MASSACHUSETTS INSTITUTE OF TECHNOLOGY

# HYDRODYNAMICS LABORATORY

DEPARTMENT OF CIVIL ENGINEERING

REPORT NO. 47

## STREAM DYNAMICS AND BOUNDARY SHEAR DISTRIBUTIONS FOR CURVED TRAPEZOIDAL CHANNELS

BY

A. T. IPPEN, P. A. DRINKER, W. R. JOBIN, AND O. H. SHEMDIN

JANUARY 1962

PREPARED UNDER

CONTRACT NO. 12-14-100-2590[41]

COOPERATIVE RESEARCH AGREEMENT NO. 12-14-100-5227[41]

AGRICULTURAL RESEARCH SERVICE

U. S. DEPARTMENT OF AGRICULTURE

R-62-11

HYDRODYNAMICS LABORATORY
Department of Civil Engineering
Massachusetts Institute of Technology

# STREAM DYNAMICS AND BOUNDARY SHEAR DISTRIBUTIONS FOR CURVED TRAPEZOIDAL CHANNELS

by

A. T. Ippen, P. A. Drinker, W. R. Jobin, and O. H. Shemdin

REPORT NO. 47

January, 1962

Prepared Under
Contract No. 12-14-100-2590[41]
Cooperative Research Agreement No. 12-14-100-5227[41]
Agricultural Research Service
U. S. Department of Agriculture

## ABSTRACT

An investigation was conducted on the distribution and magnitudes of boundary shear stresses arising from subcritical flows through curved trapezoidal channels. The test series was designed to determine the effects on the shear patterns of variation in discharge, bend geometry, boundary roughness, and upstream channel alignment. Two flumes of different bend radius and base width were used, each consisting of a single circular curve of 60° central angle, with straight upstream and downstream tangent sections. Both flumes were constructed with 2 to 1 side slopes, and the base horizontal along all transverse sections. The greatest part of the test program dealt with flows in smooth channels. For a Froude number range of 0.32 to 0.55, the stream geometries varied as follows: ratio of width to depth, $7 < w/y_o < 12$; ratio of width to centerline radius, $0.29 < w/r_c < 0.80$. Two tests were conducted in a rough-surfaced channel at stream geometries corresponding to runs in the smooth channel series. For the final four tests described, which were conducted in a smooth channel, sets of screens were installed in the approach flow in order to simulate the disturbances caused by additional curves upstream from the test reach. By this method, the shear distribution was studied for systems of two curves of similar sense, and for sets of reverse curves. Local boundary shear stresses were measured with surface Pitot tubes adapted for application in free surface flows. The calibration for these instruments, originally developed for air flows through smooth pipes, was found to be valid for direct application in the smooth channels. A modified Pitot tube was developed and calibrated for use on the rough test surface.

The boundary shear stress data are presented as relative shear, $\tau_o/\overline{\tau_o}$ (i.e. as local shear in terms of the shear for uniform flow), in the form of contour maps of the test reach; velocities and water surface elevations are presented by section.

The boundary shear patterns obtained cannot be predicted quantitatively from the gross characteristics of the flow. Local shears were found to occur at intensities of more than double the mean tractive force computed for uniform flow; as might be expected, the intensities of these local shears increase markedly with the stream curvature. A one-dimensional treatment of the energy dissipation in the curve and downstream tangent fails to indicate either the peripheral locations or the intensities of the greatest boundary stresses. In general, the distributions and the relative magnitudes of the local boundary shear stresses appear to be functions of the stream geometry, for streams in subcritical motion.

The patterns of velocity and shear in a stream curve are influenced, both directly and indirectly, by the transverse and longitudinal pressure gradients in the curve. An analysis of the water surface superelevation in curving flow reveals that, for conditions of moderate curvature, the transverse water slope is quite insensitive to variations in the velocity distribution, and that it depends only on the mean momentum of the flow and the stream geometry.

ACKNOWLEDGEMENTS

This investigation was conducted at the Hydrodynamics Laboratory, Department of Civil Engineering, of the Massachusetts Institute of Technology during the period March 1958 through September 1961. The work was sponsored by the Soil and Water Conservation Research Division, Agricultural Research Service, U. S. Department of Agriculture, under Contract Number 12-14-100-2590[41], and Cooperative Research Agreement Number 12-14-100-5227[41]. The support for this work was established through the MIT Division of Sponsored Research under DSR Project Numbers 5-7922 and 4-8682.

The experimental study was outlined in close liaison with Messrs. Louis M. Glymph, Jr., Carl R. Miller, and Donald A. Parsons of the Agricultural Research Service. Their interest in the work contributed greatly to its success, and through periodic re-evaluation of the project aims, new areas of study were opened which had not been envisioned in the original proposals. Dr. Arthur T. Ippen acted as project supervisor throughout the investigation. Dr. Ronald E. Nece, and Messrs. Charles A. Givler and Georges K. Noutsopoulos participated in the early phases of the work. Messrs. William R. Jobin and Omar H. Shemdin, Research Assistants, performed much of the experimental work and prepared the drawings for the report. Dr. Philip A. Drinker was associated with the project throughout, initially as Research Assistant, and during the final year of study as Geologist, Soil and Water Conservation Research Division, Agricultural Research Service.

TABLE OF CONTENTS

TABLE OF CONTENTS (continued)

LIST OF FIGURES

LIST OF FIGURES (continued)



LIST OF TABLES

## DEFINITIONS AND NOTATIONS

$A$ = channel cross-section area.

$b$ = bottom width of channel.

$C_{f_x}$ = mean coefficient of friction at section x = $\tau_x / \frac{\rho V_x^2}{2}$.

$d$ = diameter of Pitot and Prandtl tubes.

$\mathbb{F}$ = Froude number = $V / \sqrt{g y_m}$.

$g$ = gravitational acceleration, ft/sec$^2$.

$H_o$ = specific head, $y_o + V^2/2g$, ft-lb/lb.

$\Delta H$ = manometer reading, ft. of water.

$k$ = absolute height of roughness particle.

$k_e$ = equivalent sand roughness height.

$L$ = centerline arc length of the test reach.

$p_t$ = total, or stagnation, pressure, lb/ft$^2$.

$p_o$ = static pressure, lb/ft$^2$.

$P$ = wetted perimeter.

$Q$ = volumetric rate of flow, ft$^3$/sec.

$r$ = radial distance to a point in curve.

$r_c$ = radius of curvature of channel centerline.

$r_o$ = radius of curvature of outer edge of water surface.

$R$ = hydraulic radius, A/P, ft.

$\mathbb{R}$ = Reynolds number, $4RV/\nu$.

$\mathbb{R}_x$ = boundary layer Reynolds number $Vx/\nu$.

$\mathbb{R}_*$ = shear Reynolds number, $u_* y/\nu$.

$S_o$ = channel slope, ft/ft.

$S_e$ = energy gradient ft/ft.

$\bar{S}_{e_L}$ = average energy gradient over the test reach.

$S_{e_x}$ = local rate of energy dissipation at section x, ft-lb/lb/ft.

T = water temperature, $^oF$.

u,v = local velocity, ft/sec.

$u_*$ = shear velocity, $\sqrt{\tau_o/\rho}$, ft/sec.

V = free stream velocity or average velocity, Q/A, ft/sec.

w = water surface width.

x = longitudinal distance measured along channel centerline.

y = distance normal to plane of channel bottom.

$y_m$ = average depth = A/w.

$y_o$ = total depth of flow.

z = transverse distance.

$\alpha$ = angular misalignment of test probe.

$\gamma$ = specific weight of liquid, $lb/ft^3$.

$\delta$ = boundary layer thickness, ft.

$\varepsilon$ = kinetic energy correction factor.

$\theta$ = local central angle of curvature from beginning of bend, degrees.

$\mu$ = dynamic viscosity of fluid, $lb\text{-}sec/ft^2$.

$\nu$ = kinematic viscosity of fluid, $ft^2/sec$.

$\rho$ = mass density of fluid, $slugs/ft^3$.

$\tau_o$ = local boundary shear stress, $lb/ft^2$.

$\bar{\tau}_o$ = average boundary shear stress at curve entrance(Sta.1)$lb/ft^2$.

$\tau_x$ = average boundary shear stress at section x.

$\bar{\tau}_L$ = average boundary shear stress over the full test reach.

f(),$\Phi$() = function of.

# I. INTRODUCTION

The destruction of valuable land by erosion in stream bends is a problem which has stimulated a considerable amount of research directed towards the control of meandering and scour in alluvial streams. As an immediate attack on the problem, primary interest has been focused on techniques of channel stabilization through the placement of erosion-resistant revetments or other boundary modifications designed to inhibit local scour. For lack of systematic quantitative information on the modes of erosion in curves, the installation of revetments has an empirical basis, founded upon field studies of localized stream systems. Laboratory studies of sediment motion, as well as of velocity patterns in curving flumes, have contributed greatly to the general understanding of stream hydraulics and morphology. However, owing to the complexity of the motion of fluids in curved channels, it has not been possible either to establish a satisfactory theoretical basis for curving flow, or, failing this, to predict the scour intensities from measured velocity distributions.

The study described in this report was conducted to determine the distributions and magnitudes of the boundary shear stresses generated in curved reaches of rigid prismatic channels. In this work, which represents an initial attack on the erosion problem, all sediment properties were excluded from consideration, and only the effects of the flow pattern on a clearly defined set of boundary surfaces were studied. A general explanation of the various related aspects of sediment mechanics -- erosion, transport, and deposition -- will require much supplementary investigation of systems containing sediment in order to establish first, the role of sediment in modifying the dynamic properties of the transporting fluid itself, and second, the effect on the scour pattern of boundary modifications caused by the movement of bed material.

An earlier report (19) describes the development of the test equipment and instrumentation, and presents the results of the tests conducted during the period covered by the original research program. In order to broaden the scope of the investigation, a further series of tests was performed in which the range of stream parameters was extended. This report comprises the final report on these studies of boundary shears in trapezoidal channels. In order to better coordinate the analyses and discussions, the results of all tests, including those recorded previously, are presented. The experimental equipment and instrumentation have been described at length (19) and, except for the modifications in the test channel, equipment details are not included here.

In view of the findings from the later experiments, the original data were re-examined, resulting, in several cases, in modifications of ideas formed earlier. In substance however, the conclusions drawn from the earlier tests were not greatly affected by the results of the final experiments; rather, it will be seen that the increased scope of the investigation lends greater generality to these conclusions.

## II. FLOW THROUGH CURVED CHANNELS: A REVIEW

As a basic model of flow through channel curves, consider first the flow through a deep, smooth-surfaced, prismatic bend. If frictional effects are assumed negligible, potential theory permits description of the curved flow as a free vortex. Mockmore (31), among others, has demonstrated that at some distance from the boundaries both the velocity distribution and the transverse water surface profile are well described by an irrotational vortex. For this case the transverse velocity distribution is given by the constant product of local tangential velocity, u, and radius, r. By equating the radial forces on a fluid particle as,

$$\frac{dp}{dr} = \rho \frac{u^2}{r}, \tag{1}$$

the water surface profile can be computed from

$$\Delta y = \frac{1}{g}\int \frac{u^2}{r}\, dr, \tag{2}$$

where the flow in the curve is assumed to be concentric. For the free vortex the water surface profile is hyperbolic, convex upward.

However, examination of the flow near the boundaries shows that even in a smooth-walled flume, frictional effects combined with the superelevation tend to cause two important deviations from potential flow: helicoidal motion of the main stream and separation in zones of adverse pressure gradient.

In 1876 Thompson (44) gave his now familiar explanation of helicoidal, or spiral flow as being due to the difference in centripetal acceleration between the fluid near the bottom, which has been retarded by boundary drag, and the faster moving layers near the free surface. This acceleration, which results from the radial increase in depth (and hence in pressure), causes the low velocity fluid near the bed to move towards the center of the curve, while the fluid near the surface, having excess momentum, moves towards the outside.

The superelevation of the water surface in a channel curve leads to two occurrences of longitudinal increase in depth: along the outer bank of the curve as the water rises entering the curve, and at the curve exit along the inner bank where the flow recovers to normal depth (see for example, Figures 5 and 8). For channels of large curvature, separation may develop in these two areas and the water surface may slope upstream locally. The fluid particles near the boundary have insufficient kinetic energy to move against a pressure gradient, and separation of the boundary layer from the streambank results. A simple circular curve connecting two tangent channels is likely to produce larger separation

zones than would a natural stream bend, with more gradual transitions. In periods of high flows separation in natural channel bends manifests itself as eddies or "bank rollers" and results in bar deposits.

It has been pointed out (26)(46) that superelevation as such in subcritical curving flow is quite insensitive to radial variation in the velocity distribution. Substitution into Equation (2) of other assumed velocity distributions, and integration over the full width of the stream, give only minor variations in the total elevation difference, even though the surface profiles vary in shape. Superelevation is a result of curved flow for all fluids, and is essentially independent of the frictional aspects and the velocity distribution of the flow. It is controlled primarily by the boundary geometry and the mean momentum of the stream. Thus, while superelevation provides the mechanism by which separation and helicoidal motion take place, their direct cause is boundary friction or shear stress, and in a completely frictionless flow they could not occur.

In deep, turbulent streams, the separation zone at the concave bank is usually obliterated by the turbulent infusion of momentum from the main body of the stream, although bank rollers are observed at the outside of abrupt, shallow bends. The separation zone at the inner bank is more persistent, as shown by the point bar deposits common to virtually all streams except those which are deeply incised and actively degrading. The persistence and extent of this latter zone are due both to the abrupt rise in water surface at this point, and to the spiral motion of the stream which tends to move the faster moving fluid to the opposite bank.

Examples of helicoidal motion and separation in a laboratory flume bend are shown in Figures 1 and 2. Both of these photographs were taken from the bend exit, facing upstream, so that the flow is from top to bottom of the photographs. Figure 1 was taken after dye had been injected and allowed to spread to the full extent of the separation zones. In Figure 2 the fainter dark streaks were caused by dye crystals moving towards the inner bank with the bottom current (the dashed arrow), while the heavier plume was made by continuous injection of dye at the surface (the solid arrow).

These two phenomena have far reaching effects on the flow in natural streams. The helicoidal pattern is, perhaps, the more important, in that, by shifting the faster moving fluid to the outside of the bend, it tends to suppress the free vortex pattern. Einstein and Harder (8) show experimentally that, for a curve of sufficient length, a stable velocity distribution develops in which the velocity increases radially outwards. That is, of course, the phenomenon observed in long river curves in which the thalweg remains near to the concave bank.

The pattern of helicoidal flows in the bend of a rectangular flume was studied by Shukry (39) using a Pitot sphere to determine the three components of the local velocity vector. It was found that the helicoidal (i.e. radial) velocities increase with increasing relative

curvature, $w/r_c$, and ratio of width to depth, $w/y_o$. Einstein and Harder (8) also observed that increasing the ratio, $w/y_o$, as well as increasing the boundary roughness, led to high velocities towards the outer bank, due, presumably, to a more pronounced helicoidal motion.

The laboratory bends in which the irrotational type of flow is observed are too short to complete the transfer of the filament of highest velocity to the outer bank. The patterns of flow in sharp bends -- of both flumes and rivers -- represent a transitional type which, with sufficient length of curved reach, would develop into the friction controlled flow described above. The length of the transition reach, however, has not been well defined in terms of the pertinent parameters.

Recently Leopold and co-workers (26) have reported an investigation on the frictional resistance of rigid sinuous channels. By studying the overall head loss over a reach, for channels of constant shape but varied sinuosities, the authors show that not only is the total energy dissipation greater in curved channels than in straight, but that it increases discontinuously above a certain threshold Froude number, due to the formation of local standing waves, or "spills", along the banks. While the rate of increase in total boundary shear is not clearly defined, a relationship is suggested between the ratio of width to radius and the Froude number at which the discontinuity occurs. In the laboratory tests the threshold Froude number varied from about 0.4 to 0.6, while, from a survey of river data, the authors found that bankfull flows generally occur in streams in the range $0.2 < F < 0.45$. They suggest that the rare occurrence of higher Froude numbers may be due to a tendency of alluvial rivers to eliminate local areas of high resistance. Such a local reduction in boundary shear could come about through erosion of the banks at points of greatest spill occurrence, where there is increased dissipation of energy.

The relationship between shear stresses and erosion is further complicated in natural streams by loose bed material which permits an additional degree of freedom not possessed by rigid boundary flumes. This freedom to shape its own bed undoubtedly causes a river to alter its flow pattern in ways which cannot readily be predicted from a study of rigid, prismatic channels (23). Thus, scour will occur in regions of high shear stress; the modifications in the bed configuration caused by the scour will in turn modify the current pattern and hence the shear distribution.

Previous investigations of energy dissipation in curved flow have been restricted to one-dimensional analyses for both open and enclosed conduits. As shown by Anderson (2), the different experimental techniques, as well as the varied definitions of a loss coefficient, used by past investigators have led to considerable confusion. Ito (21) has demonstrated, by a re-analysis of early data, that the loss coefficient of a smooth bend can be predicted empirically, if the measurements and definitions are given a common basis. With respect to the present study, a one-dimensional

approach is not very revealing in that it gives no indication as to the distribution of the boundary shear stresses that cause the loss in bends. Indeed, as is shown in the discussion to follow, the mean section loss gives little indication of the magnitudes of the local shears, and the location and intensity of erosive attack cannot be predicted by this means.

Figure 1. (above) Zones of Separation in Laboratory Channel Bend.

Figure 2. (left) Helicoidal Flow in Channel Bend.

# III. EXPERIMENTAL EQUIPMENT AND TECHNIQUES

## A. The Test Channel

### 1. Description of the Equipment

The experiments were conducted in the two trapezoidal flumes shown in Figure 3. In both channels the general arrangement is the same, consisting of a straight approach section 20 feet in length, a single curve of 60-degree central angle, and a straight 10-foot exit section. The side slopes are constant at 2 horizontal to 1 vertical and the channels were constructed with the invert horizontal along all radial sections. A smooth entrance transition from the stilling basin at the upstream end of the approach channel reduces the tendencies for local separation. Additional control of depth is provided by an adjustable sluice gate mounted at the exit section. Details of the basic design of the channel facility are given in Reference 19.

The larger flume (Figure 3a) has a 24-inch base width, and the radius of the curve centerline is 60 inches. For the smaller flume, which was laid in the bed of the larger, the base width dimension was halved and the stream section was shifted outward to follow the concave bank of the original curve, giving a curve centerline radius of 70 inches.

In a curved trapezoidal stream, the relative curvature -- i.e. the ratio of surface width to bend radius -- varies with depth and thus cannot be given solely in terms of the boundary geometry. However, the limiting values of relative curvature are those set by the base width. Thus, the range of curvatures which may be obtained in the two flumes is limited by $w/r_c > b/r_c = 0.40$ and $w/r_c > b/r_c = 0.17$ in the larger and smaller channels, respectively. In each channel, therefore, tests at several depths give a moderate range in relative curvature, the lower limit of which is fixed by the boundary curvatures, $b/r_c$.

During the installation of the original flume structure, the centerline slope was set at 0.00064 = 1/1563. The slope was not adjusted throughout the test program; however, after construction of the smaller channel, it was found that the approach slope had decreased to 0.00055 due to settling of the foundations.

The channels were treated with a waterproof plastic coating which dries to form a tough elastic film. For the series of smooth boundary tests it was found that this material provides a hydraulically smooth surface, giving a mean Manning coefficient of 0.010.

For the rough boundary tests which were conducted in the larger channel, the surface was prepared as follows: the channel was given two coats of varnish; while the surface was still wet, roughness particles were spread by hand over the bottom and sidewalls of the section. After

the material had dried, the surface was scraped with a flat bar to knock off any protruding particles, and then sealed with a final coat of varnish. The rough surface was applied over 15 feet of the approach section, through the curve and for 8 feet in the exit reach. The roughness particles are uniform, rectangular, lucite parallelepipeds, of the approximate dimensions, 0.18 x 0.10 x 0.10 inches. The absolute roughness height of the completed surface was taken as 0.1 inches; for the treated channel the Manning coefficient is 0.017.

Modification of the test facility to incorporate additional combinations of curves would have entailed great additional expense. Therefore, the effects of varied channel alignment were studied through simulation of the flow disturbances caused by curvature in the approach channel. For this purpose, sets of screen baffles were installed in the upstream tangent. The different screen combinations were established by trial and error to produce the desired flow patterns at the entrance to the curve.

### 2. Operating Conditions

For each desired depth condition, the discharge at uniform flow was calculated from the Manning equation. During the early tests in the smooth channels the Manning coefficient was assumed as $n = 0.009$. As the test program continued the channel resistance could be checked, and it was found that the proper value for the plastic finish was $n = 0.010$. A similar trial procedure in the rough channel gave the Manning coefficient, $n = 0.017$.

With the proper discharge flowing in the channel, the sluice gate was employed to adjust the depth at the entrance to the curve. This downstream control was necessary because of the backwater effects of the channel outfall which, before its installation, had been observed to extend through the curve and well into the approach tangent.

Flow uniformity had little significance in the tests on the simulated curve systems due to the large scale modification of the flow pattern produced by the screens. For these tests, therefore, the discharges and sluice gate settings were those established for the corresponding tests at uniform approach conditions.

## B. Instrumentation

### 1. The Measurement of Boundary Shear Stress

a. General Requirements: The basic objective of this study involved the mapping of boundary shear intensities in the curved test reach at varied conditions of flow. Thus, the primary requirements of the shear instrument to be used were that it be readily movable and that it have a rapid response.

Because of the secondary currents in the bend region, it was

further necessary that the instrument be insensitive to moderate variations in the direction of flow. Local velocities close to the boundary in a bend possess lateral as well as longitudinal components, and consequently the boundary shear stresses are also skewed with respect to the channel centerline. For moderate skewness however (e.g. less than 20 degrees), the magnitudes of the local velocities and boundary shear stresses may be taken as equal to their downstream components. Thus, local shear magnitudes may be adequately determined with an instrument aligned parallel to the downstream direction, provided the instrument itself is not subject to appreciable error arising from lateral components of flow.

A discussion of methods of determining local shears is given in Ref. 19; each of the techniques listed was reviewed in terms of the requirements of this study.

b. Shear Measurement by Surface Pitot Tubes: Of the various means available for the measurement of boundary shear stress the surface Pitot tube technique developed by Preston (37) was found to be best suited to the purposes of this study. By this method, the shear stress on a smooth boundary is computed from the dynamic pressure registered by a round Pitot tube resting on the surface. Preston demonstrated that, for a tube of sufficiently large diameter, the effects of the viscous sublayer become negligible, and the mean total pressure over the face of the tube is dependent only on the velocity distribution in the turbulent boundary layer.

The velocity distribution in the turbulent boundary layer over a smooth surface can be expressed,

$$\frac{u}{u_*} = f\left(\frac{u_* y}{\nu}\right) \; ; \quad u_* = \sqrt{\frac{\tau_o}{\rho}} \; . \tag{3}$$

Preston developed the functional groupings by which the shear stress at the wall, $\tau_o$, could be expressed as a dependent variable, and by direct calibration in pipe flows obtained the equation,

$$\log \frac{\tau_o d^2}{4\rho\nu^2} = -1.396 + 0.875 \log \frac{(p_t - p_o)d^2}{4\rho\nu^2} \tag{4}$$

valid within the range,

$$4.5 < \log \frac{(p_t - p_o)d^2}{4\rho\nu^2} < 6.5.$$

Here $\rho$ and $\nu$ are the density and kinematic viscosity of the fluid, and $(p_t - p_o)$ is the dynamic pressure recorded by a round Pitot tube of outer diameter = d. This calibration equation depends on the velocity distribution near the wall which was found to be expressible as the power law,

$$\frac{u}{u_*} = 8.61\left(\frac{u_* y}{\nu}\right)^{1/7} \quad . \tag{5}$$

Although Preston developed Equation (4) for a set of Pitot tubes of constant ratio of inner to outer diameters, Hsu (18) later showed, both analytically and by experiment, that, for a tube of given outer diameter, the internal diameter has negligible effect on the Pitot tube calibration.

Equation (4) was verified by both Preston and Hsu on flat surfaces under varied pressure gradients. For the present open channel work, the calibration was first checked directly in a tilting glass flume. In the curve of the trapezoidal test channel, however, direct calibration was not possible because of the non-uniformity of the flow. In order to establish the validity of Equation (4) for this application, velocity profiles in the flow immediately adjacent to the boundary ($y < 1$ cm) were taken at various points in the curve. By this method the existence of the velocity distribution given by Equation (5) was established (see Reference 19, Appendix A); therefore, the validity of Equation (4) could be assumed, subject to the restriction that the surface Pitot tube lie wholly within the established boundary layer region of similarity.

For the rough boundary tests, a surface Pitot calibration was developed, which had been suggested in principle by Preston. In turbulent flow over a hydraulically rough surface, the velocity distribution being independent of Reynolds number may be expressed,

$$\frac{u}{u_*} = f_a\left(\frac{y}{k}\right) \quad , \tag{6}$$

where k is the absolute height of the boundary protrusions. Thus, by dimensional considerations alone, the expression analogous to Equation (4) becomes,

$$\frac{\tau_o}{(p_t - p_o)} = f_b\left(\frac{d}{k}\right) \quad . \tag{7}$$

On the non-uniform surfaces encountered in general practices, direct application of Equation (7) would be questionable, dur to the uncertainty of consistent Pitot tube placement. Furthermore, from analysis of Nikaradse's rough surface velocity data (33), it seems clear that f, in Equation (7), should vary with the value of $y_o/k$.

If, however, tests are conducted over a limited range of $y_o/k$ on a surface of sufficiently uniform roughness, then it should be possible to find a single form of Equation (7). Direct calibration of a round Pitot tube was performed in a tilting flume on an artificially

roughened surface, identical to that which was later used in the test channel. The test conditions were: $d = 0.432"$, $k = 0.1"$, $2" < y_o < 6"$, for mean velocities ranging up to 5 fps. The empirical equation obtained,

$$\tau_o = 0.021(p_t - p_o) , \qquad (8)$$

is valid only for the above set of conditions. Since the calibration was performed with only one Pitot tube, the general dimensionless expression, Equation (7), was not established, and the restricted form, Equation (8), is to be preferred.

c. Experimental Application: (i) Smooth Surface: Various models of surface Pitot tubes (19), were employed during the tests. The final version, designated as the Model III instrument, is shown in Figure 4. The static tube is positioned above the total head tube in order to minimize the effects of the total pressure gradient near the boundary on the measured static pressure. Before final assembly of the instrument it was determined that the two tubes exert no mutual interference, and that the pressure in the channel curve is hydrostatically distributed over the depth of flow. The two leads from the instrument are connected to a manometer to give the desired dynamic head, $(p_t - p_o)/\gamma$.

To measure the boundary shear stress at a point, the instrument is mounted vertically with the total head tube aligned parallel to the downstream direction and the tip resting on the boundary. The shear value is computed from Equation (4) using the dynamic head as read from a manometer. Because each test involved about 200 readings, it was expedient to re-arrange and plot Equation (4) to give a direct graphical solution of $\tau_o$.

In preliminary tests it was found that the instrument is quite insensitive to moderate misalignment of the probe axis with the local direction of velocity. For deflection angles up to $20^o$, the error in measured shear stress varies essentially as $(1 - \cos\alpha)$; at $\alpha = 20^o$ the error is 6%, and at $\alpha = 15^o$ the error is about 3%. Dye traces in the channel curve revealed a maximum angularity of the flow of about $20^o$, which is confined however to a very thin zone adjacent to the boundary.

(ii) Rough Surface: For the measurement of shear stress on the rough test surface, the Model III tube was fitted with the adapter sleeve and bushing shown in Figure 4 which raised the diameter of the impact tube to 0.432 inches. This was done in order to increase the value of the manometer readings obtained, as well as to reduce the effects of local disturbances due to the individual roughness particles. The procedure for measuring shear stress with the modified instrument is essentially the same as the smooth surface technique, the value of $\tau_o$ being computed in this case from Equation (8).

2. Additional Instrumentation

a. Manometry: Two types of manometers were used in this study. These instruments have been described in the earlier report (19). One of these, a micromanometer, consists of two piezometer columns with affixed micrometer point gauges. The other, an inclined manometer, being the faster and more convenient, was used in most of the work.

b. Depth Measurements: Depths of water in the channel were measured with a point gauge mounted on the instrument carriage. In certain of the tests it was more convenient to determine depths from static pressure measurements which were correlated with the centerline depths as determined from the point gauge readings.

c. Velocity Measurements: Stream velocities were measured with a 5/16-inch Prandtl tube. The instrument was always aligned parallel to the downstream component of flow, and no attempt was made to determine the lateral velocity components.

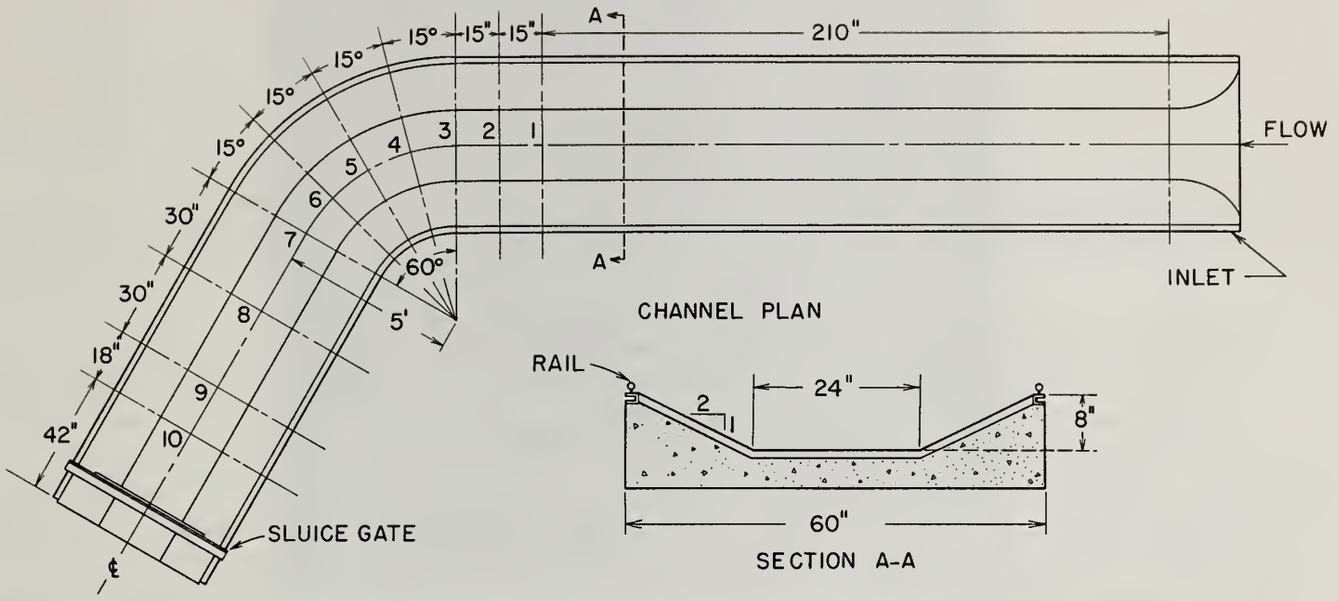


(a)

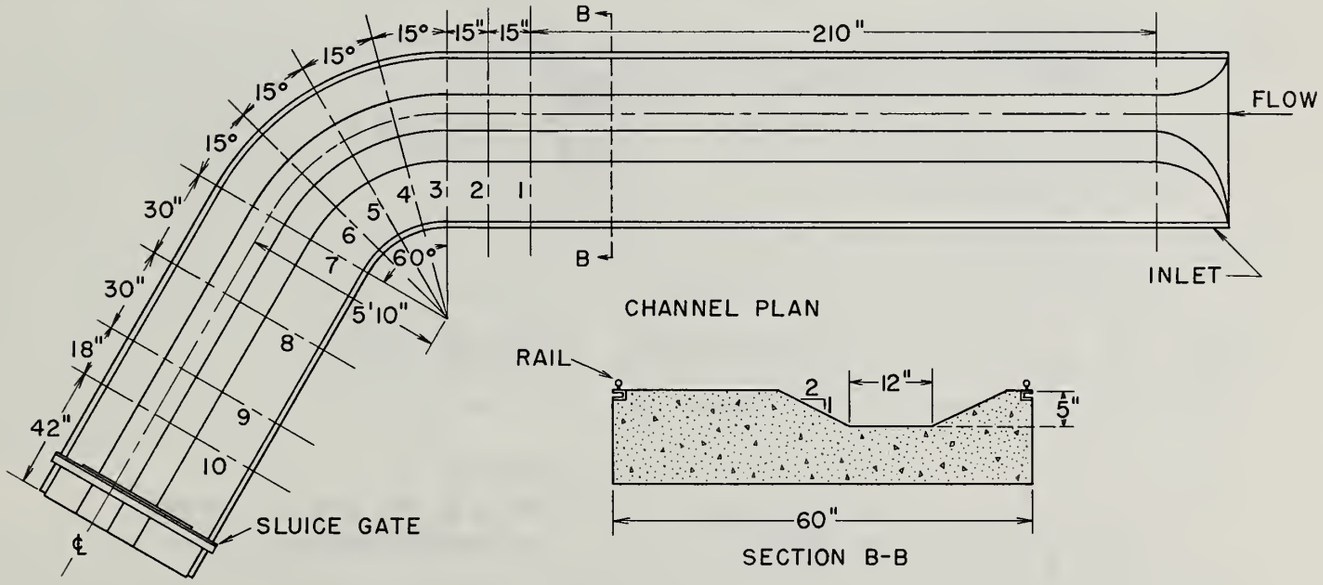


(b)

Figure 3. The Trapezoidal Channels. The locations of the ten test stations are indicated by the dashed section lines.

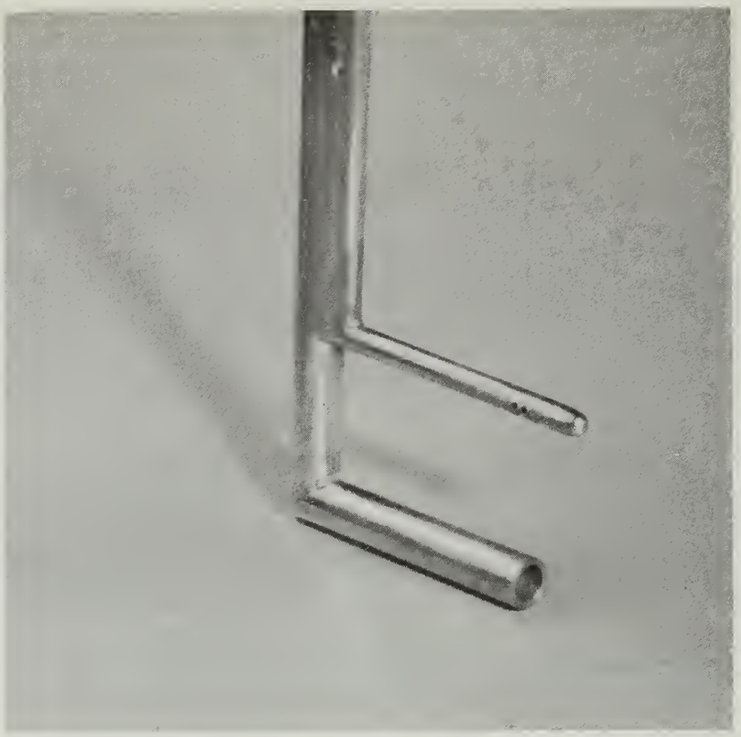

(a.) Instrument Mounted on Flat Surface.

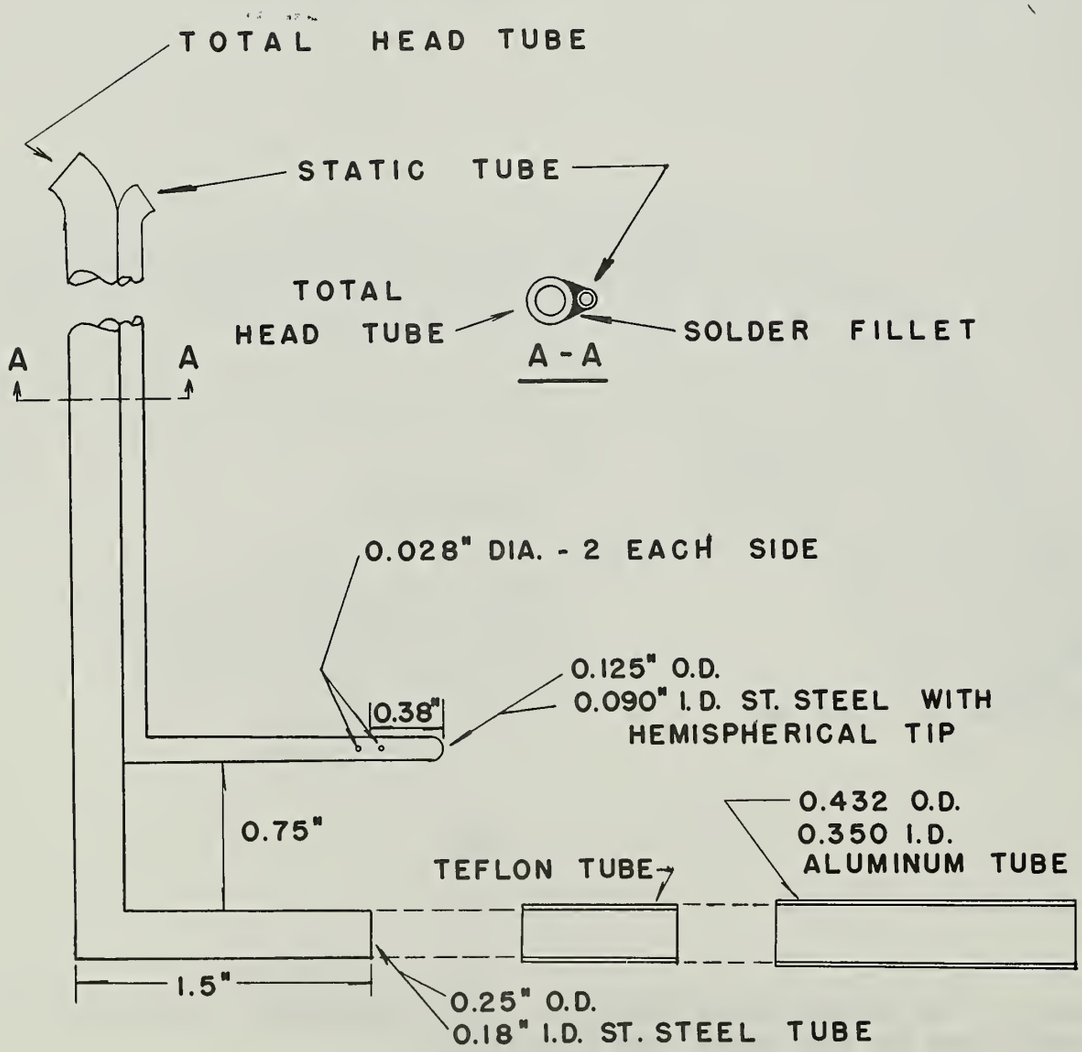


(b) Construction details showing the cylindrical sleeve adapter for the Model III-A Rough Surface Tube.

Figure 4. Model III Surface Pitot tube.

## IV. THE EXPERIMENTAL PROGRAM

### A. Scope of the Study

The tests were conducted in the two channels shown in Figures 3a and 3b, covering the range of flow geometries which is summarized in Tables I and II.

With the exception of Runs 10-13, the flow entering the curve was essentially uniform and symmetrical about the centerline. For purposes of discussion, therefore, it is convenient to consider Runs 1-9 as comprising one test series covering a broad range of boundary geometries for the simple configuration of a curve with straight tangents. Runs 1-7 comprise the complete series of smooth surface, single curve tests; for Runs 8 and 9, the channel roughness was increased and flows were studied for stream geometries similar to those in Runs 2 and 4.

In Runs 10-13, the velocity distribution in the approach flow was modified through installation of various combinations of baffle screens. By superposing asymmetrical conditions on the entrance flow it was possible to simulate the effects of varied upstream channel alignments. Tests at two depths were conducted to determine the shear pattern in a sequent bend of a double series (U-configuration), and a reverse series (S-configuration) of curves.

During the course of the test series various modifications were made in the design of the surface Pitot tube. The classification of instrument models, as listed in Table II, is given with a description of the instruments in Reference (19). In order to establish that the measured distributions of relative shear were not influenced by the specific model designs, the shear measurements were completely re-taken with different instruments. Comparison of the shear distributions for Run 2-A (Model I) with 2-D(Model II), and Run 3-A (Model III) with 3-B (Model II), showed that, while the absolute magnitudes of the local shears varied with the model used, there were no essential differences in the maps of relative shear given in terms of the mean shear stress measured at Station 1, $\tau_o$.

In performing the runs on the simulated curve systems with the Model III tube, it was simply necessary, on the basis of the above tests, to re-measure the shear distribution at Station 1 and then to apply the relative shear data as computed previously. Thus the second value of $\tau_o$ given in Table II for Run 2-A and for Run 4-A, represents the measurement with the Model III instrument, which was used in the corresponding compound curve tests.

It will also be noticed that while two tests were conducted at a 6-inch depth, the energy gradient, mean velocity, and hence the shear stress of the approach flow were varied markedly between the two runs.

Unlike Runs 2 and 3, which were repeated at similar conditions in order to verify the experimental techniques, Runs 4-A and 4-B represent essentially different tests. The purpose of these tests, which are discussed in a later section, was to study the effect of approach flow non-uniformity on the shear pattern in the curve.

For all of the tests, boundary shear stresses were measured at the ten test stations indicated in Figures 3a and 3b. Highly non-uniform shear patterns in several of the runs made it necessary to add two intermediate sections between Stations 7 and 8. Shear measurements were taken at 2" intervals across each station, covering the full wetted perimeter except the outer 4" along each side.

Complete measurements of water surface elevations and local velocities were made at each station in Runs 1-4. As the test program progressed coverage of these variables was decreased in order to limit the amount of data to be processed. At all depths, however, sufficient data were taken to indicate the gross characteristics of water surface superelevation and velocity distribution.

It should be mentioned that the numbering system of the test runs shown in Table I was established to give a logical sequence to the order of discussion, and that it does not follow the chronological order of the experiments. All of the tests involving the larger smooth channel (Figure 3a) were completed before application of the rough surface. Following the completion of the two tests on the rough surface, the channel was modified to give the flume arrangement shown in Figure 3b, and the final three tests were those conducted in the smaller smooth-surfaced channel.

## B. Presentation of Data

The volume of the basic data compiled during the course of this study is such that direct presentation of the tabulated material would make analysis difficult. Therefore, in order to facilitate the discussions of the results, the data presented herein have been reduced to graphical form. The complete compilation of tabulated data has been printed and is available in the basic data supplements of this report.

The data figures for the various tests are presented in the appropriate discussion sections in the following text. Before proceeding with the discussions, however, it is convenient to define the method of presentation of each group of data.

### 1. Velocity and Water Surface Profile Data

The velocity distributions and transverse surface profiles are presented by stream sections following the sequence of test stations in the curved reach. Because of the repetitive nature of these patterns

drawings were prepared only for representative tests.

2. Boundary Shear Stress Data

The value of the mean measured shear stress at Station 1, $\overline{\tau_o}$, was determined for each test by graphical integration of a plot of the local shear stress, $\tau_o$, over the wetted perimeter;

$$\overline{\tau_o} = \frac{1}{P} \int_P \tau_o \, dP \Big]_{\text{Sta. 1}} . \qquad (9)$$

The maps of boundary shear distribution for the full test series are presented in terms of relative local shear, $\tau_o / \overline{\tau_o}$. This form is preferable to reporting absolute values, since application of the results is simpler, and the shear patterns for varying flow conditions are readily compared. The absolute magnitudes of local shears may be computed from the shear maps using the values of $\overline{\tau_o}$ (Table I) obtained from Equation (9).

TABLE I

Summary of Channel Geometries Covered in the Test Program.

| Run No. | Nominal Stream Dimensions $\frac{w}{y_o}$ | Nominal Stream Dimensions $\frac{w}{r_c}$ | Channel Dimensions | Boundary Roughness | Velocity Distribution in Approach Flow |
|---|---|---|---|---|---|
| 1 | 12 | 0.60 | $b/r_c = 0.40$ Fig. 3a | Smooth $n = 0.010$ | Symmetric; Single curve with straight tangents. |
| 2 | 10 | 0.67 | | | |
| 3 | 8.8 | 0.73 | | | |
| 4 | 8 | 0.80 | | | |
| 5 | 10 | 0.29 | $b/r_c = 0.17$ Fig. 3b | | |
| 6 | 8 | 0.34 | | | |
| 7 | 7 | 0.40 | | | |
| 8 | 10 | 0.67 | | Rough $n = 0.017$ | |
| 9 | 8 | 0.80 | | | |
| 10 | 10 | 0.67 | $b/r_c = 0.40$ Fig. 3a | Smooth $n = 0.010$ | Asymmetric; Flow pattern modified to simulate upstream curvature. |
| 11 | 8 | 0.80 | | | |
| 12 | 10 | 0.67 | | | |
| 13 | 8 | 0.80 | | | |

TABLE II

Summary of Test Conditions Determined in the Approach Flow (Station 1).

| Run No. | | 1 | 2-A;10;12 | 2-B | 3-A; B | 4-A;11;13 | 4-B | 5 | 6 | 7 | 8** | 9** |
|---|---|---|---|---|---|---|---|---|---|---|---|---|
| $y_o$ | in | 2.98 | 3.86 | 4.00 | 5.08 | 6.00 | 5.99 | 2.01 | 3.02 | 3.98 | 3.94 | 6.04 |
| A | sf | 0.620 | 0.850 | 0.889 | 1.210 | 1.500 | 1.498 | 0.223 | 0.378 | 0.550 | 0.889 | 1.463 |
| R | ft | 0.199 | 0.246 | 0.255 | 0.311 | 0.354 | 0.354 | 0.127 | 0.177 | 0.222 | 0.249 | 0.337 |
| w | in | 35.92 | 39.44 | 40.00 | 44.32 | 48.00 | 47.96 | 20.04 | 24.08 | 27.92 | 40.70 | 49.10 |
| $y_m$ | ft | 0.208 | 0.259 | 0.267 | 0.326 | 0.375 | 0.375 | 0.134 | 0.188 | 0.236 | 0.262 | 0.357 |
| $r_o/w$ | | 2.17 | 2.02 | 2.00 | 1.86 | 1.75 | 1.75 | 4.00 | 3.41 | 3.01 | 1.97 | 1.73 |
| $w/y_o$ | | 12.05 | 10.21 | 10.00 | 8.72 | 8.00 | 7.99 | 9.98 | 7.98 | 7.02 | 10.32 | 8.13 |
| Q | cfs | 0.85 | 1.27 | 1.26 | 2.02 | 2.86 | 2.00 | 0.19 | 0.45 | 0.77 | 0.84 | 1.77 |
| V | fps | 1.36 | 1.50 | 1.43 | 1.67 | 1.91 | 1.33 | 0.87 | 1.19 | 1.40 | 0.94 | 1.18 |
| F | | 0.53 | 0.52 | 0.49 | 0.52 | 0.55 | 0.38 | 0.42 | 0.48 | 0.51 | 0.32 | 0.34 |
| R x $10^{-5}$ | | 1.21 | 1.63 | 1.62 | 2.31 | 3.00 | 2.10 | 0.44 | 0.84 | 1.24 | 0.94 | 1.42 |
| $S_e$ x $10^5$ * | | 71 | 60 | 64 | 65 | 68 | 32 | 52 | 64 | 66 | 68 | 67 |
| $\gamma R S_e$ x $10^4$ | psf | 88 | 92 | 102 | 127 | 150 | 70 | 40 | 70 | 88 | 105 | 140 |
| $\bar{\tau}_o$ x $10^4$ | psf | 70 | 87 81 | 88 | 101 121 | 148 123 | 60 | 34 | 55 | 74 | 85 | 120 |
| Surface Pitot Tube Model | | II | I III | II | III II | II III | II | III | III | III | III-A | III-A |

*The bottom slope, $S_o$, is assumed as 0.00064 in all but Runs 5-7; in Runs 5, 6, 7, $S_o$ = 0.00055.

**The slight difference in geometries between these and the corresponding smooth surface runs is due to the installation of the rough surface material.

# V. DISCUSSION OF RESULTS

## A. Tests Conducted with Uniform Conditions of Approach: Flow Through Single Curves

### 1. Smooth Channel, Runs 1-7

a. Entrance Conditions: For the series of tests conducted in the smooth channels with undisturbed approach conditions, the velocity, water surface and shear stress configurations at the entrance to the test section are essentially symmetrical about the centerline axis (Figures 5-10). At conditions of greater relative curvature and depth a slight asymmetry becomes evident at Station 1 due to the backwater effects of the curve. It seems clear however that the flow pattern in the bend cannot be ascribed to upstream distortion of the flow.

The existence of a fully developed turbulent boundary layer was desired at the entrance to the curve. The boundary layer thickness, $\delta$, may be approximated by the Blasius expression, assuming turbulent conditions from the channel entrance, $x = 0$;

$$\frac{\delta}{x} = \frac{0.38}{\left(\frac{V_x}{\nu}\right)^{1/5}} \quad . \tag{10}$$

Substitution of the values, $V = 1.50$ fps and $\nu = 10^{-5}$ ft$^2$/sec., gives $\delta = 4.6$ inches at $x = 20$ feet. Because of the relatively small variation in Reynolds numbers, the boundary layer thickness varied only a small amount over the full set of flow conditions. Thus the boundary layer was fully developed in Runs 1-2 and 5-7, and essentially so for the 5-inch and 6-inch depths, Runs 3 and 4.

Because the low channel slope made it impossible to obtain the energy gradient accurately, it is not known to what extent fully uniform flow was achieved. However, it is believed that this condition is not of great consequence for the results of this study. It will be noted that Runs 4-A and -B represent the largest variation in $F$ and $S_e$, yet the contours of $\tau_o / \overline{\tau_o}$ for these tests were found to be virtually identical. Thus, while the magnitude of the mean shear stress varies essentially as the mean velocity head, the distribution of relative shears is but little affected by variations in the Froude number and energy gradient of the approach flow.

b. Flow through the Curve: The flow through the channel bend exhibits the expected tendency toward free vortex motion, and in the upstream portion of the curve (Stations 3-5) the velocity patterns and water surface configurations are in general agreement with those found by previous investigators (31)(39). For the full range of conditions

tested the maximum total water surface superelevations (See Section V-C below) as well as the surface profile shapes (Figures 8 and 9) conform quite closely to the trend predictable for free vortices.

The irrotational aspects of the flow are most pronounced at conditions of greatest depth and curvature. In Runs 1-4, the irrotational type of motion persists over the full length of the curve, and high velocities appear along the outer bank only at the start of the downstream tangent. (Figures 5 and 6). However, at decreased curvature (Figure 7), the transfer of higher velocities toward the outer bank is quite evident throughout the second half of the curve, and below Station 5, the irrotational pattern is suppressed.

Attention is called here once more to the phenomena previously discussed which are not readily apparent from the plots of velocities and surface elevation: separation and helicoidal motion.

Figures 1, 5, and 6 indicate the two zones of separation that may occur at the points of locally rising water surface. The zones are manifested by stable areas of reversed flow along the sloping banks. Dye injected into the bank rollers spreads rapidly throughout the separated regions, but is slow to diffuse into the main stream. The presence of these zones depends primarily on the relative curvature of the stream. At conditions of lower curvature and depth, variations in surface elevation are more gradual and are greatly reduced. In Runs 5-7 there could be detected only a vestigial zone on the inner bank, and there was no sign whatever of separation along the outer boundary.

As is shown in Figure 2, a helicoidal pattern, due to the transverse surface gradient, is well developed in the smooth channel. Since lateral components of velocities were not measured, it is not possible to evaluate the effects of bend curvature on the intensity of the spiral currents. However, the spiral velocities are generated by the transverse pressure gradient in the curve and it is to be expected that they should be subject to the same control and thus will vary as the velocity head and relative curvature. The angularity of the flow, which is a measure of the spiral velocities relative to the mean downstream velocity, did not appear to vary greatly over the range of test conditions. In all of the runs, the maximum angular deflection which could be observed from dye traces was about $15^{o}$-$20^{o}$ in a thin zone close to the channel bottom; at 1/2" above the bottom, however, the velocities appeared to have little angularity with respect to the curve centerline. The importance of the secondary bottom currents, as related to the shape of the inner separation zone and to sediment transport, is demonstrated in Figure 2 by the infusion of dye to the separation zone (lower right-hand corner of photograph) from the bed of the stream.

The ultimate breakdown of the free vortex patterns and the establishment of a high velocity zone near the outer bank are due to two major factors, the relative importance of which depends on the stream curvature.

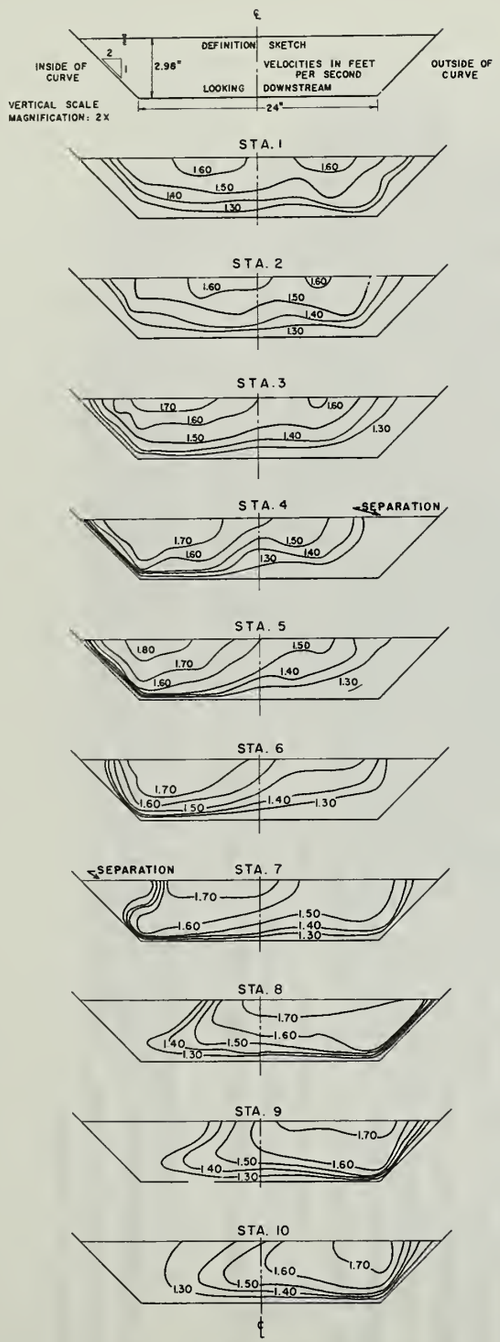


Figure 5. Velocity Distributions by Section, Run No. 1: $y_o$ = 3", $w/y_o$ = 12, $w/r_c$ = 0.6.

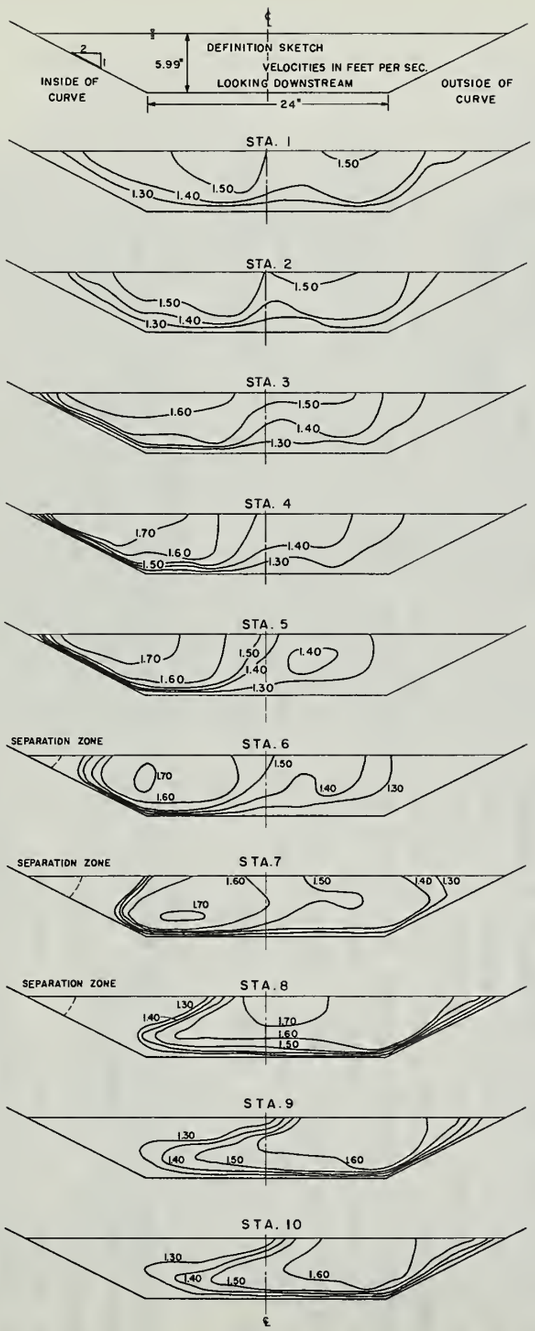


Figure 6. Velocity Distributions by Section, Run No. 4-B, $y_o$ = 6", $w/y_o$ = 8, $w/r_c$ = 0.8.

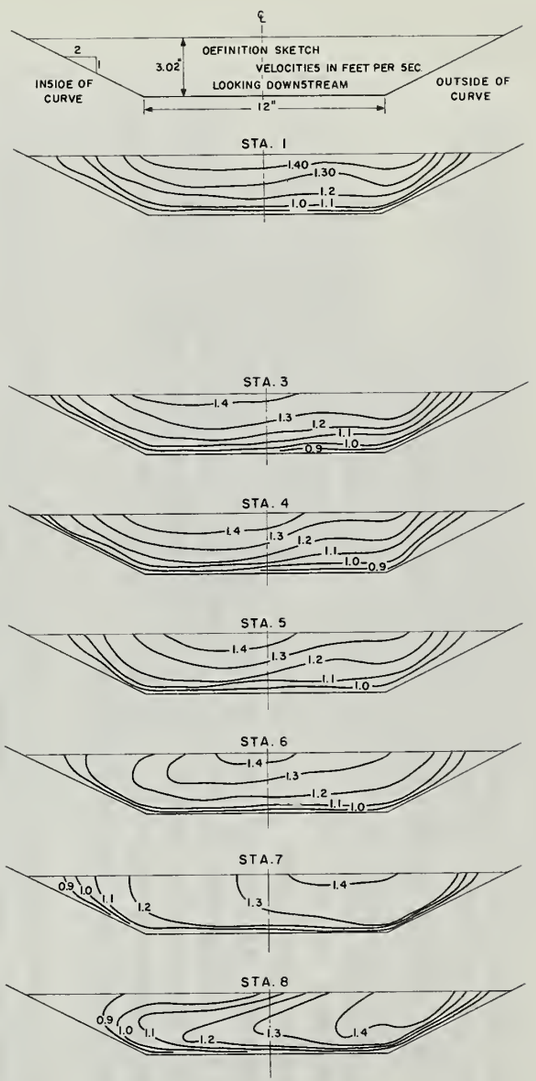


Figure 7. Velocity Distributions by Section, Run No. 6, $y_o$ = 3", $w/y_o$ = 8, $w/r_c$ = 0.34.

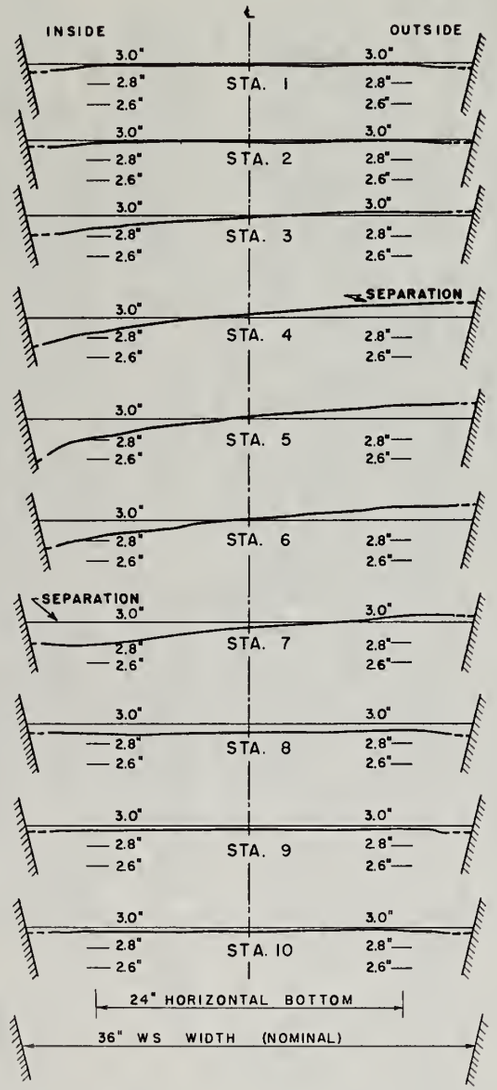


Figure 8. Transverse Water Surface Profiles by Section, Run No. 1: $y_o = 3"$, $w/r_c = 0.6$.

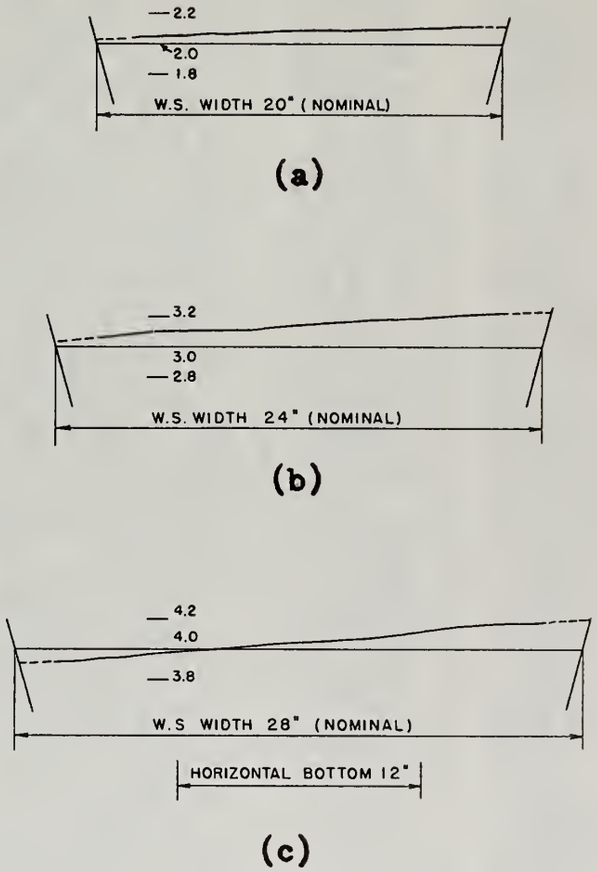


Figure 9. Transverse Water Surface Profiles Shown for Station 5.
(a) Run No. 5: $y_o = 2"$, $w/r_c = 0.29$
(b) Run No. 6: $y_o = 3"$, $w/r_c = 0.34$
(c) Run No. 7: $y_o = 4"$, $w/r_c = 0.40$

1. The helicoidal motion tends to move the high velocity fluid continuously toward the outer bank.

2. The separation zone which originates at the inside of the curve reduces the effective area of the section, resulting in acceleration of the constricted stream and a deflection of the flow away from the inner bank.

In the tests at reduced curvature, Runs 5-7, the first of these factors is clearly dominant. The separation zone remains small yet the high velocities begin to develop along the concave bank midway through the curve.

At higher curvatures (Runs 1-4) however, the separation zone is strongly developed on the inner bank, and the second effect assumes the greater importance. In addition, because of the relatively shorter length of flow in a sharper curve, the helicoidal motion is not as fully developed, and the momentum transfer by this means is greatly reduced. This dominant action of the separation zone was demonstrated in the tests of the simulated reverse curve systems (Runs 11 and 13), which are discussed in a later section. In the latter tests, which were conducted at conditions similar to those of Runs 2 and 4-A, the higher velocities in the entrance flow were diverted toward the inner bank, preventing the formation of the separation zone. Dye traces showed that the helicoidal motion was undiminished, yet for these conditions the high velocity zone did not develop on the outer bank.

The further persistence of the flow asymmetry in a long straight reach following the curve could not be determined in these tests. The channel was too short to permit a return to normal flow, but, from the similarity between the distributions at Stations 9 and 10, of both velocity and shear, it is evident that such a return would be quite gradual requiring a considerable length of straight channel below the curve. Shukry (39) found that uniform flow is not re-established for a distance of at least eight stream widths, while investigations on pipe bends have shown that the rate of headloss may not return to normal within a length of less than fifty pipe diameters (2)(21). The distance of recovery following a curve is subject to great variation as it depends on the degree of non-uniformity produced by the curve itself. In general it may be surmised that this recovery length will be of the order of the distance required to establish a normal boundary layer.

c. Boundary Shear Stress: The distribution of shear stresses in the approach flow is in general agreement with the results reported by Enger (1) on tests performed in a straight channel of similar trapezoidal section lined with sand-gravel mixtures. In Figure 10, the shear distributions at Station 1 are shown for the complete series of tests in the single curve. For comparison, data from the rough surface tests, Runs 8 and 9, are included, as well as from several of Enger's tests.

The fact that the shears measured in the gravel-lined channel

show a somewhat greater scatter emphasizes the difficulties encountered in working with streams through non-homogeneous materials. While the shears measured in both the smooth and rough channels appear quite consistent, it must be borne in mind that, in natural streams, greater variation is to be expected in the local tractive, or scouring, forces.

The close physical relationship between the boundary shear and velocity patterns is shown by comparison of Figures 5, 6, and 7 with the corresponding shear maps, Figures 11, 14, and 16. That the shear pattern should be governed by the velocity distribution is to be expected. Beneath a zone of high velocity, the gradient of velocity and, hence, the local rate of momentum transfer are increased, resulting in higher shear stresses. However, the ability to relate boundary shear stress to local velocities presupposes a rather idealized boundary layer, which may be described by a single velocity distribution function. While such a law is realized for the flow immediately adjacent to the boundary (19), non-uniformity in the curving stream prevents such general formulation for the full depth of flow, and the relation between the shear distribution and the gross velocity patterns can only be considered on a qualitative basis.

Comparison of the shear maps, Figures 11-17, reveals certain trends in the variations in shear patterns with stream geometry. The maps for the tests at greater curvature (Runs 1-4) are essentially similar, showing the higher stresses developed on the inner bank through most of the curve and on the outer bank only below Station 7. With decreasing curvature the suppression of the free vortex motion becomes more evident in the shear maps. Thus, while high shears occur on the inner bank in Run 7, the crossover of the shear pattern is developed between Stations 5 and 6. In Run 6, the inner bank shears are greatly diminished and the crossover occurs at Station 5; while in Run 5, the asymmetry of the shear pattern in the beginning of the curve is barely perceptible.

Closely allied with the above trend is the change in location of the maximum local shear stress with variation in stream depth and curvature; with increasing depth and curvature the location of the highest shear shifts upstream from the outer bank to the inner part of the curve. In Runs 5, 6, 7, 1, and 2 the maximum shear was measured near the outer bank in the downstream tangent. In Run 3, there are three points of high shear, the maximum occurring high on the inner bank at Station 4; while in Run 4, the maximum occurs at Station 7, with high shears extending above Station 3 along the bank.

An evaluation was made of the average relative shear over the entire test reach affected by the curve, from Stations 1 through 9. The variation of the ratio $\overline{\tau_L}/\overline{\tau_o}$ with relative curvature, $w/r_c$, which is shown in Figure 35, suggests a trend of increasing average shear with increasing curvature. It should be borne in mind, however, that for the range of curvatures studied, the total variation observed in $\overline{\tau_L}/\overline{\tau_o}$ is of the same order of magnitude as the experimental error inherent in the

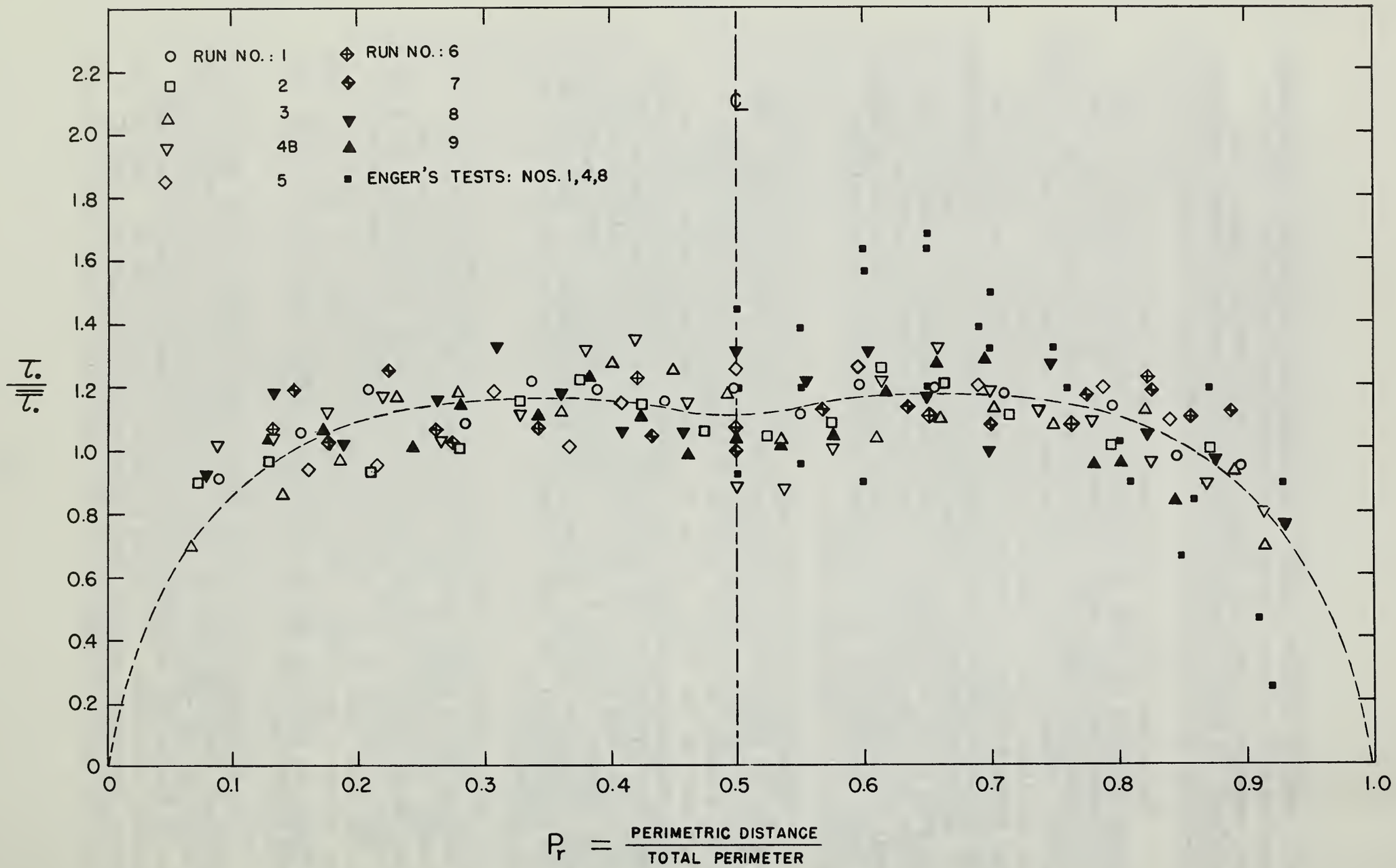


Figure 10. The Peripheral Distribution of Local Boundary Shear Stresses in Straight Trapezoidal Channels (facing downstream).

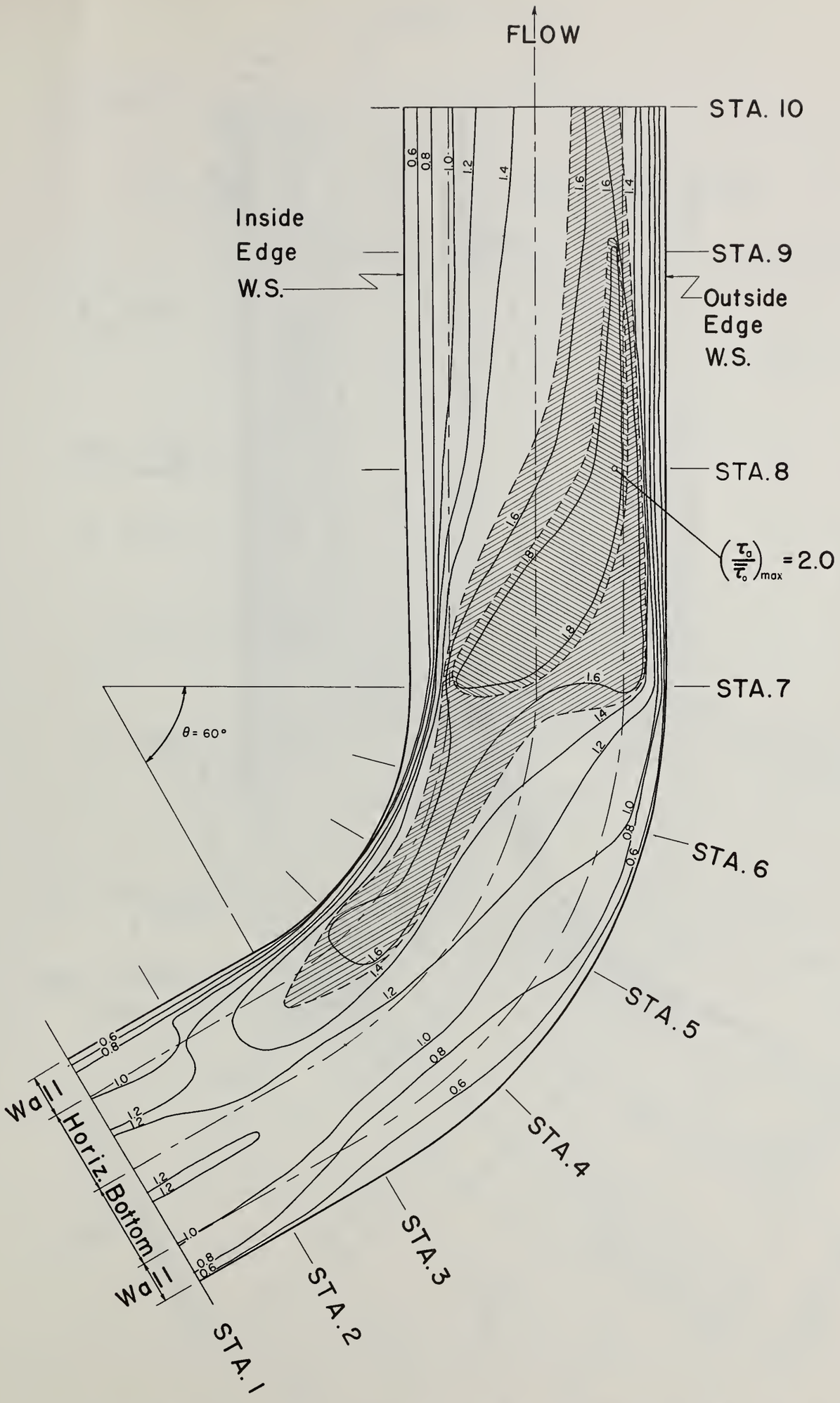


Figure 11. The Distribution of Boundary Shear Stresses in the Curved Reach Shown by Contours of $\tau_o / \overline{\tau_o}$; Run No. 1: smooth channel, $b/r_c = 0.42$, uniform approach, $y_o = 2.98"$, $w/y_o = 12$, $w/r_c = 0.6$, $\overline{\tau_o} = 0.0070$ psf.

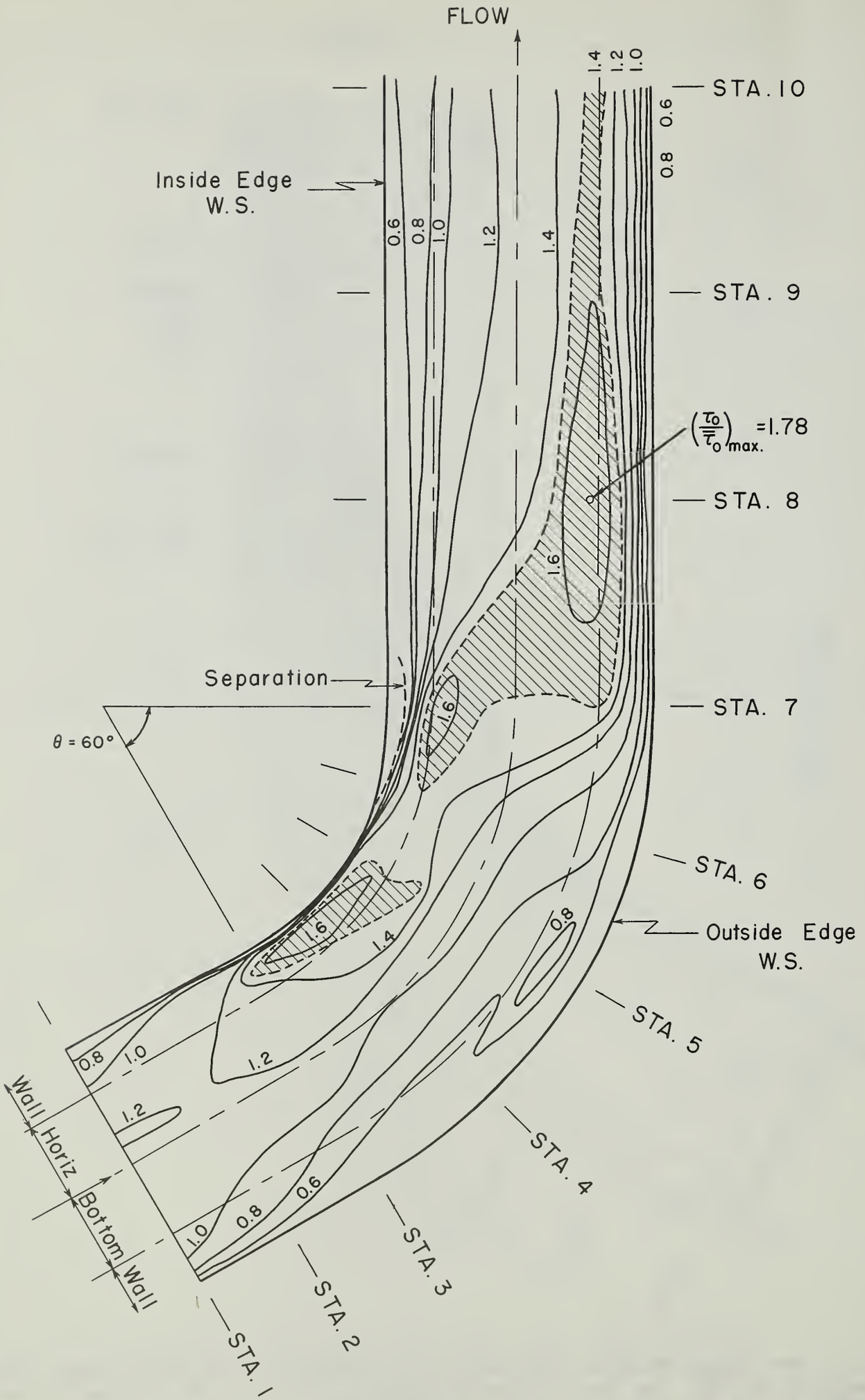


Figure 12. The Distribution of Boundary Shear Stresses in the Curved Reach Shown by Contours of $\tau_o/\overline{\tau_o}$; Run Nos. 2-A and B: smooth channel, $b/r_c = 0.42$, uniform approach, $w/y_o = 10$, $w/r_c = 0.67$, (A): $y_o = 3.86"$, $\overline{\tau_o} = 0.0087$ psf., (B): $y_o = 4.00"$, $\overline{\tau_o} = 0.0088$ psf.

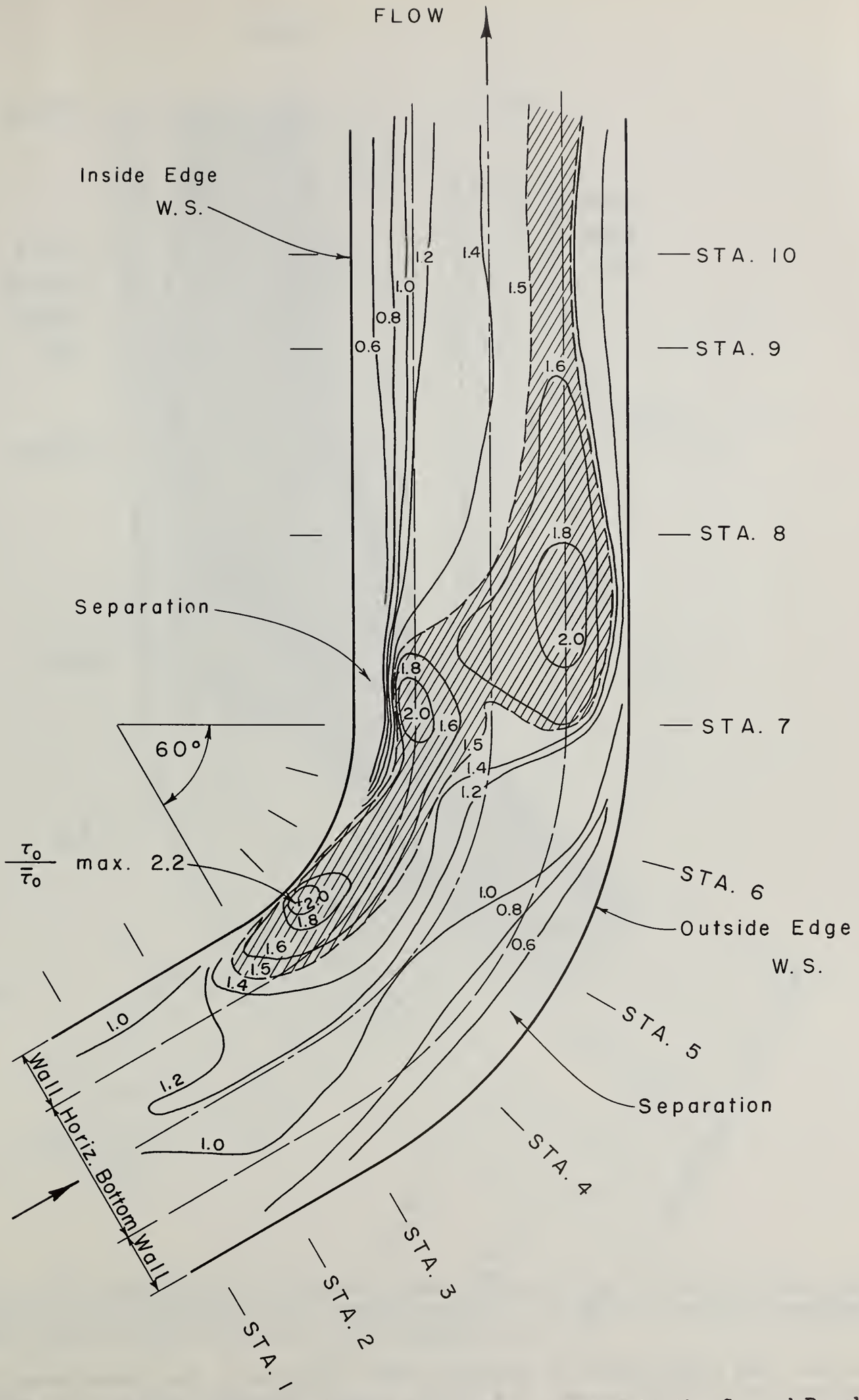


Figure 13. The Distribution of Boundary Shear Stresses in the Curved Reach Shown by Contours of $\tau_o / \overline{\tau_o}$; Run Nos. 3-A and B: smooth channel, $b/r_c = 0.42$, uniform approach, $w/y_o = 8.8$, $w/r_c = 0.73$, (A): $y_o = 5.08"$, $\overline{\tau_o} = 0.0101$ psf., (B): $y_o = 5.08"$, $\overline{\tau_o} = 0.0121$ psf.

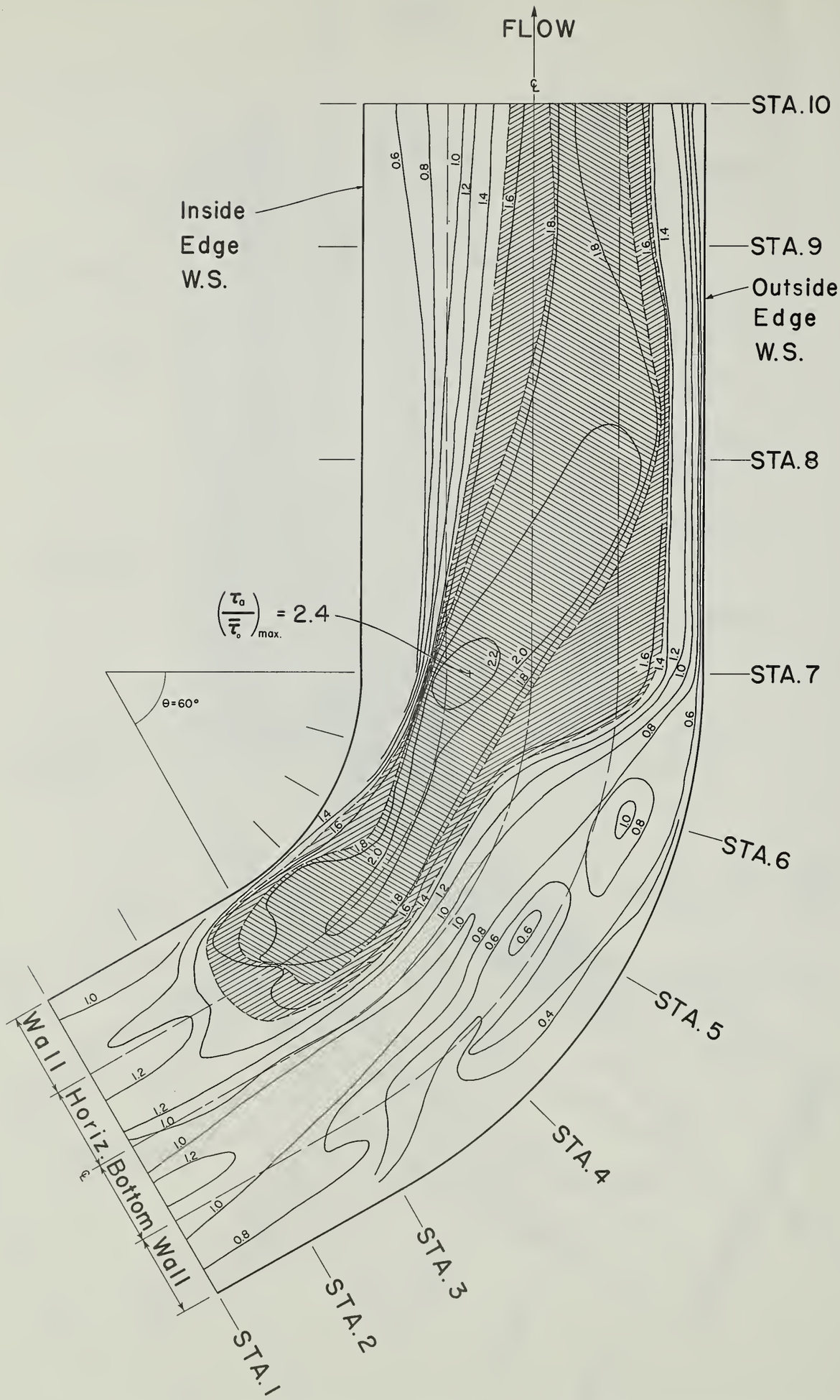


Figure 14. The Distribution of Boundary Shear Stresses in the Curved Reach Shown by Contours of $\tau_o / \overline{\tau_o}$; Run Nos. 4-A and B: smooth channel, $b/r_c = 0.42$, uniform approach, $w/y_o = 8$, $w/r_c = 0.8$, (A): $y_o = 6.00"$, $\overline{\tau_o} = 0.0148$ psf., (B): $y_o = 5.99"$, $\overline{\tau_o} = 0.0060$ psf.

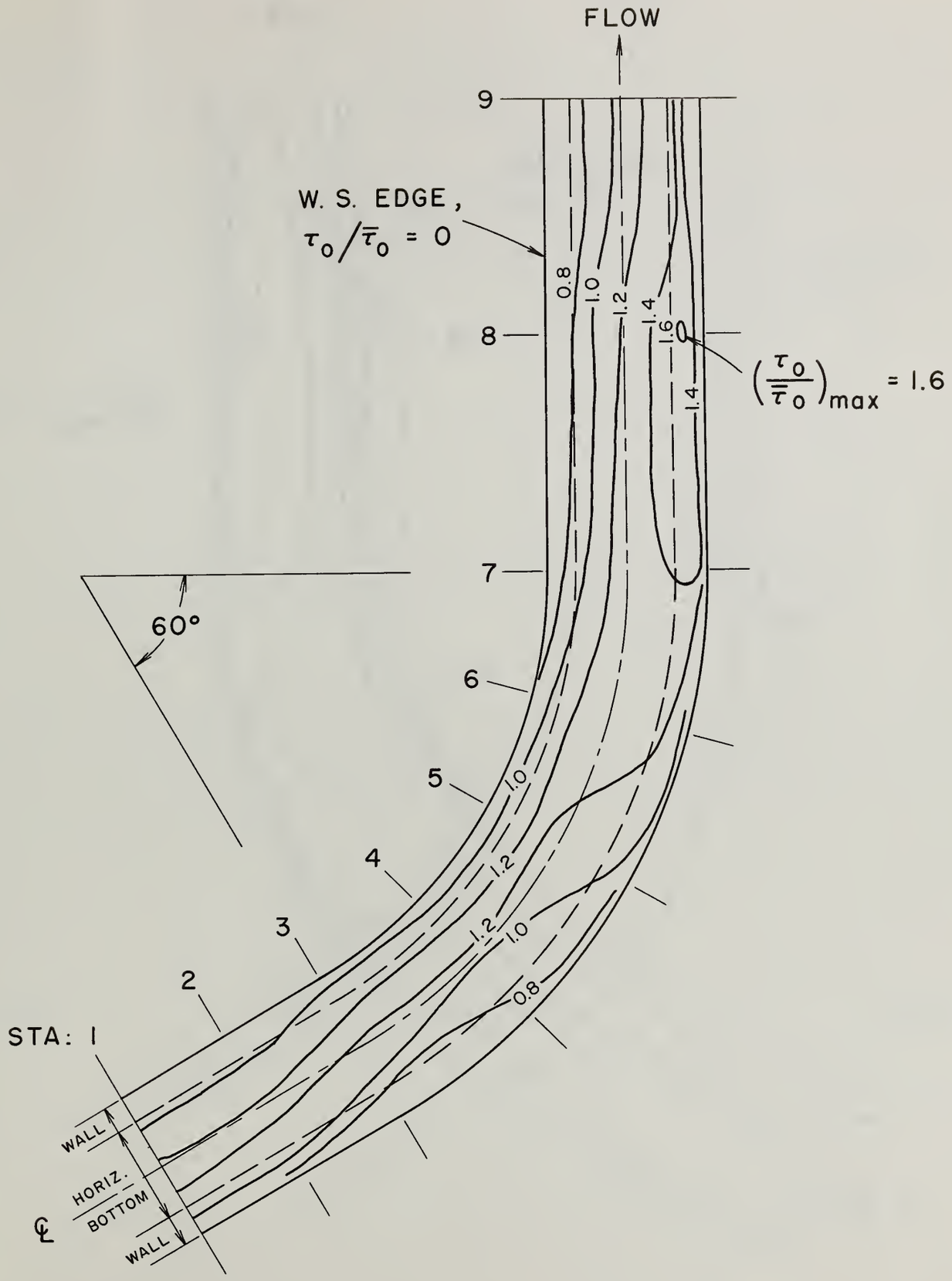


Figure 15. The Distribution of Boundary Shear Stresses in the Curved Reach Shown by Contours of $\tau_o/\overline{\tau_o}$; Run No. 5: smooth channel, $b/r_c = 0.17$, uniform approach, $w/y_o = 10$, $w/r_c = 0.29$, $y_o = 2.01"$, $\overline{\tau_o} = 0.0034$ psf.

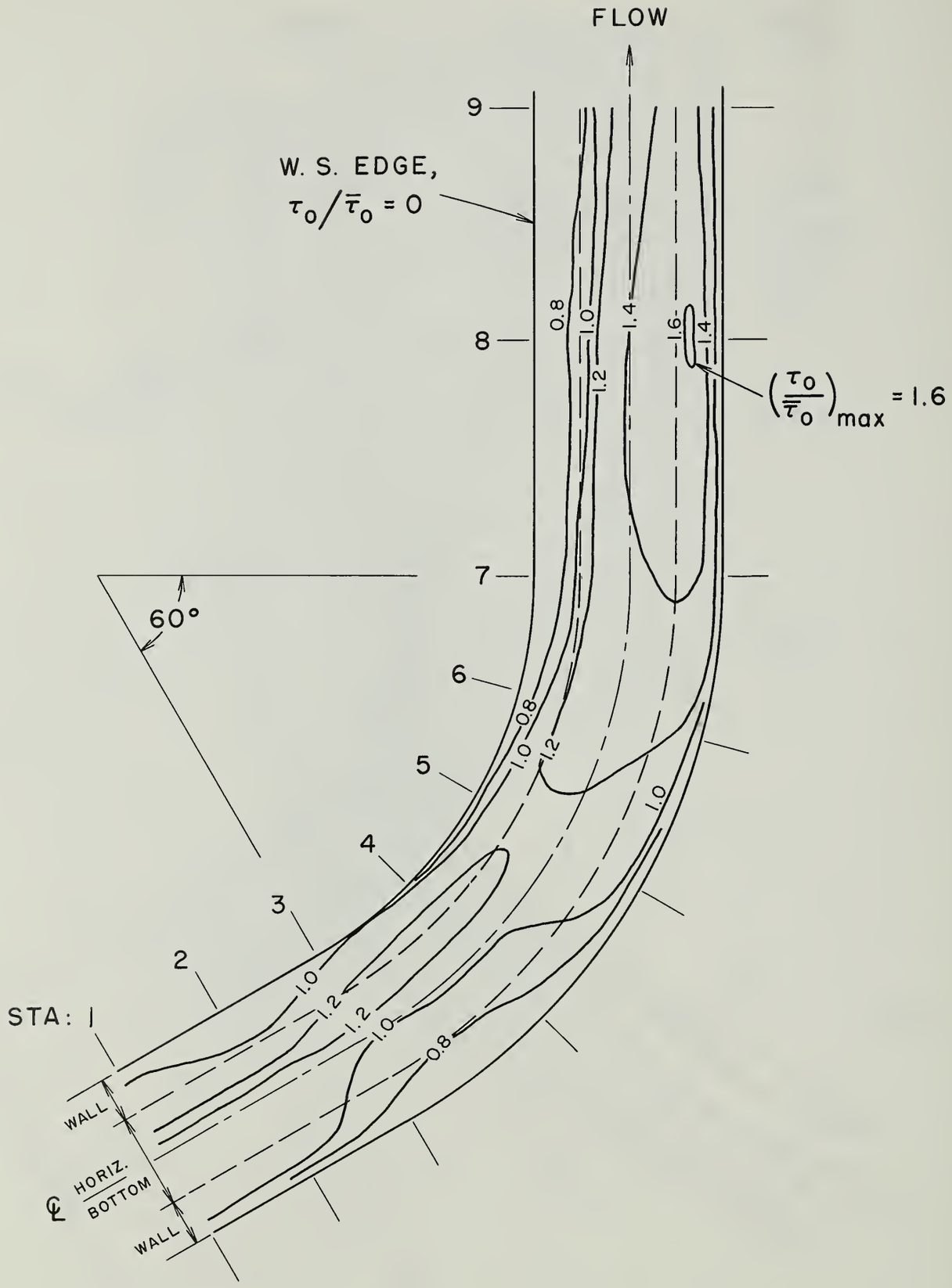


Figure 16. The Distribution of Boundary Shear Stresses in the Curved Reach Shown by Contours of $\tau_o/\bar{\tau}_o$; Run No. 6; smooth channel, $b/r_c = 0.17$, uniform approach, $w/y_o = 8$, $w/r_c = 0.34$, $y_o = 3.02"$, $\bar{\tau}_o = 0.0055$ psf.

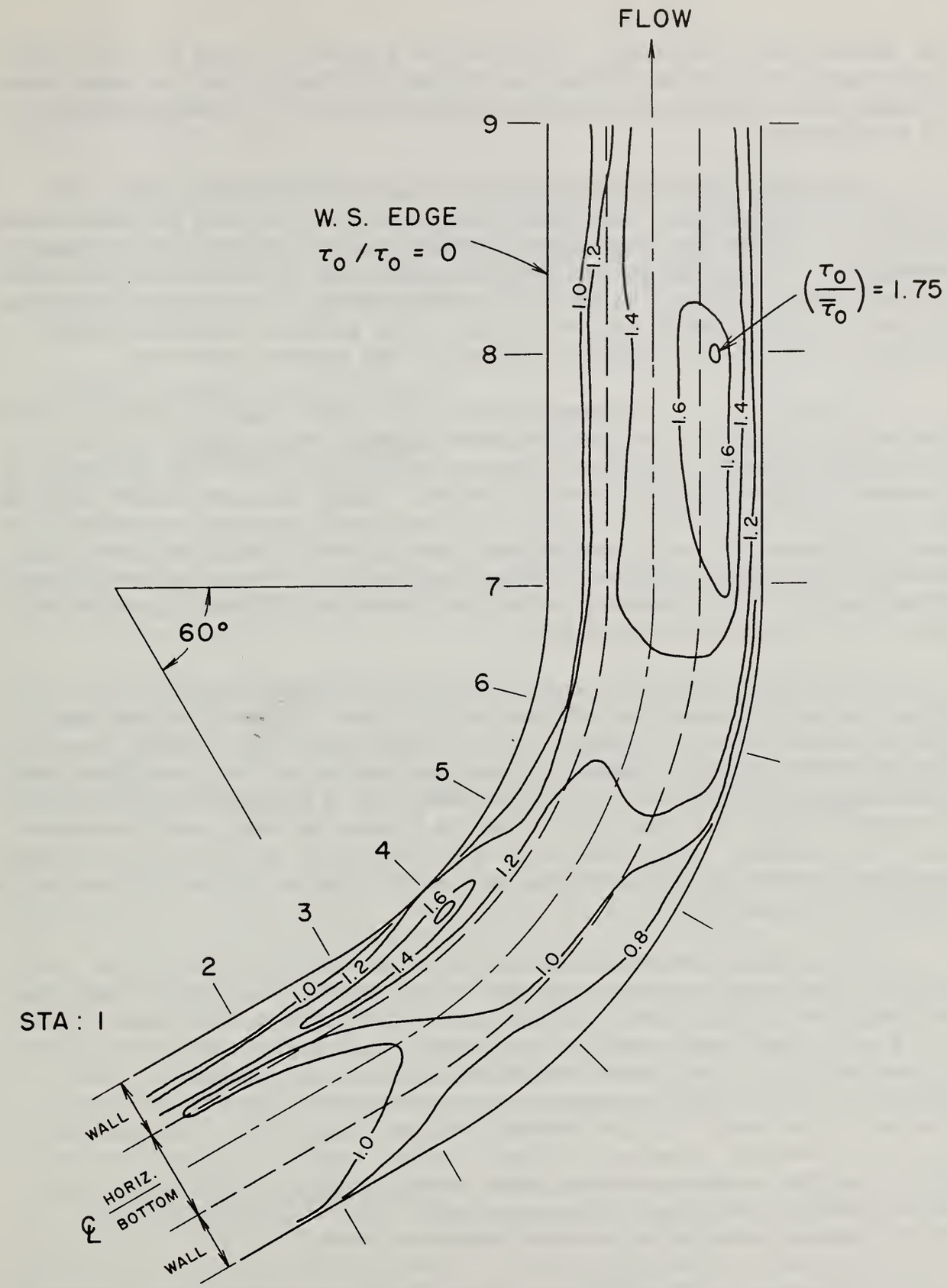


Figure 17. The Distribution of Boundary Shear Stresses in the Curved Reach Shown by Contours of $\tau_o / \overline{\tau_o}$; Run No. 7: smooth channel, $b/r_c = 0.17$, uniform approach, $w/y_o = 7$, $w/r_c = 0.4$, $y_o = 3.98"$, $\overline{\tau_o} = 0.0074$ psf.

shear measurement technique. Thus, while a greater range in $w/r_c$ would be necessary in order to define the variation in $\overline{\tau_L}/\overline{\tau_o}$, the trend shown in Figure 35 is clearly indicative of the effect of stream curvature on bend resistance.

The tests conducted at similar ratios of width to depth are indicated in Figure 35. For Runs 2 and 5, $w/y_o = 10$, and for Runs 4 and 6, $w/y_o = 8$. With the very limited amount of data available for this comparison, no trend could be observed simply on the basis of the cross-sectional shape of the stream. It seems reasonable to assume, however, that the effect of depth per se on the shear pattern should be less important and that the dominant factor is the stream curvature.

In addition to the comparison of the mean relative shear stresses shown in Figure 35, plots were prepared showing the variation with $w/r_c$ of the maximum local relative shear, as well as of the area enclosed by a contour of given relative shear stress. While the mean shear, $\overline{\tau_L}/\overline{\tau_o}$, is of interest as an indication of the bend resistance, the information given in Figures 36 and 37 is perhaps more directly applicable to the problem of revetment design in channel curves. In spite of considerable scatter in the data, there is an evident trend of increasing relative shears with increasing curvature.

It is of interest to note that in the earlier report (19), which did not include the results of Runs 5-7, it was stated that the mean relative shear in Run 2 appeared to be inexplicably lower than those of the other three tests. However, from the results of the completed test series (Figures 35-37), it is evident that Run 2 conforms quite well to the general trend and that the relative shears in Run 1 are somewhat high. The possible significance of the deviations of Runs 1 and 2 from the general trend is discussed in the section below on Energy Dissipation in the Test Reach (V-D).

The greater deviation of Run 1 may be due to error in the calibration of the static pressure probe in the Model II surface Pitot tube, which was used in the test. At the time of the first four tests, Runs 2 and 3 were completely verified with different instruments, but since the results of Run 1 appeared reasonable it was not checked. After completion of the full test series, the remainder of which was conducted with the Model III instrument, it was found that the Model II calibration becomes uncertain at low depths, tending to give substantial positive errors in the computed local shears. It is unfortunate that this calibration error was discovered after the alteration of the channel, which prevented a re-examination of Run 1.

In Figure 36 it will be noticed that the maximum local shear in Run 1 conforms to the indicated trend while that in Run 2 appears to be too low. While this may indeed be the case, it should be recognized that measurement of the point of extreme shear is statistically uncertain for the relatively small sampling of the total stream bed areas, which was necessary in these tests. Thus, a more reliable criterion of the

variation between tests is the mean relative shear, or, alternatively, the percentage of the test reach affected by a given intensity of relative shears.

From these tests it can be concluded that the boundary shear stresses in a channel curve vary with the flow conditions and, with the shear stresses, appear to be functions primarily of the stream geometry. For the range of conditions tested in 60-degree curves, $7 < w/y_o < 12$ and $1.75 < r_o/w < 4$, the maximum local shears, expressed as $\tau_o/\overline{\tau_o}$, are of the order of 2.

2. Rough Channel, Runs 8 and 9

a. Entrance Conditions: As with Runs 1-7 discussed previously, the flow at the entrance to the curve in the rough channel is essentially symmetrical about the channel axis (Figures 10,18,19). While there is no expression analogous to Equation (10) for the estimation of the boundary layer over a rough surface, it may be inferred that the boundary layer was fully developed in both tests. The decrease in Reynolds number and the increased coefficient of friction for the rough channel would both lead to a more rapid development of uniform flow.

b. Flow through the Curve: The tendency towards free vortex motion is again evident in the velocity distributions and water surface configurations for flow through the rough channel. Comparison of Figure 18 with Figure 6 shows that the gross characteristics of the flow are essentially unchanged by the introduction of boundary roughness to a bend of a given geometry.

For channels of equal cross section and slope, but of different roughnesses, the mean shear stress over the full perimeter at uniform flow, $\gamma RS_e$, is a constant, independent of the roughness. Any variation in the friction factors for different channels requires an inverse variation in the mean velocity head of the stream in order to maintain uniform conditions. While it was not possible to duplicate exactly the conditions of the corresponding smooth channel tests, a comparison of the values of $\overline{\tau_o}$ and $\gamma RS_e$ in Table II for Runs 2 and 8 and Runs 4-B and 9 shows that the magnitudes of the mean shears at each depth are indeed independent of the boundary roughness.

c. Boundary Shear Stress: The general patterns of the boundary shear distributions for these tests are quite similar to those in the corresponding smooth channel tests. As a result of the predominant free vortex type of motion the stresses in the early part of the curve are greatest on the convex bank. Towards the exit of the curve the transfer of high momentum fluid to the outer bank causes increased shears along the outer edge of the stream.

However, a comparison of Figure 20 with Figure 12, and Figure 21 with Figure 14 reveals certain deviations from the smooth channel patterns.

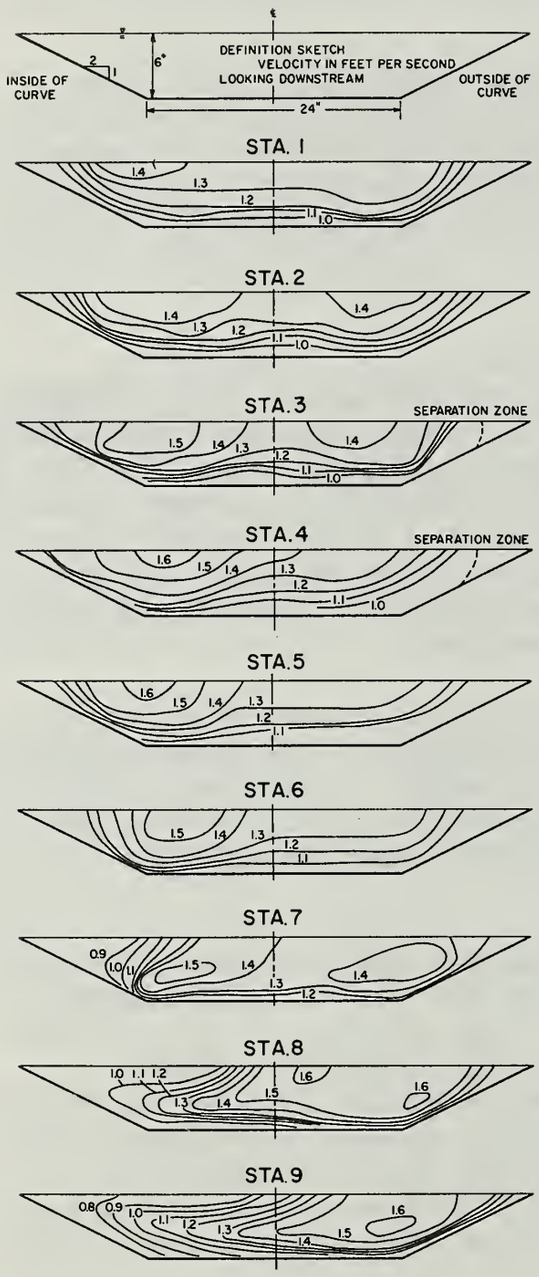


Figure 18. Velocity Distributions by Section, Run No. 9, Rough Channel, $y_o$ = 6", $w/y_o$ = 8, $w/r_c$ = 0.8.

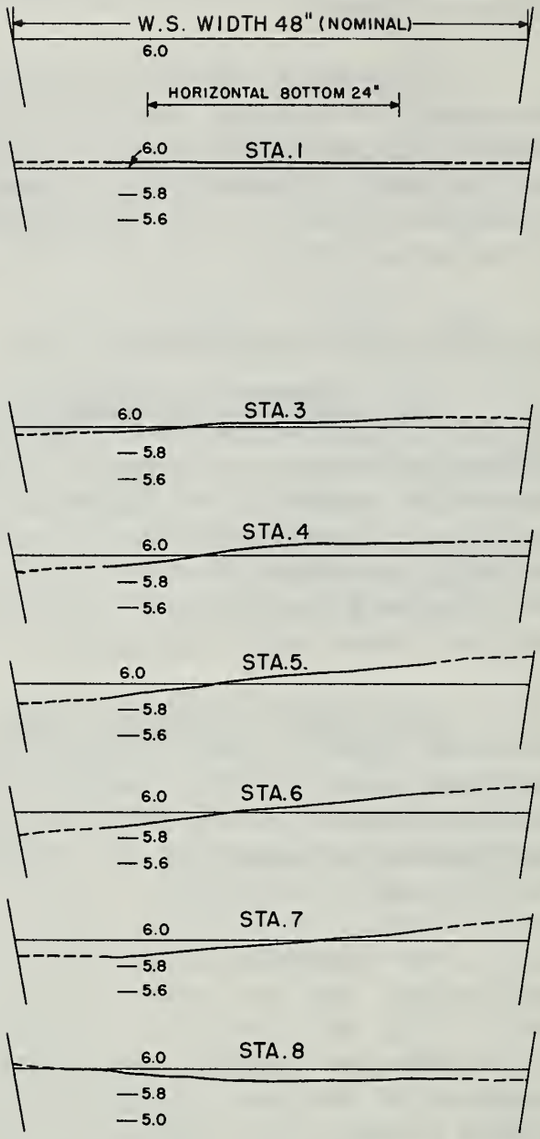


Figure 19. Transverse Water Surface Profiles by Section, Run No. 9.

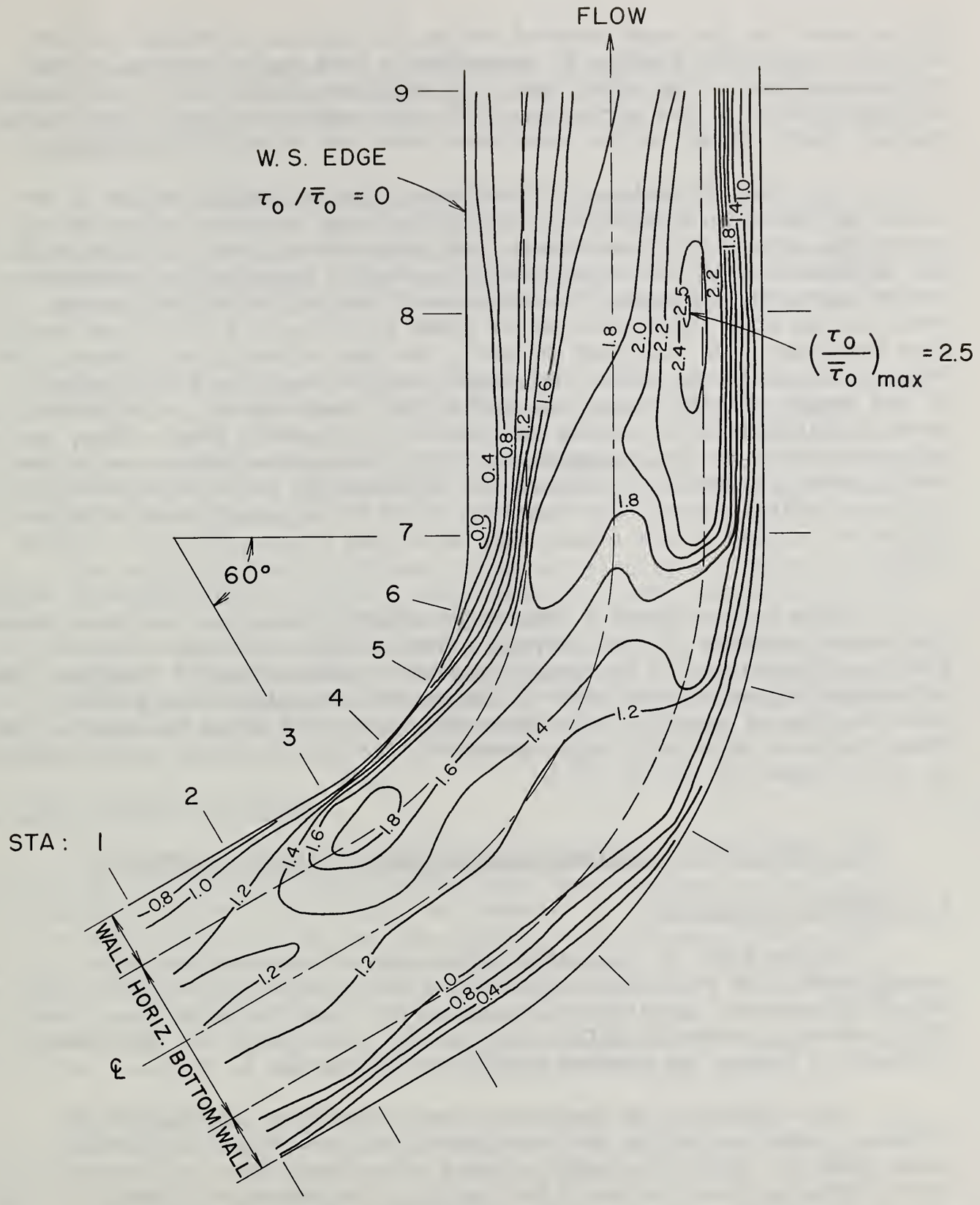


Figure 20. The Distribution of Boundary Shear Stresses in the Curved Reach Shown by Contours of $\tau_o / \overline{\tau_o}$; Run No. 8: rough channel, $b/r_c = 0.42$, uniform approach, $w/y_o = 10$, $w/r_c = 0.67$, $y_o = 3.94"$, $\overline{\tau_o} = 0.0085$ psf.

In the maps for the rough channel tests, the initial crossover pattern is quite evident at Station 6, suggesting a more rapid transfer of the stream momentum to the outer bank. In addition, while the shear stresses throughout most of the curve are of the same magnitudes as in the smooth channel tests, those in the downstream reach are considerably higher.

In order to explain this behavior, the helicoidal motion in the curve may again be considered. Due to the rough boundary, which prevented the motion of dye crystals and also caused a rapid diffusion of the aqueous dye, it was not possible to clearly evaluate the secondary bottom currents. However, the presence of the helicoidal motion was obvious, and some inferences can be drawn regarding its effect on the flow structure. In the rough channel, the mean velocity and, hence, the superelevation in the curve are lower than for the same curve geometry in the smooth channel. Near the bed of the rough channel, a relatively greater thickness of the fluid is retarded by boundary drag. Thus, a greater portion of the stream will undergo transverse motion due to the radial pressure gradient. The result of this will be to accelerate the crossover bringing more high momentum fluid to the outer bank, with an ultimate increase in the attack exerted by the stream along the outside bank.

From the two tests in the rough channel it may be concluded that the general pattern of flow through a bend of given curvature is not greatly affected by the boundary roughness. With increased roughness the helicoidal motion affects more of the stream, resulting in a greater concentration of momentum and higher shear stresses along the outer. For these tests at relatively high curvature, the maximum local shear stress is of the order of $\tau_o / \overline{\tau_o} = 2.5$.

## B. Tests with Simulated Compound Curve Systems: Runs 10-13

### 1. Entrance Conditions

In the tests of simulated double and reverse-bend patterns, the approach flow was deliberately distorted in order to determine the effect of upstream curvature on the boundary shear distribution. For this purpose, systems of baffle screens were installed near the channel entrance to impose the desired conditions at Station 1.

The simulation of the double-bend pattern was established as follows: using as models the downstream shear and velocity distributions taken in the corresponding single curve tests (Run 2, Station 8 for Run 10; Run 4-A, Station 9 for Run 11), the screen sets were adjusted until these same distributions were obtained at Station 1. Figures 22 and 23; a, b, and e, show the comparison of the desired patterns with those obtained by this technique.

The reverse-bend patterns were obtained in a similar way by screens placed on the opposite side of the channel. For these tests

the downstream distributions of velocity and shear from Runs 2 and 4-A were reversed, and the inverted patterns used as models. The desired and obtained distributions are shown for the reverse-bend tests in Figures 24 and 25;a, b, and e.

In each case the major portion of the screen system was located as far upstream as possible. This produced a more gradual shift of the velocity distribution near the entrance to the curve, without creating major surface disturbances. The screen arrangement for each test is shown schematically in the inset sketch on the appropriate shear map (Figures 28-31).

The baffle screens caused non-uniform conditions which prevented the determination of approach flow gradient and which also increased the average shear stress at Station 1 to a value greater than that measured at conditions of uniform approach. In the calculation of $\tau_o / \overline{\tau_o}$, therefore, the average shear, $\overline{\tau_o}$, was used as determined in the single curve series for Runs 2 and 4-A.

The modifying screen systems produced velocity and shear distributions corresponding to the exit conditions of a curve upstream of the channel bend. It was unnecessary to reproduce a helicoidal motion, since below the curve exit the superelevation and, hence, the secondary current abates rapidly. Since the degree of similitude that can be attained with simple screen arrangements is limited, the shear patterns obtained from the compound curve series should be regarded as being somewhat qualitative.

## 2. Flow through the Curve

The overall pattern of flow through the curve was not greatly affected by the velocity distributions which were imposed at Station 1. The helicoidal pattern could again be detected by dye traces, although the increased turbulence of the flow caused a more rapid diffusion of the dye. As might be expected, the separation zone on the same side of the flume as the higher velocities was reduced while that on the opposite bank was increased in extent. In the reverse-bend tests, the roller on the convex bank was barely evident, and, in the double-bend tests, reduced velocities occurred on the concave bank without reversed flow.

The shapes of the water surface profiles (Figures 26,27) for the double and reverse curves varied somewhat from those measured in the single curve tests. The profile at Station 5 for the double curve test shows the effect of the higher velocities along the outer bank, with a broad stagnant zone on the inner part of the bend. In the reverse bend tests, the separation zone on the inner bank is reduced, and the profiles are accordingly steeper near the inside edge throughout the curve.

In spite of the gross variations in velocity distributions imposed on the flow, the maximum superelevations measured in these tests are essentially the same as those for the corresponding single curve tests.

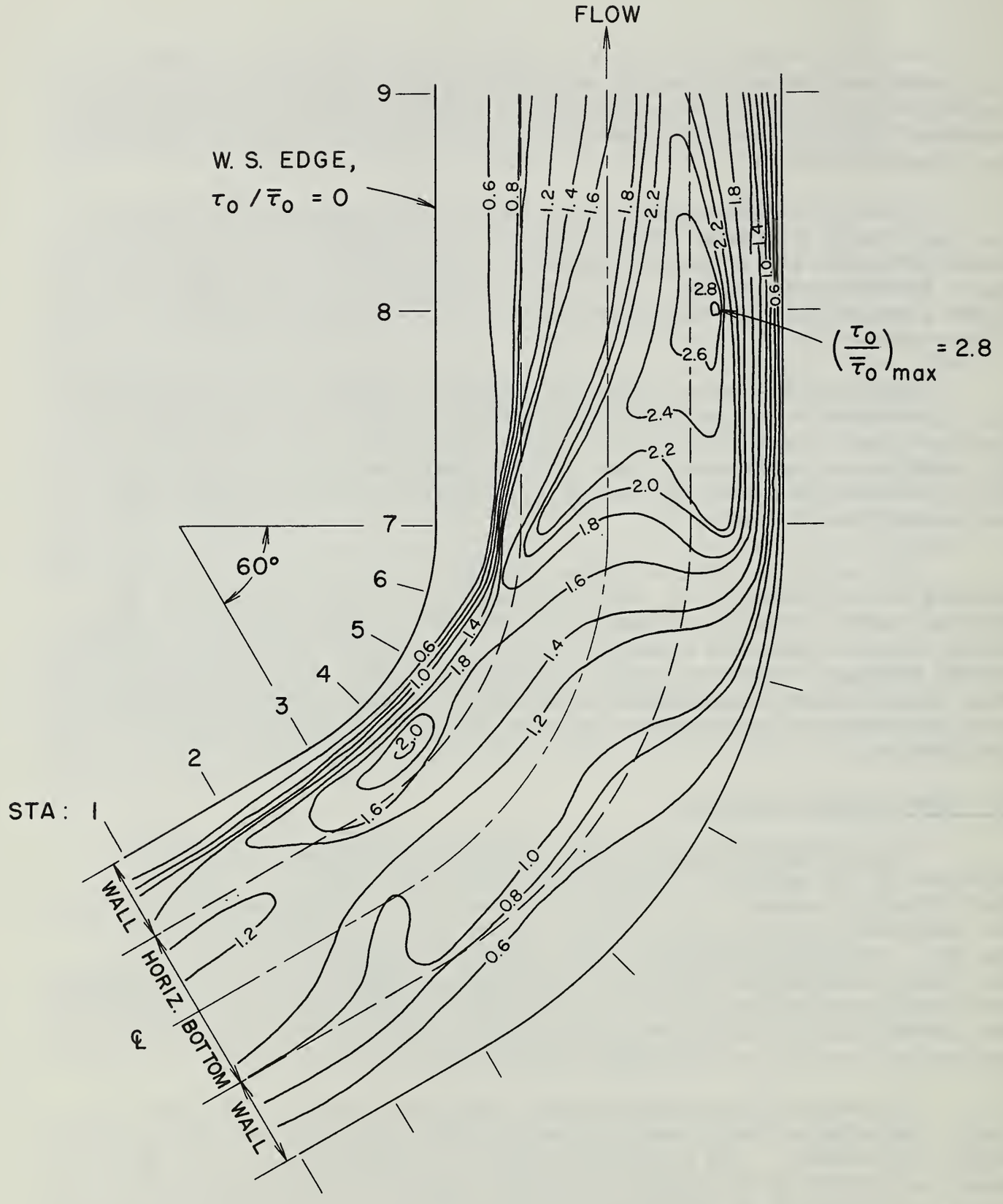


Figure 21. The Distribution of Boundary Shear Stresses in the Curved Reach Shown by Contours of $\tau_o / \overline{\tau_o}$; Run No. 9: rough channel, $b/r_c = 0.42$, uniform approach, $w/y_o = 8$, $w/r_c = 0.8$, $y_o = 6.05"$, $\overline{\tau_o} = 0.012$ psf.

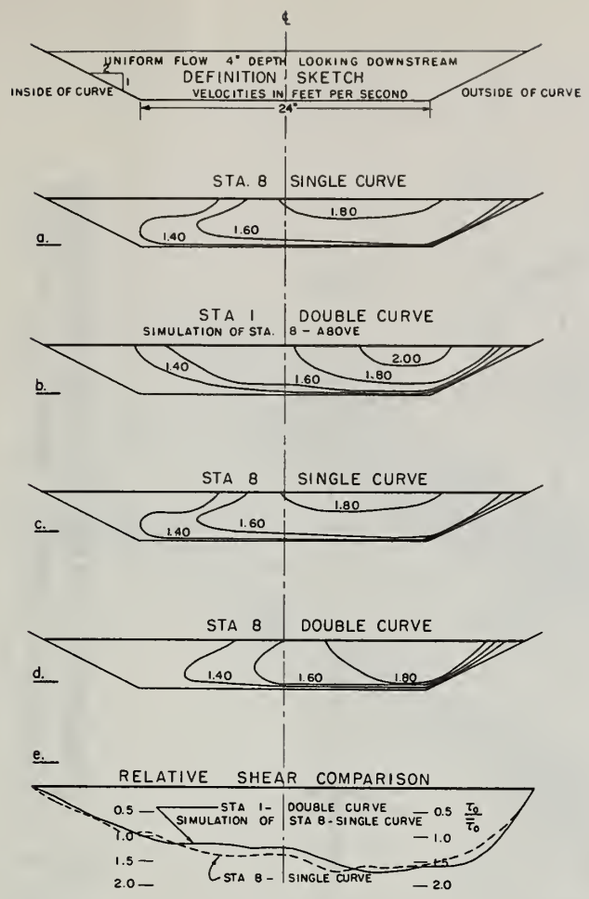


Figure 22. Run No. 10: Double Curve, $y_o$ = 3.86", $\overline{\tau_o}$ = 0.0081 psf.

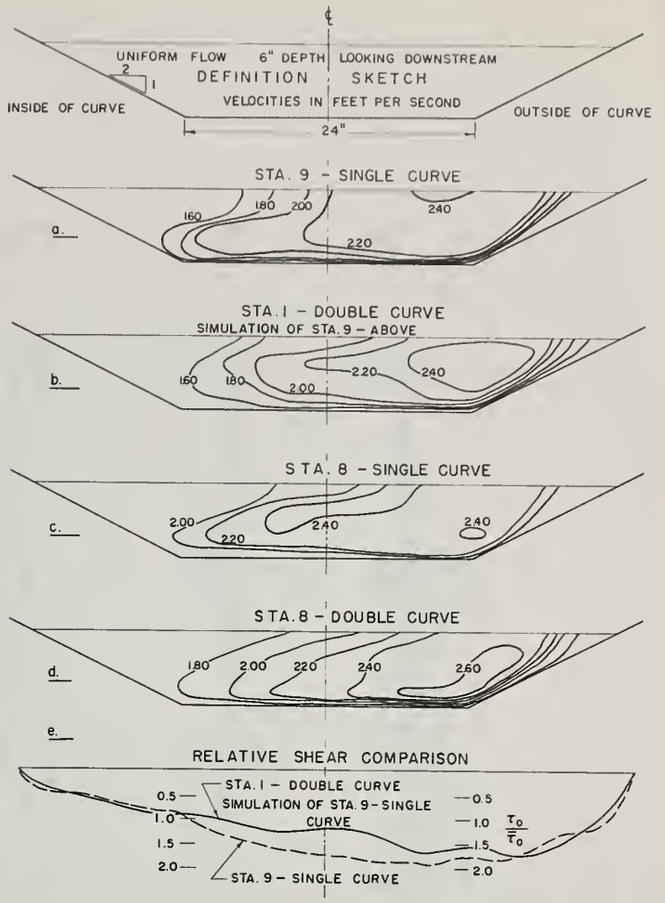


Figure 23. Run No. 11: Double Curve, $y_o$ = 6.00", $\overline{\tau_o}$ = 0.0123 psf.

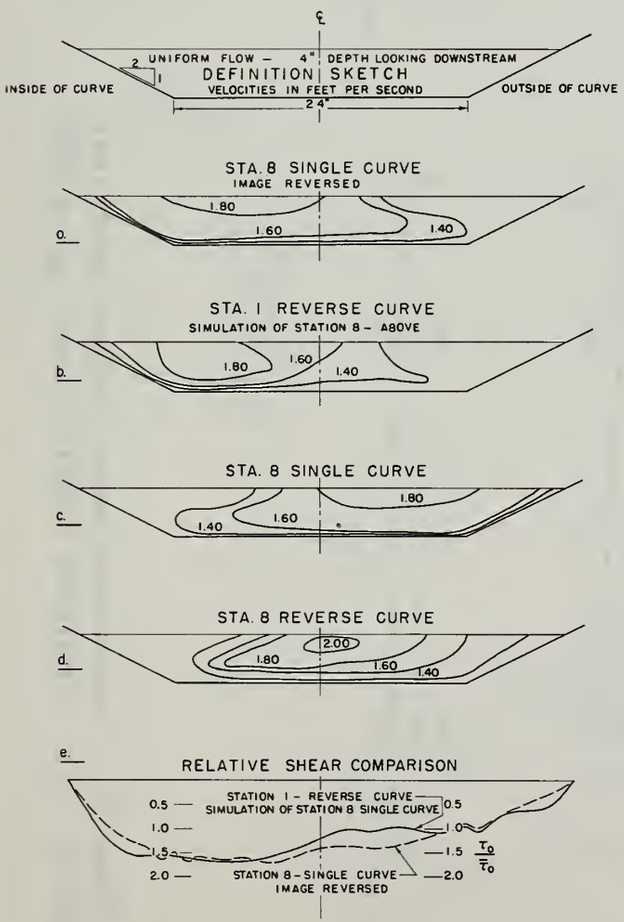


Figure 24. Run No. 12: Reverse Curve, $y_o$ = 3.86", $\overline{\tau_o}$ = 0.0081 psf.

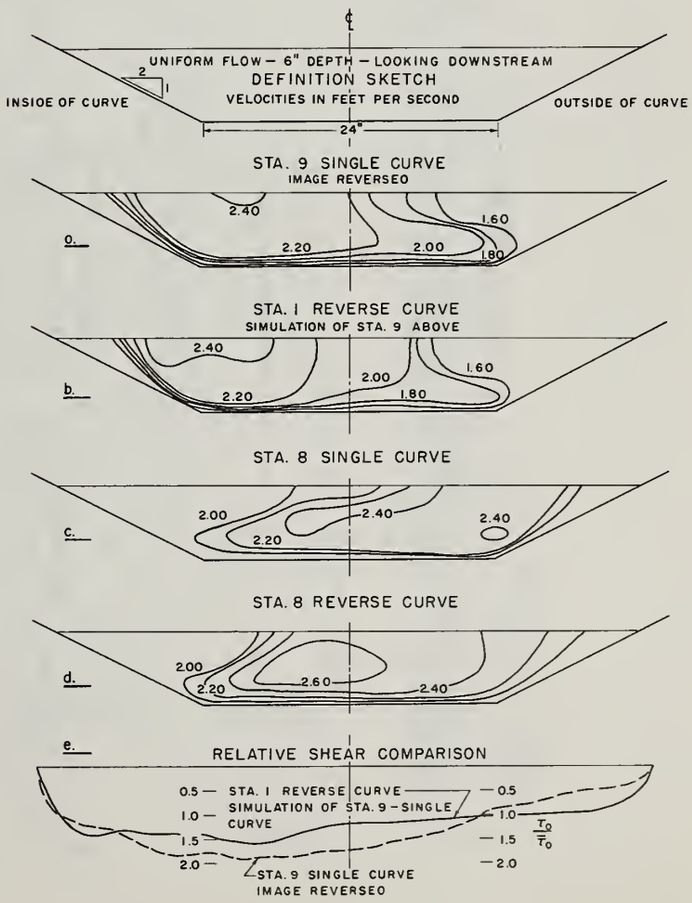


Figure 25. Run No. 13: Reverse Curve, $y_o$ = 6.00", $\overline{\tau_o}$ = 0.0123 psf.

Figures 22,23,24,25. Shear and Velocity Patterns Obtained for the Simulated Compound Curve Systems. The four tests were performed in the smooth channel, $b/r_c$ = 0.42.

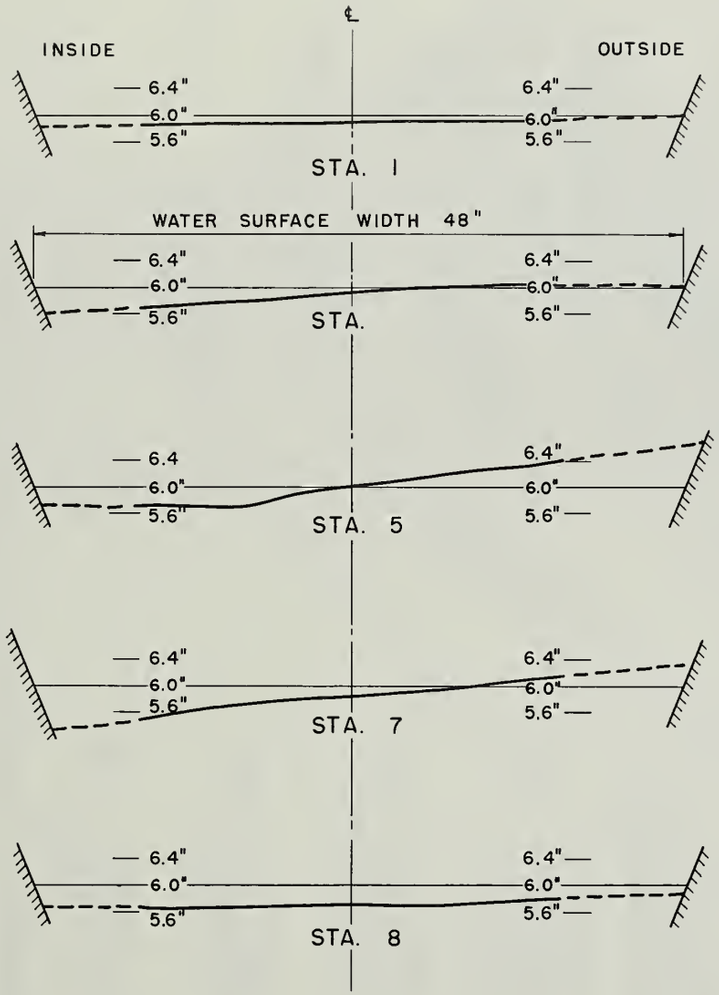


Figure 26. Transverse Water Surface Profiles; Run No. 11: Simulated Double Curve, $y_o = 6.00"$.

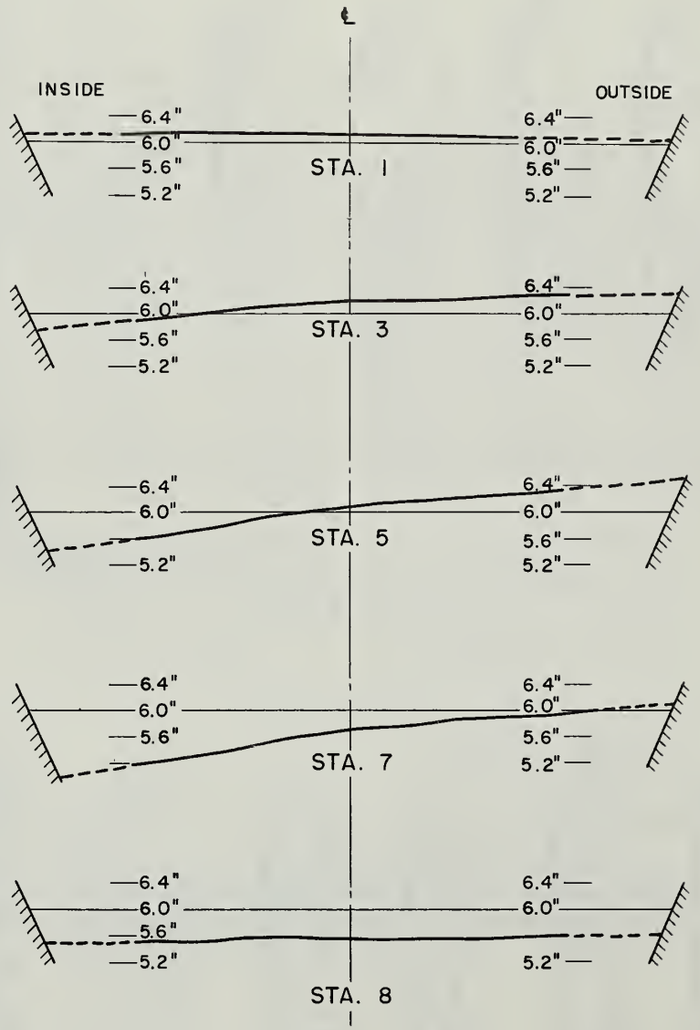


Figure 27. Transverse Water Surface Profiles; Run No. 13: Simulated Reverse Curve, $y_o = 6.00"$.

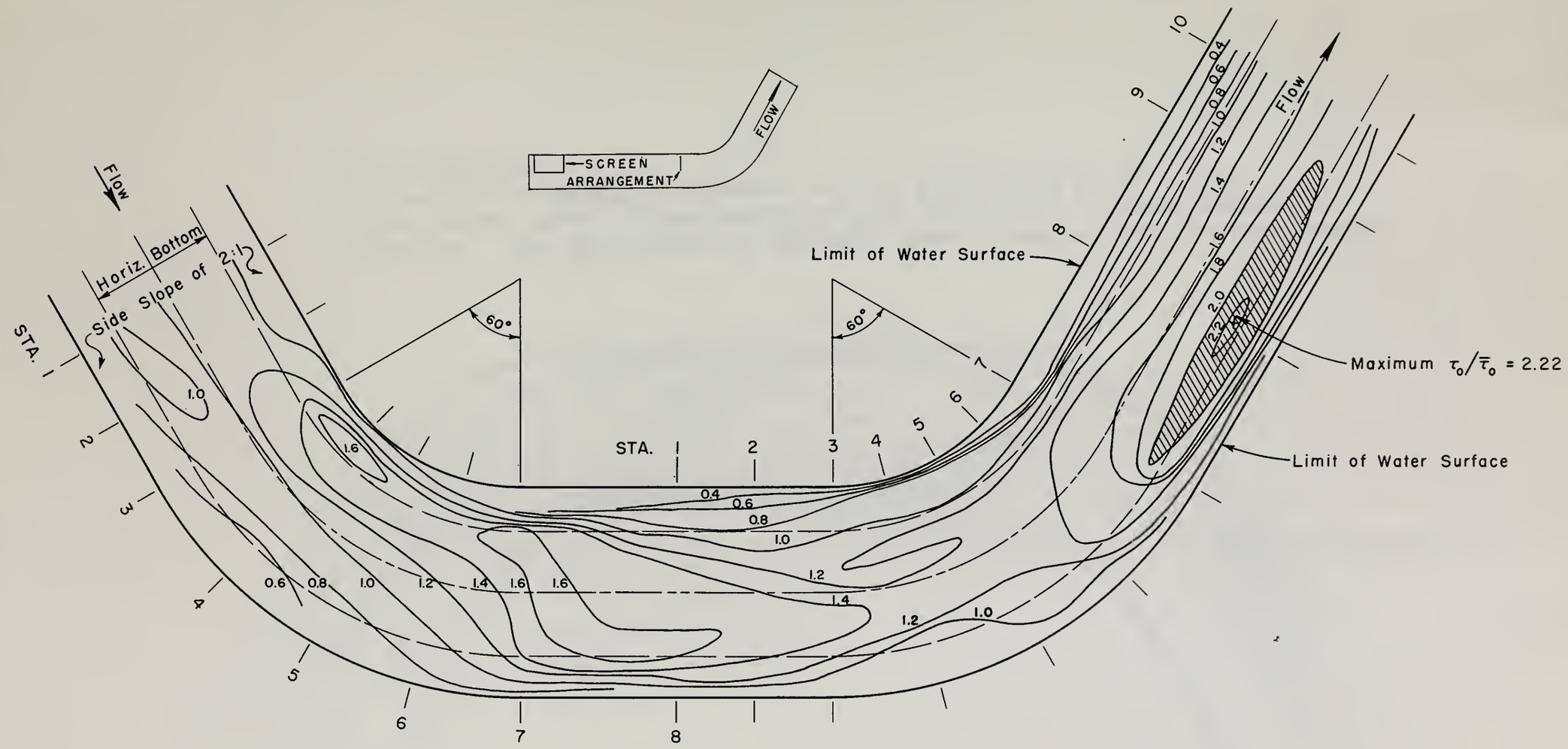


Figure 28. The Distribution of Boundary Shear Stresses in a Simulated Double Curve System, Shown by Contours of $\tau_o/\overline{\tau_o}$; Run No. 10: smooth channel, $b/r_c$ = 0.42, non-uniform approach, $w/y_o$ = 10, $w/r_c$ = 0.67, $y_o$ = 3.86", $\overline{\tau_o}$ = 0.0081 psf.

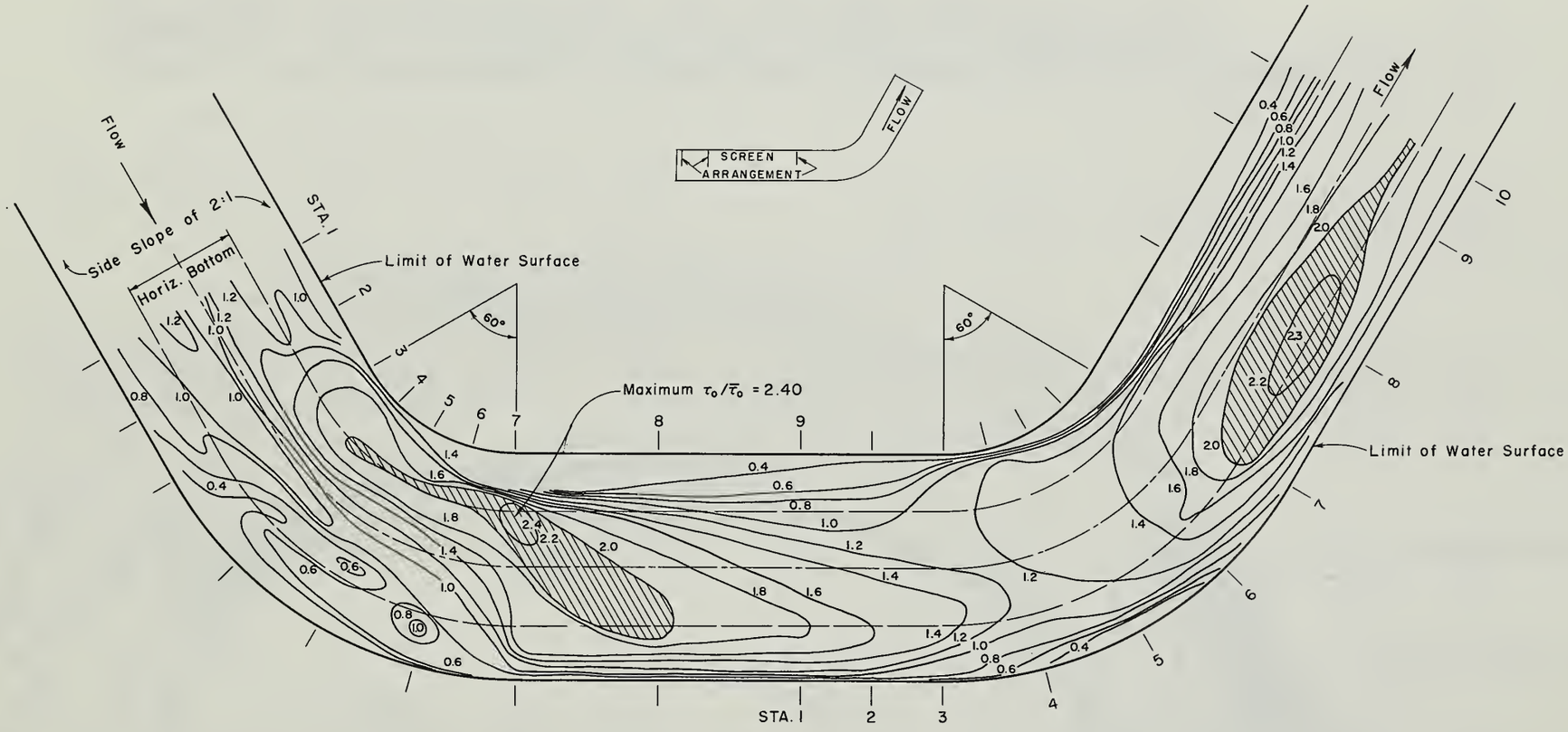


Figure 29. The Distribution of Boundary Shear Stresses in a Simulated Double Curve System, Shown by Contours of $\tau_o/\overline{\tau_o}$; Run No. 11: smooth channel, $b/r_c$ = 0.42, non-uniform approach, $w/y_o$ = 8, $w/r_c$ = 0.8, $y_o$ = 6.00", $\overline{\tau_o}$ = 0.0123 psf.

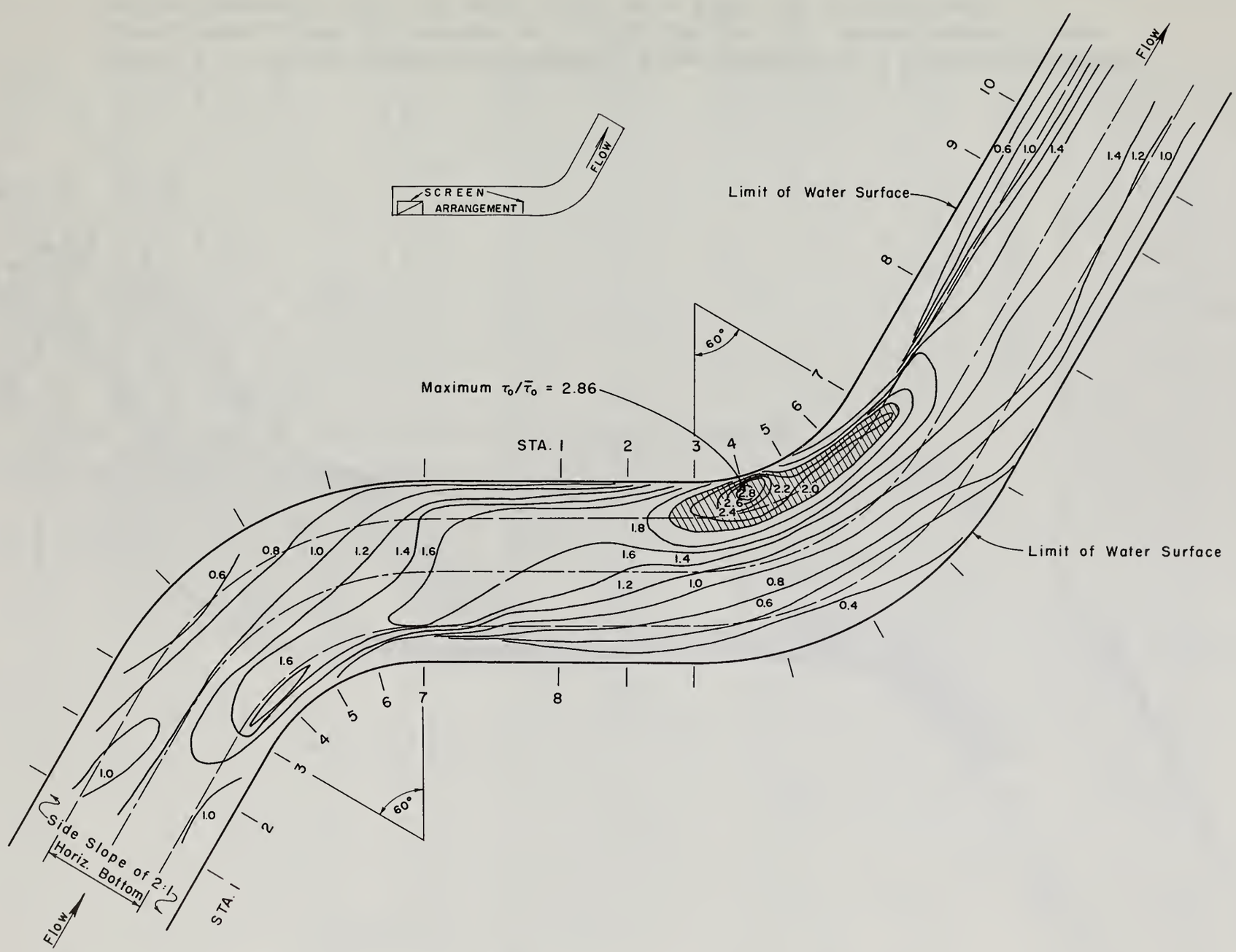


Figure 30. The Distribution of Boundary Shear Stresses in a Simulated Reverse Curve System, Shown by Contours of $\tau_o/\bar{\tau}_o$; Run No. 12: smooth channel, $b/r_c$ = 0.42, non-uniform approach, $w/y_o$ = 10, $w/r_c$ = 0.67, $y_o$ = 3.86", $\bar{\tau}_o$ = 0.0081 psf.

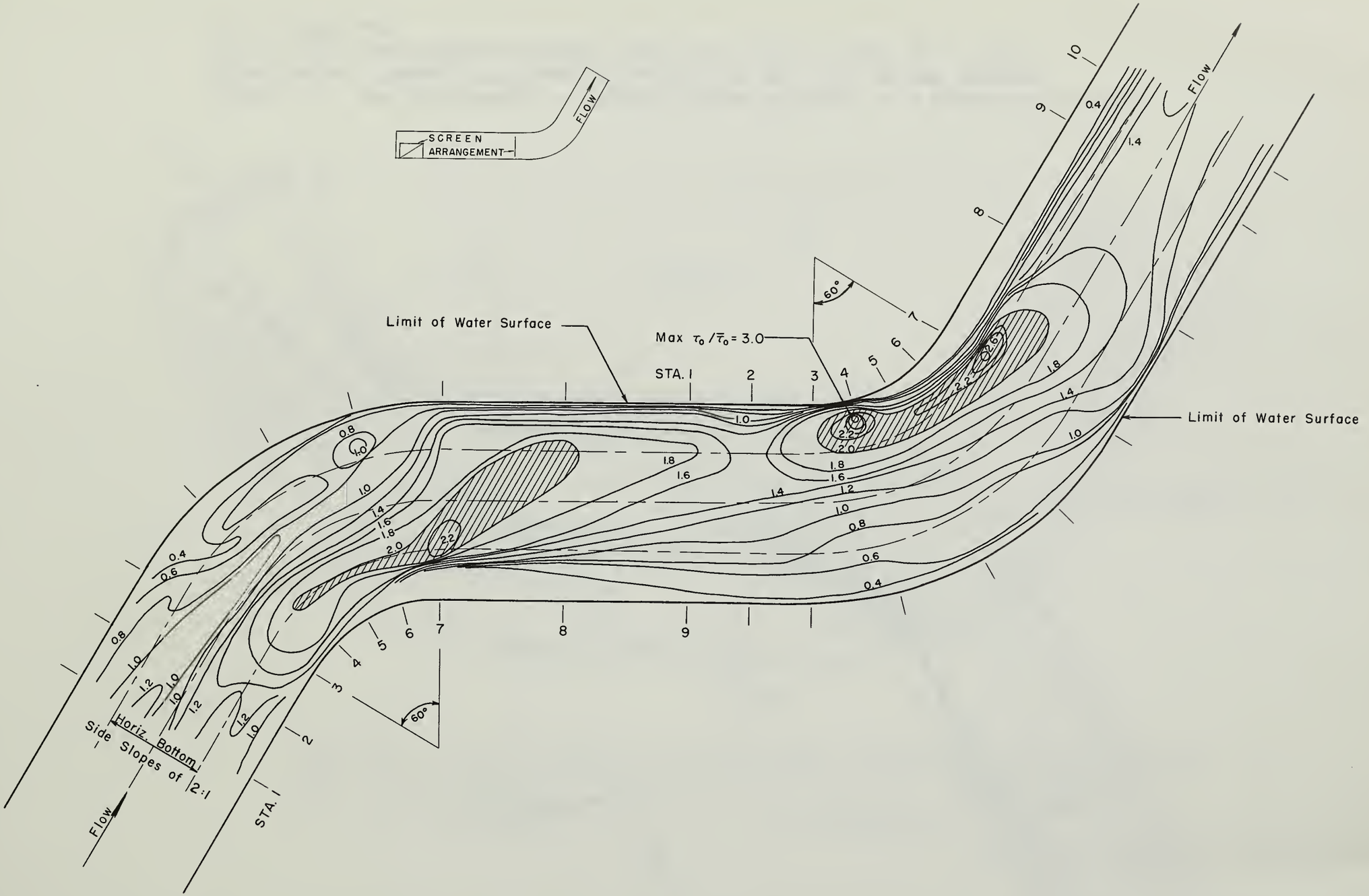


Figure 31. The Distribution of Boundary Shear Stresses in a Simulated Reverse Curve System, Shown by Contours of $\tau_o / \overline{\tau_o}$; Run No. 13: smooth channel, non-uniform approach, $w/y_o = 8$, $w/r_c = 0.8$, $y_o = 6.00"$ $\overline{\tau_o} = 0.0123$ psf.

The superelevations measured and computed for Runs 2, 10, 12 and Runs 4-A, 11, 13 may be compared in Table IIIa, b.

Because the velocity distribution in the single curve tests was shown to be related to the mapped shear pattern, the detailed velocity profiles are not given for the compound curve tests. Parts b and d of Figures 22-25 show the velocity profiles taken at Stations 1 and 8 in the four tests. Further discussion of the velocity distribution is given in relation to the shear stress patterns.

3. Boundary Shear Stress

Before proceeding with a discussion of the shear stress distributions determined in these tests, it is necessary to explain the shear maps shown in Figures 28-31. Consider the map of the 4-inch double-bend test, Figure 28; the right-hand half of the figure represents that portion of the channel which was actually mapped for the entrance conditions of velocity and shear shown in b and e of Figure 22. In the left half of Figure 28, the shear data for the single curve 4-inch test, Figure 22, have been reproduced. The two maps were joined by sketching the contours together to provide the shear distribution throughout the double bend shown in Figure 28.

For the 4-inch reverse-bend test, Figure 30, the right-hand section was mapped for the entrance conditions shown in b and e of Figure 24; the pattern from Figure 12 was reproduced in reverse to show the upstream curve. The maps of the 6-inch double and reverse-bend tests were prepared in exactly the same way, with the upstream curve pattern being obtained from Figure 14. The boundary shears were mapped for the entrance conditions shown in Sections b and e of Figures 23 and 25.

Examination of Figures 28-31 reveals the striking similarity between the shear patterns of the 4-inch and 6-inch tests for both the double and reverse-bend series.

In the double-bend tests, the deflection of the high velocities to the outside of the sequent bend prevents any degree of attack on the inner bank. In the downstream reach, comparison of the contours of $\tau_o / \overline{\tau_o} = 1.8$ shows that the shears are somewhat lower in Run 10 than in Run 11, although the difference is slight. The diminution of the outer bank shears within the sequent curve indicates a tendency for the flow to revert to the irrotational pattern of the single curve tests; however, the momentum stays high on the outside and leads to sharply rising shear stresses on the outer bank, below the curve.

Figures 30 and 31 reveal that, in the reverse-bend tests, high shear -- higher, in fact, than any measured in previous tests -- are confined to the convex bank. This high shear intensity occurs high up on the bank, throughout the curve, and the crossover pattern seen in

the cerlier tests never develops. The deflection of the high velocities in the approach section to the inner bank reinforces the natural tendency towards free vortex flow. The momentum of the fluid along the inner bank is sufficient to prevent separation. In the absence of the high velocity shift to the outside, the high momentum diffuses rapidly through the stream, and the shears return to normal, with a symmetrical distribution resulting again in a short distance.

The great similarity of the two shear patterns, in the double and reverse-bend tests, might best be explained by the turbulent structure of the flow in the various tests. For the single bend series, the flow enters the channel through a smooth transition from a reservoir in which there is essentially no turbulence. Thus, at Station 1, all of the stream turbulence is that which is generated in the boundary layer. With the introduction of upstream screens, however, free stream decaying turbulence is introduced into the flow at the point of disturbance. Since the variation in Reynolds number between the 4-inch and 6-inch screen conditions is small, it is to be expected that the turbulence intensities should be comparable. If the free stream turbulence were of sufficient intensity to overshadow the normal boundary effects, then the relative shear patterns would be quite similar, as indeed was the case.

In each of Figures 22-25, it will be noticed that sections c and d are more closely related to each other than they are to section a. The implication to be drawn from this is that, as might be expected, the effects of flow disturbances are not compounded indefinitely through curves.

Within the limitations of the simulative approach used in these tests, certain conclusions can be drawn. In the sequent part of a double-bend, the shear stresses are highest along the outer bank and do not vary greatly over those in a single curve. In a series of closely spaced reverse curves, the shears along the inner bank may be greatly increased. It is probably safe to infer that a tight S-pattern, such as that in Runs 12 and 13, would not normally be found in natural streams; the high shears on the sequent convex bank indicate that this configuration would tend to straighten itself rapidly.

## C. Superelevation in the Channel Bend

As shown in the earlier discussions, the major non-ideal aspects of the flow through a curve -- i.e. helicoidal motion and separation -- are intimately related to the varied pressure gradients induced by the water surface configuration. It is of interest, therefore, to compare the measured superelevations with those predicted on the basis of various assumed conditions of flow.

As a first approximation the superelevations may be computed from one-dimensional analysis. Assuming concentric flow at a constant uniform velocity, such that the momentum of the stream acts at the mean (centerline) radius of the curve, the superelevation is given by,

$$\Delta y = \int_{r_i}^{r_o} \frac{u^2}{gr}\, dr = \frac{V^2}{2g}\,\frac{2w}{r_c}\,, \qquad (11a)$$

where the subscripts, i and o, refer to the inner and outer radii of the bend, respectively.

A more accurate estimate of superelevation should be obtained by introduction of the appropriate velocity distribution function, $u = u(r)$, and integration of the resulting surface gradient over the width of the stream. As is shown in the Appendix, Section VIII, exact solutions for $\Delta y$ are possible corresponding to the various forms assumed for the function, $u(r)$. However, because of the change in mean depth which must occur within the curve (see Appendix) these solutions are cumbersome and not practical for direct application. In the channel tests, which were conducted for a moderate range of curvatures, it was found that the variation in measured mean depth was slight throughout the test reach. The assumption of constant mean depth greatly simplifies the expressions for superelevation, and in the following therefore, it is assumed that the mean depth and hence mean velocity are constant over the length of the test reach. The comparison of the resulting simplified equations for $\Delta y$ to the general expressions is given in the Appendix discussion.

In these developments a rectangular channel has also been assumed in order to permit a simple definition of bend geometry. However, for a trapezoidal stream of equal width and mean velocity, the superelevation, $\Delta y$, should be somewhat smaller due to the increase in effective mean radius as the flow moves outward on the sloping banks. In addition, for a real fluid, frictional retardation of the flow near the banks will further tend to reduce the total transverse water slope.

Since the gross features of the flow through the single curve indicate an essentially irrotational behavior, a better approximation of the superelevation should be attainable by treating the flow as a free vortex. For this condition $ur$ = constant and the total head is uniform

and constant at all sections. By again equating the radial pressure gradient to the centripetal acceleration, and integrating over the width of the stream, the superelevation, in terms of a proportionality constant, is given by,

$$\Delta y = \frac{K_1^2}{2g}\left(\frac{1}{r_i^2} - \frac{1}{r_o^2}\right) ; \quad K_1 = ur .$$

Then, for uniform specific head, and by the assumption of constant mean depth, the cross-sectional area is given by,

$$A = y_o w = \bar{y}(r_o - r_i) = \int_{r_i}^{r_o} y(r)dr = \int_{r_i}^{r_o} \left(H_o - \frac{K_1^2}{2gr^2}\right)dr .$$

This reduces to,

$$\bar{y} = y_o = H_o - \frac{K_1^2}{2gr_o r_i} = H_o - \frac{V^2}{2g} .$$

Solving for $K_1$ and substituting into the original expression for $\Delta y$, the superelevation in the free vortex becomes,

$$\Delta y = \frac{V^2}{2g}\,\frac{2w}{r_c}\left(\frac{1}{1 - \frac{w^2}{4r_c^2}}\right) \qquad (11b)$$

where

$$r_o - r_i = w$$

and

$$r_o + r_i = 2r_c .$$

In natural streams the flow in curves will show various degrees of asymmetry, depending on the entrance conditions, the bend curvature and the arc length of the curve. In long stream bends, as simulated in the channel tests by Runs 10 and 11, the patterns of flow ultimately established within the curve shows a radial increase in velocity. It is also of interest, therefore, to consider the superelevation produced in a curve with the highest velocities occurring near the outer bank. Such a condition may be approximated by assuming the stream to undergo motion as a

forced vortex, for which the velocity increases linearly in the radial direction. For this case,

$$\Delta y = \frac{K_2}{2g}(r_o^2 - r_i^2) \; ; \quad K_2 = \frac{u}{r} \; .$$

Again assuming constant mean depth and constant average specific energy (although the local specific hear, $H_o = y + u^2/2g$, is no longer constant), the coefficient $K_2$ may be solved from the expression for stream area, and the superelevation in the forced vortex simplified to,

$$\Delta y = \frac{V^2}{2g} \frac{2w}{r_c} \left( \frac{1}{1 + \frac{w^2}{12 r_c^2}} \right) \; . \qquad (11c)$$

Figure 32 shows a comparison of the maximum superelevations computed from Equations (11). It is of interest to note that, for the bends of moderate curvature normally found in natural streams, $w/r_c \approx 0.5\text{-}0.7$, the superelevation is virtually independent of the radial distribution of velocity. Thus, for a bend of given geometry the shape of the transverse surface profile will vary with the radial distribution of momentum; the total superelevation is a function only of the mean momentum of the stream.

For conditions approaching maximum curvature, $w/r_c = 2$, (i.e. $r_i = 0$), the computed superelevation for a free vortex becomes infinite. This is, of course, in accordance with the requirement of infinite velocity at the core of an irrotational vortex. In the motion of a real fluid, separation occurs under these conditions, imposing a finite limit on the actual magnitude of the superelevation.

The values of the superelevation computed for the complete test series from Equations (11) are listed in Table III for comparison with the measured values of $\Delta y$. Table IIIa shows the results for the full width of the trapezoidal section, while in Table IIIb only the central rectangular portion of the channel is treated.

Considering the practical limitations inherent in the exact measurement of water surface elevations, the agreement between the

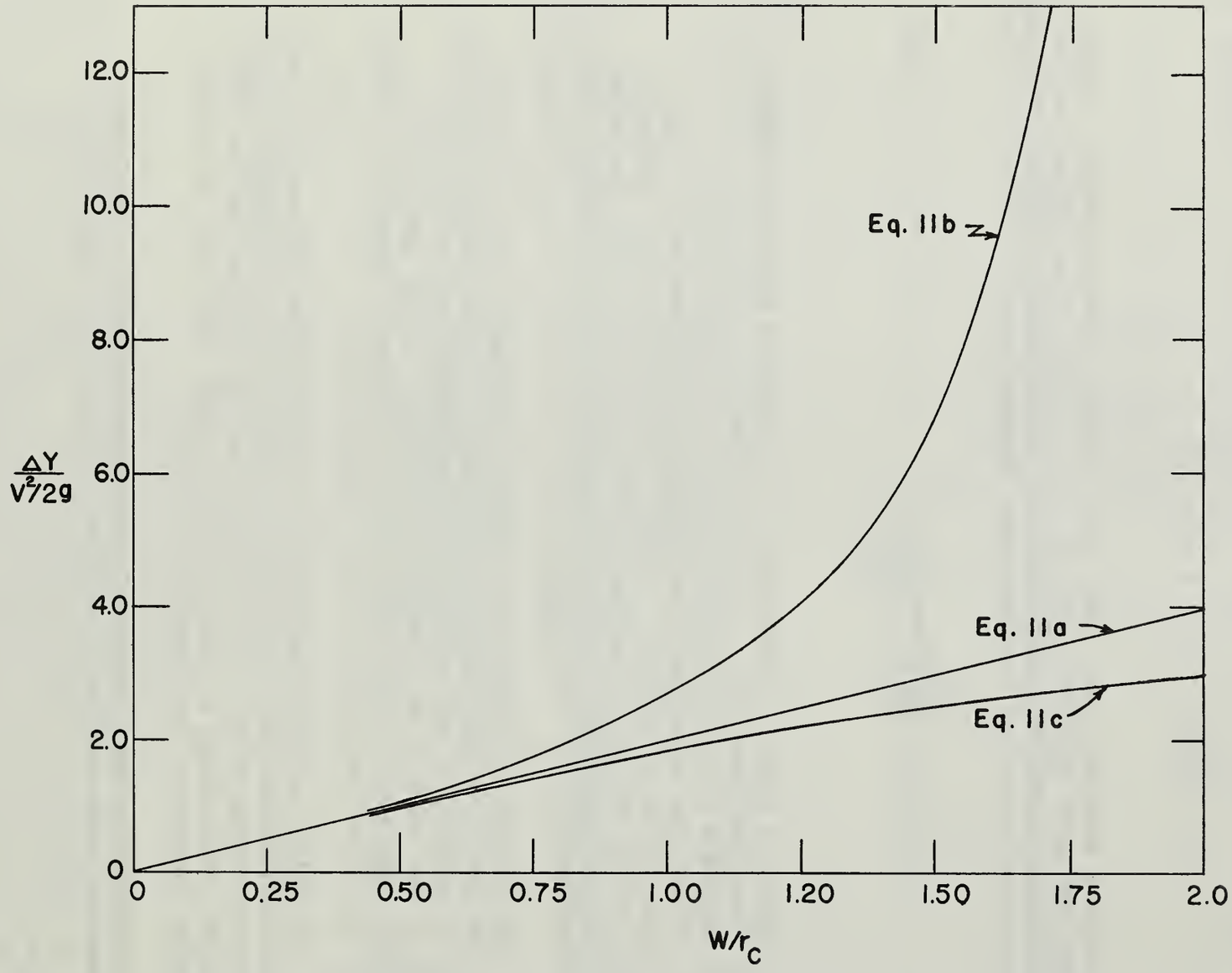


Figure 32. Variations in Total Water Surface Superelevation in a Circular Curve, as computed from one-dimensional analysis, and for the flow assumed as free and forced vortices.

TABLE III

Water Surface Superelevations Obtained from Measurements, One Dimensional Analysis and Vortex Theories.

$\Delta y$ given in inches.

| | a. Full Channel Width | | | | b. Rectangular Portion of Channel | | | |
|---|---|---|---|---|---|---|---|---|
| Run No. | Meas. at Sta 5 | One-Dimen. Eq. (11a) | Free Vortex Eq. (11b) | Forced Vortex Eq. (11c) | Meas. at Sta 5 | One-Dimen. Eq. (11a) | Free Vortex Eq. (11b) | Forced Vortex Eq. (11c) |
| 1 | 0.52 | 0.41 | 0.45 | 0.40 | 0.31 | 0.28 | 0.29 | 0.27 |
| 2 | 0.53 | 0.55 | 0.62 | 0.53 | 0.35 | 0.34 | 0.35 | 0.33 |
| 3 | 0.77 | 0.77 | 0.89 | 0.74 | 0.43 | 0.42 | 0.44 | 0.41 |
| 4A | -- | 1.09 | 1.30 | 1.04 | -- | 0.54 | 0.57 | 0.54 |
| 4B | 0.53 | 0.53 | 0.63 | 0.50 | 0.29 | 0.26 | 0.28 | 0.26 |
| 5 | 0.10 | 0.08 | 0.09 | 0.08 | 0.06 | 0.05 | 0.05 | 0.05 |
| 6 | 0.18 | 0.18 | 0.18 | 0.18 | 0.10 | 0.09 | 0.09 | 0.09 |
| 7 | 0.28 | 0.29 | 0.30 | 0.28 | 0.14 | 0.12 | 0.13 | 0.12 |
| 8 | 0.23 | 0.22 | 0.25 | 0.22 | 0.14 | 0.14 | 0.14 | 0.14 |
| 9 | 0.37 | 0.41 | 0.46 | 0.40 | 0.19 | 0.20 | 0.21 | 0.20 |
| 10 | 0.51 | 0.55 | 0.62 | 0.53 | 0.33 | 0.34 | 0.35 | 0.33 |
| 11 | 0.95 | 1.09 | 1.30 | 1.04 | 0.58 | 0.54 | 0.57 | 0.54 |
| 12 | 0.64 | 0.55 | 0.62 | 0.53 | 0.32 | 0.34 | 0.35 | 0.33 |
| 13 | 1.07 | 1.09 | 1.30 | 1.04 | 0.59 | 0.54 | 0.57 | 0.54 |

measured and computed results is good for the full trapezoid, as well as for the rectangular section. In the earlier report on this study (19), it was stated that the values measured over the full channel width were too low. Those figures were based on the measurements made closest to the edges of the stream. In the present compilation, shown in Table IIIa, the measured profiles were extrapolated to the stream boundaries, and the superelevations so estimated used as the values for the full stream width. There is no real evidence of the expected reduction in $\Delta y$, due to the effects of the sloping sides, noted above.

Run 1 (Table IIIa) shows the largest deviation from the predicted superelevation. It is likely that in this case wave disturbances emanating from the boundary influenced the measured value of $\Delta y$. The possibility of such error exists for all measurements near the edges of the stream; the size and magnitude of the error will depend on the distribution of the disturbances with respect to location of the measurements.

For conditions of least curvature the measured superelevation conforms closely to all of the predicted values. At increased curvatures, in the single curve tests, the full-width superelevation predicted for a free vortex is consistently too high, while the one-dimensional and forced vortex equations provide reasonably good estimates. The flow adjacent to the inner bank is retarded by boundary drag and here the irrotational pattern breaks down. It will be noted that for the single curve tests, the superelevation within the rectangular section is, in general, best represented by the free vortex formulation.

In the compound curve tests, Runs 10-13, the superelevations show, as expected, little effect of variations in the velocity distribution. It appears that such differences as do occur conform generally to the predicted trend. The double curves (Runs 10 and 11) with high velocities on the outer bank resemble the forced vortex. In the reverse curves, the higher velocities on the inner bank reinforce the natural tendency towards irrotational motion, and somewhat greater superelevation results.

It may be concluded that for streams of moderate curvature the water surface superelevation is quite insensitive to variation in the radial distribution of velocities. In practice an adequate estimate may be obtained through the simple one-dimensional treatment of the flow, Equation (11a).

## D. Energy Dissipation in a Channel Bend

In order to relate the present work to previous studies of energy losses in bends, the measured shear distributions may be applied to a one-dimensional analysis of the energy dissipation in the curved reach of the open channel. In the following discussion only the smooth channel tests for a single curve, Runs 1-7, are considered.

As noted earlier, the short exit tangent made it impossible to study the return of the flow below the curve to uniform conditions. For this reason the results presented herein will not bear direct quantitative comparison to tests performed in channels of adequate length. However, the detailed information on the shear stresses in these tests contributes to the understanding of the modes of local dissipation as related to the overall losses in a bend.

The energy of a flowing stream is dissipated through the resistance or drag upon the solid boundaries. If a control volume is assumed of cross section $A_x$, of perimeter $P_x$, and of length $\Delta x$, the power dissipated becomes:

$$\Delta HP = \tau_x P_x \frac{Q}{A_x} \Delta x = \tau_x P_x V_x \Delta x , \qquad (12)$$

wherein $\tau_x$ is the mean shear stress over the perimeter $P_x$.

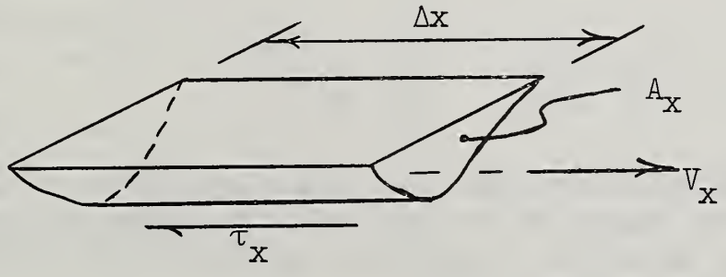


The energy dissipated per pound of fluid flowing per unit length of channel becomes:

$$\left.\frac{\Delta H}{\Delta x}\right|_x = S_{e_x} = \frac{\tau_x P_x V_x}{\gamma A_x V_x} = \frac{\tau_x}{\gamma R_x} . \qquad (13a)$$

For uniform or normal flow in straight channels the quantities involved become independent of distance. For flow through curves and other channel transitions, variations in these quantities must be expected with distance in accordance with the non-uniform character of the flow.

Since the dimensions of the test-channel for the experiments on channel curves did not permit the establishment of completely uniform flow, the conditions at Station 1 were adopted for reference purposes. In order to avoid confusion with hydraulic properties for uniform flow, which are usually denoted by the subscript, o, the coordinate, x, is here re-defined such that at Station 1, $\tau_x = \tau_1 = \overline{\tau_o}$.

Equation (13a) may be transformed by introducing a mean friction coefficient,

$$\tau_x = C_{f_x} \rho \frac{V_x^2}{2} \; ;$$

$$S_{e_x} = \frac{\Delta H}{\Delta x}_x = \frac{\tau_x}{\gamma R_x} = C_{f_x} \frac{V_x^2}{2gR_x} \; . \qquad (13b)$$

In these tests, it was found that the maximum increase in $\tau_x$ is of the order of 40% while $A_x$, $P_x$, and $V_x$ vary only about 2-4%. From Equations (13) therefore, neglecting variations in flow geometry, the local average rate of energy dissipation is proportional to $\tau_x$. However, $\Delta H/\Delta x\big|_x$ is only approximately proportional to $C_{f_x}$ within the variations of $V_x^2/2g$.

In Figure 34 graphs are shown for two of the runs in which the rate of energy dissipation relative to that at Station 1 is plotted as,

$$\frac{\tau_x}{\tau_1} = \frac{S_{e_x}}{S_{e_1}} \; , \quad \text{vs.} \quad \frac{x}{r_c} \; ,$$

where $x$ = centerline distance through the test reach and $r_c$ = centerline radius of the bend. The values of average relative shear at each station, $\tau_x/\tau_1$, were obtained by graphical integration of the section plots of shear vs. perimeter shown in Figure 33;

$$\frac{\tau_x}{\tau_1} = \frac{\tau_x}{\overline{\tau_o}} = \left[\frac{1}{P}\int \left(\frac{\tau_o}{\overline{\tau_o}}\right) dP\right]_x \; . \qquad (14)$$

In the same figure, the variation in $C_f$ is plotted as $C_{f_x}/C_{f_1}$.

The foregoing relationships may be applied to give an approximation of the additional head loss for flow through the curve. By integration of the $\tau_x/\tau_1$ curves, the average relative shear stress, $\overline{\tau_L}/\tau_1$, may be determined over the test reach of length, L. These computations were performed for the test series, Runs 1-7. The average relative shears so obtained are presented in Table IV and Figure 35, which show the variation with relative curvature. From the proportionality shown in Equations (13) between $\tau_x$ and $S_{e_x}$,

$$\frac{\overline{S_{e_L}}}{S_{e_1}} = \frac{\overline{\tau_L}}{\tau_1} \; . \qquad (15)$$

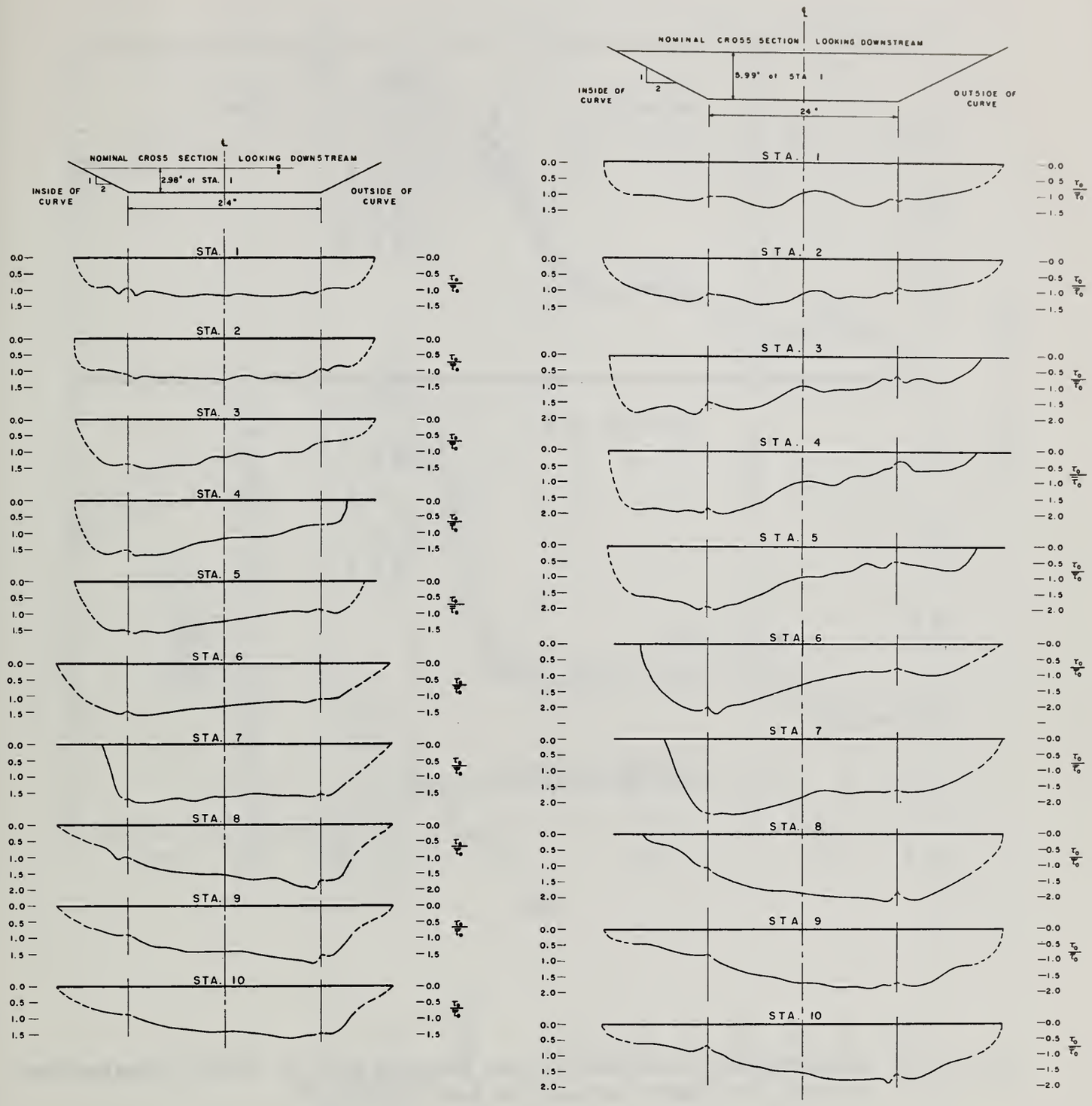


(a) Run No. 1

(b) Run No. 4-B

Figure 33. Shear Distribution by Section Showing Local Values of $\tau_o / \overline{\tau_o}$.

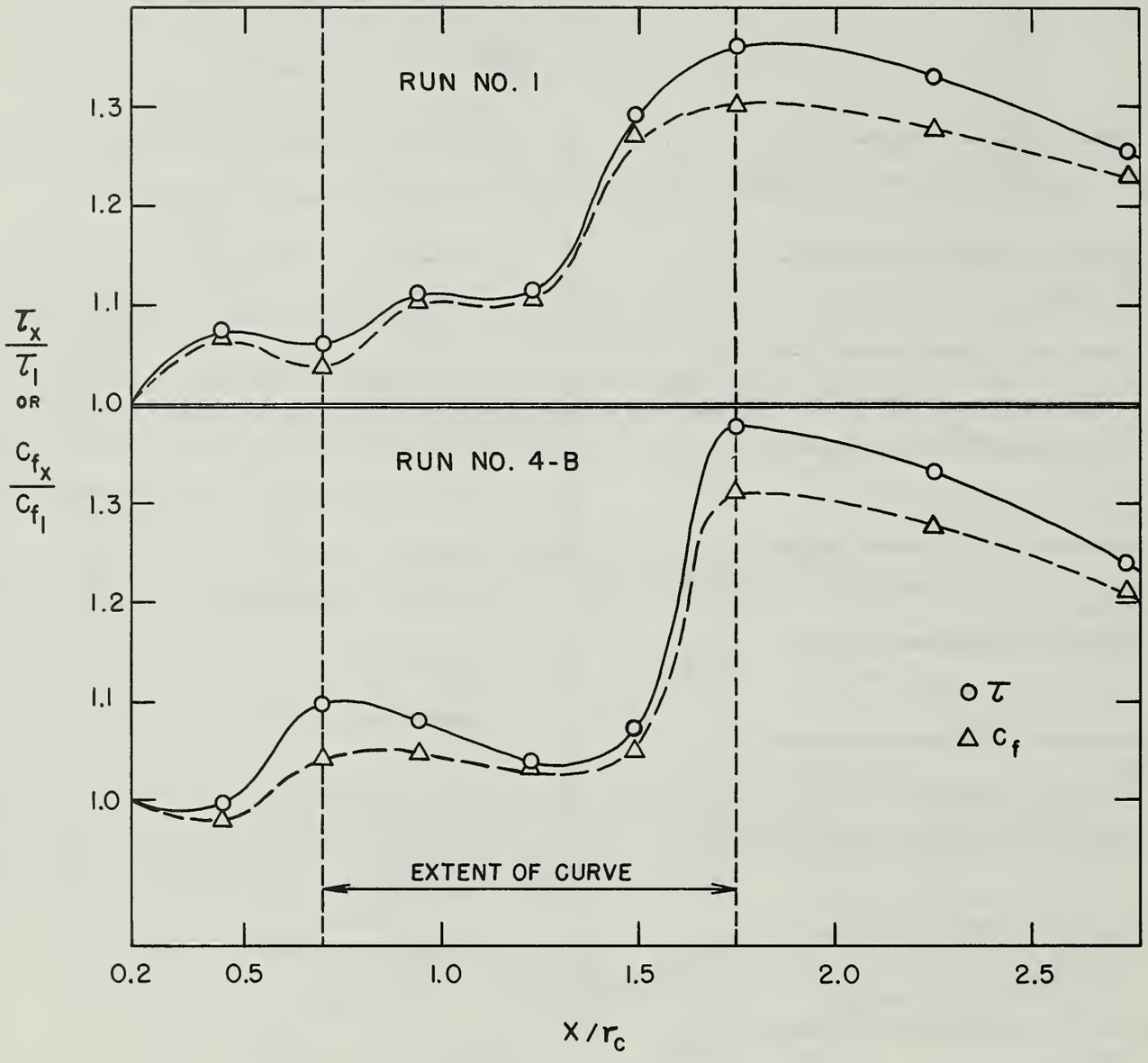


Figure 34. Longitudinal Variation in the Average Rate of Energy Dissipation Through the Curve, shown for Runs 1 and 4-B.

## TABLE IV

Energy Dissipation in the Test Reach

| Run No: | Average shear stress at Station 1: $\tau_1 = \overline{\tau_o}$, lb/ft² | Average relative Shear over the Test Reach: $\overline{\tau_L}/\tau_1$ | Fractional excess energy dissipation over the Test Reach: $\frac{\overline{S}_{e_L} - S_{e_1}}{S_{e_1}}$ | Maximum local relative shear measured within the Test Reach: $(\frac{\tau_o}{\overline{\tau_o}})_{max.}$ |
|---|---|---|---|---|
| 1 | 0.0070 | 1.20 | 0.20 | 2.00 |
| 2 | 0.0087 | 1.08 | 0.08 | 1.78 |
| 3 | 0.0101 | 1.14 | 0.14 | 2.20 |
| 4-B | 0.0060 | 1.16 | 0.16 | 2.40 |
| 5 | 0.0034 | 1.05 | 0.05 | 1.60 |
| 6 | 0.0055 | 1.02 | 0.02 | 1.60 |
| 7 | 0.0074 | 1.07 | 0.07 | 1.75 |

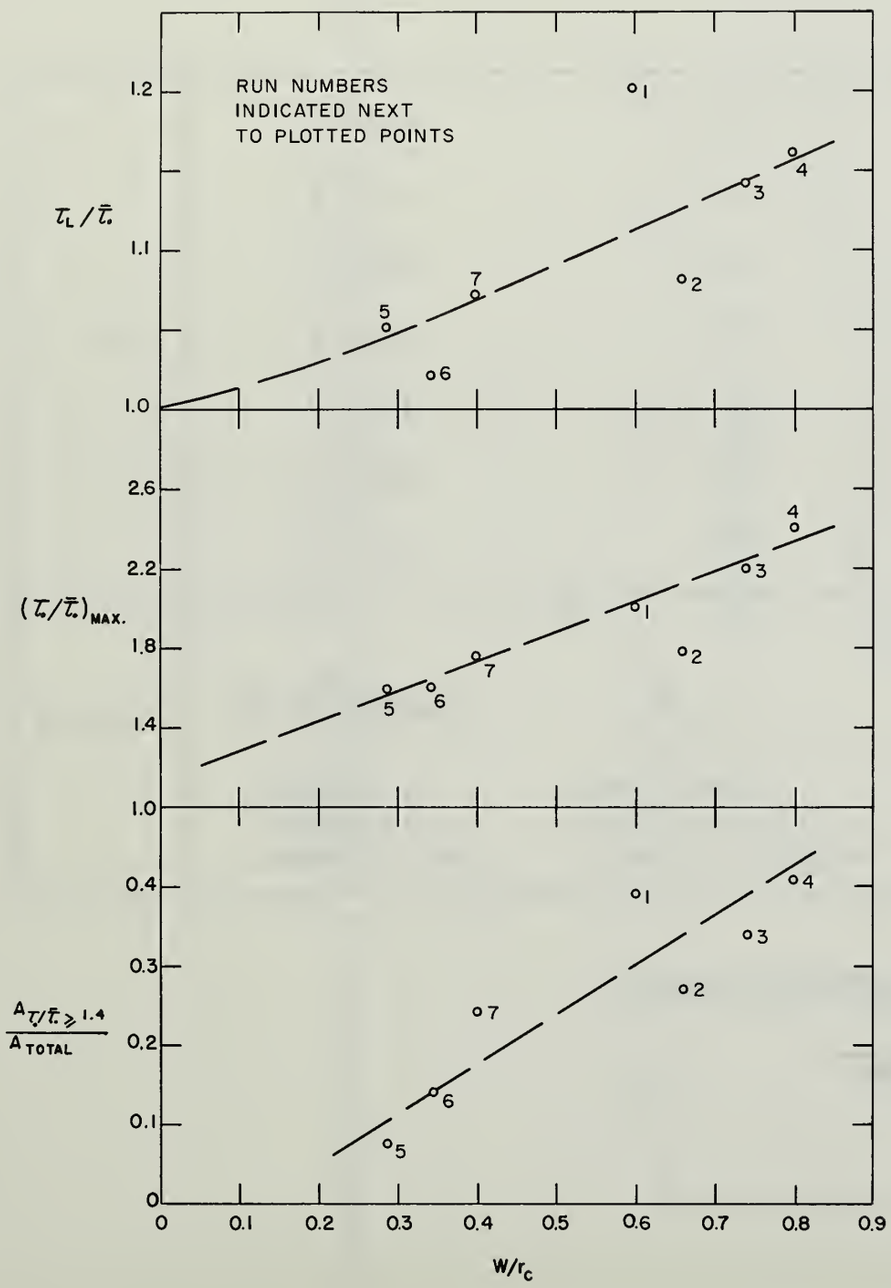


Figure 35. The variation with stream curvature of of the average rate of energy dissipation in the test reach, expressed as $\bar{\tau}_L/\tau_1 = \bar{\tau}_L/\bar{\tau}_o$.

Figure 36. The variation with stream curvature of the magnitude of the maximum relative shear stress measured in the test reach, $(\tau_o/\bar{\tau}_o)_{max.}$

Figure 37. The fraction of the test reach area affected by stresses of magnitude $\tau_o/\bar{\tau}_o > 1.4$.

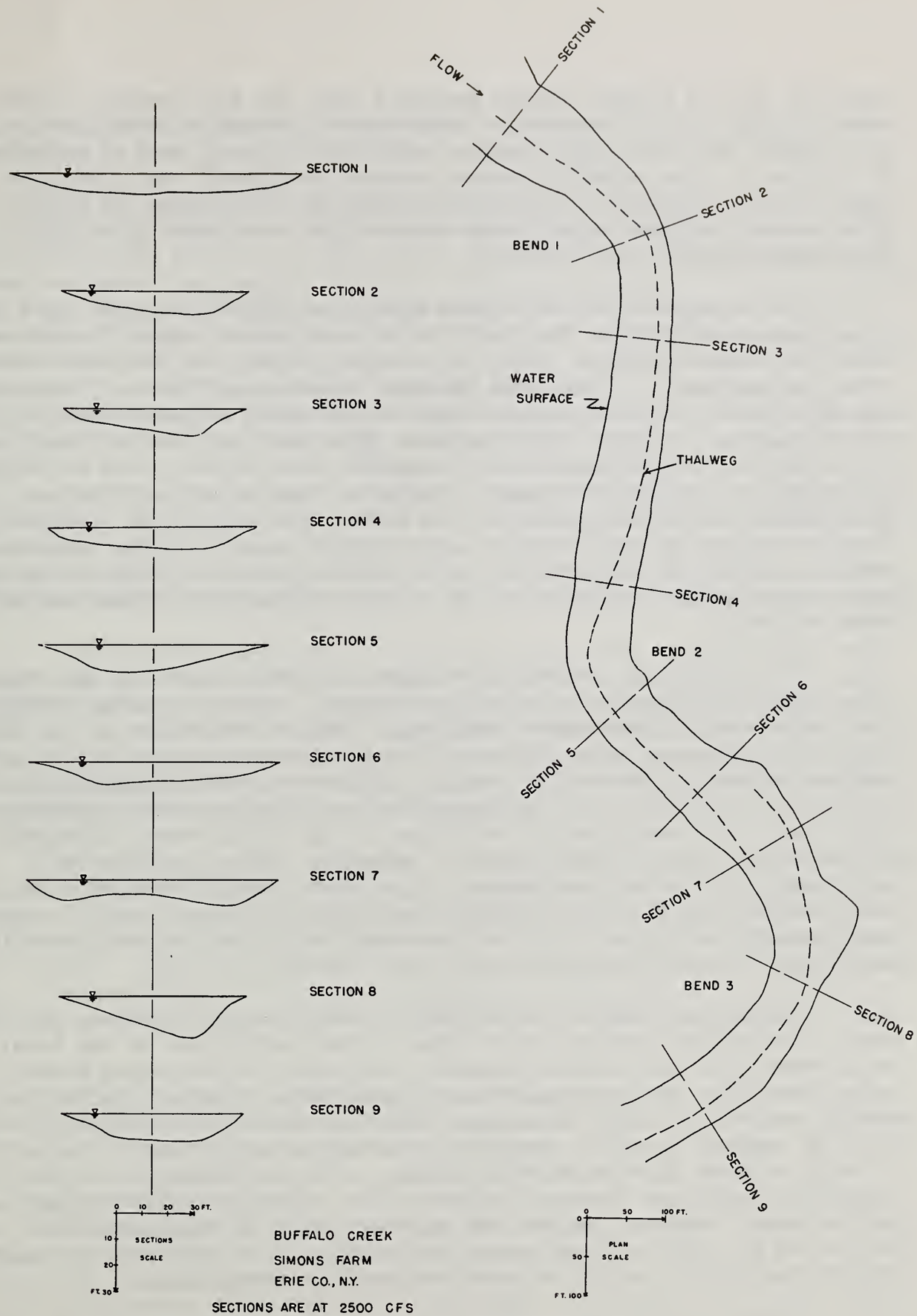


Figure 38. Sketch map and lateral sections of an alluvial stream, showing the course of the channel of maximum scour.

Since $\bar{S}_{e_L}$ is the average energy gradient over the test reach, the difference, $L(\bar{S}_{e_L} - S_{e_1})$, represents the average increase in head loss per unit length over the normal rate of head loss assumed here as existing at Station 1. The relative average excess head losses are shown for these tests in Table IV. Due to variation in the location of Station 10 in several of the tests, these computations are based on a test reach extending from Stations 1-9.

It is appreciated that this method as applied here can give only a very approximate value for the rate of energy loss caused by the curve, since the normal friction slope is probably higher than the one determined for Station 1. Also, the straight length downstream of the curve was not adequate to follow the return of the shear stresses back to normal values. However, other methods of determining the net head loss (e.g. the analysis of variation in specific head) are subject to the same difficulty of inadequate tangent lengths of channel and involve the measurement of surface gradients. With the flow conditions employed, these measurements could not be made accurate enough to give consistent results, and hence this approach of evaluating the head loss due to the curve was abandoned in favor of the direct application of the boundary shear stresses.

The effect of a curve is similar to that produced by any resistance which might exist in a straight channel, such as a sill, bridge pier, or a reach of increased roughness. Such a resistance to the flow will cause decreased velocities and increased depths, resulting in an upstream storage of potential energy. The excess energy dissipated in the curve is obtained from the backwater, or storage, reach upstream, where there is a compensating reduction in the total energy dissipated on the stream bed. At some distance below the curve, the flow will again return to normal conditions. Thus, for straight approach and exit reaches of sufficient length, there would be no net excess energy loss through the curve. This is a general rule which may be stated for any obstruction or resistance in an open channel.

Therefore, a major difficulty in determining the excess rate of energy dissipation due to a curve lies in the definition of the total reach over which the loss is measured. In order to make open channel tests comparable to investigations on pipe bends, the best definition should probably be based on a reach starting above the curve at the point of maximum specific energy and extending downstream to the point at which uniform flow is re-established. The exact location of the downstream point, as long as it lies in the region of uniform flow, is not critical. However, since the upstream point of measurement is determined by the backwater curve, it is clear that error in the location of this point will modify the measured results accordingly.

In the light of the above argument, it is to be expected that the boundary shear stress measured at Station 1 should be lower than the average shear stress, $\gamma RS_e$, computed for a uniform flow. The short length of the test channel makes it impossible to evaluate $\gamma RS_e$ accurately,

but, as shown in Table II, the measured values of $\overline{\tau_o}$ (at Station 1) are consistently lower than the estimated average shear stress, $\gamma RS_e$.

It is seen from Figure 34, in which $\tau_x/\tau_1$ is equivalent to the ratio, $S_{e_x}/S_{e_1}$, that the energy dissipation is only moderately increased in the upstream portion of the curve. Near the curve exit, however, the shear stresses rise sharply with the shift of momentum to the outer bank, and these high shears decrease only slowly towards the normal value in the channel section below the curve. In preparing the plots to determine $\overline{\tau_L}$ for the tests at lower curvature, Runs 5-7, it was found that within the early part of the curve the average shear, $\tau_x/\tau_1$, decreases to a value of about 0.92, before increasing towards the exit. The implication from this is that, for decreasing curvature, the storage reach may extend further into the bend. The resistance of the curve lies primarily in the zone in which the irrotational pattern breaks down. Thus, as long as the flow through the curve takes place without separation and is essentially in accordance with an irrotational pattern, average energy losses remain moderate within the curve itself. The greatest part of the loss occurs below the point of breakdown, over a reach extending well below the curve.

The relative amounts of the loss, which occur within the curve proper and over the downstream reach, vary with the geometry of the bend. Ito (21) has shown that, in pipe bends of large curvature, as much as 90 % of the bend head loss may take place in the downstream tangent. However, for moderate curvatures ($d/r_c \approx 0.2$), only about 40 % of the energy is dissipated in the sequent reach, due to the reduction in the disturbance generated by the curving boundary.

The general trend indicated in Figure 35 suggests an increase in excess dissipation with increasing curvature. Because of the small number of tests available for this comparison and the relatively large scatter of the points, no attempt was made to give concise formulation of this trend. Intuitively such a trend is quite plausible; at zero curvature, the resistance is that of a straight channel, $\overline{\tau_L}/\tau_1 = 1$, while at maximum curvature the resistance should attain a maximum (finite) value.

Previous investigations on losses through bends in pipes (2), as well as in open channels (26), have revealed that there may occur an anomaly in the rate increase of bend resistance with increasing curvature. For bends of constant roughness and deflection angle it appears that, with increasing curvature, there exists an intermediate condition of relative minimum resistance. The critical value of curvature at which this anomaly occurs has not been clearly defined, nor has its cause been adequately explained. It is recognized that the deviation of Runs 1 and 2 from the general trend of increasing resistance may be an indication of this phenomenon in the open channel tests. However, it is felt that, because of the small amount of available data, there is no justification in this case for assuming such a discontinuous behavior.

In concluding this discussion it can be stated that the mean loss coefficients determined for flow through curves from the usual hydraulic

measurements give an inadequate indication of the maximum intensities of local shear stresses. For flow through single curves, the maximum local shears were found to exceed the mean initial shears by over 100 %, while mean sectional shear stresses were only of the order of 35 % larger than the mean stresses at the entrance of the curve. For conditions of increasing curvature, there is an increasing trend in the mean sectional shears, as well as in the total relative resistance of the entire curved reach.

## E. Scour Patterns in Alluvial Streams

In the previous section the energy dissipated by a curving stream was discussed in terms of an average resistance over the total curved reach. While this approach is of interest in considering the role of boundary geometry in the overall energy balance of the stream, it tends to obscure the local conditions controlling the scour pattern. From a comparison of the shear maps with the mean values shown in Figures 34 and 35, it is clear that, in an erodible channel localized areas of scour should be expected at various sections for which the mean shear stress is not critically high.

For the understanding of scour patterns, therefore, it is probably more logical to consider the variation in magnitude of some parameter of local shear as a function of bend geometry. In Figure 36, the magnitude of the maximum measured shear stress for Runs 1-7 is plotted against relative curvature, $w/r_c$. Because of the statistical uncertainty of actually determining an extreme value in these tests, the quantitative validity of Figure 36 is subject to question. However, the trend is clear, and it may be concluded that, in an erodible trapezoidal channel, these would represent points at which erosion would first appear. As noted in the earlier discussions, with increasing curvature this point of initial scour moves to a position further upstream. On the basis of these tests, this shift is apparently quite abrupt, occurring at a curvature in the range $0.67 < w/r_c < 0.73$.

An additional parameter, which may also be relevant in an approach to the problem of channel stability and the design of revetments, is the variation in areal extent of a zone subjected to shears greater than some critical magnitude. Consider, for example, the zones in the curved reach (Runs 1-7) enclosed by the contour $\tau_o / \overline{\tau_o} = 1.4$. These areas, expressed as a fraction of the area of the test reach, are plotted in Figure 37. As might be expected, the relative area exposed to shears equal to or greater than a given value increases with increasing curvature. For channels of fixed boundary geometry (Runs 1-4, or 5-7), the increase in depth and curvature at flood conditions will lead to scour which is increased both in extent and intensity.

Before it becomes feasible to apply these experimental results directly to natural streams, further information is needed on the effects of boundary deformation on the pattern of scour. It is evident that, at

a point of high local shear stress, scour will occur. It cannot be predicted, however, to what degree the resulting boundary depression will modify the shear either at the point or in the surrounding area. In addition, the deposition which may be expected in the zones of reduced shear should further modify the flow pattern by localized aggradation of the boundary.

The variation in erodibility of sorted sediments adds still another complicating factor to this problem. Sundborg (43) has shown that the sorting of a heterogeneous bottom sediment depends on the size range as well as on the particle shapes and the nature of the sediment mixture. In some sediments, the fine material is winnowed out, leaving an erosion pavement which can withstand much higher shears. Under other conditions the residual sediment is comprised of the finer material, which may then develop into ripples and thus alter the effective bottom roughness. Valuable information could be gained from both laboratory and field work in which systematic studies were made to determine the sorting of bottom sediments under varied shear stresses. Of particular interest to the present study would be data on the size distribution across transverse sections in stream bends. As far as could be determined, this work has never been done.

In spite of these still unsolved problems, a quite logical relationship can be observed between the scour patterns in alluvial streams and the boundary shear distributions measured in the channel experiments. Figure 38* shows a short reach of Buffalo Creek, Erie County, New York, in an area where the stream flows through an unconsolidated mixture of glacial sands and silty clays. The stream discharge of 2,500 cfs to which the map corresponds is based on the approximate conditions of annual spring flooding.

By comparison of the section profiles with the map, the scour pattern through the reach can be observed. Before each bend the stream assumes an approximately trapezoidal shape, indicating a symmetrical flow distribution. The tendency for the flow to cross to the outer bank under the influence of the helicoidal motion extends quite far upstream in each bend, as evidenced by the early dislocation of the thalweg. Between the second and third bends, an oblique bar is evident at the crossing point, with a discontinuity of the thalweg. This is a type of bar configuration which is common to many sinuous streams. The scour extending down to the inner bank of Bend 3 is due to the tendency to irrotational motion of the flow entering the curve, as well as to the asymmetry of the flow leaving Bend 2. A similar condition may be observed for the reverse curve tests in the channel, Figures 30, 31. In these bends of moderate curvature, the helicoidal motion should be developed early in the curve, and the deeper channel on the concave bank is thus extended quite far upstream.

In closing the discussions of these experiments it may be remarked

*This material was supplied by Messrs. D. A. Parsons and R. P. Apmann, of the Agricultural Research Service.

that the magnitudes of the measured shears, which might be expected to cause bank instability, compare favorably to field observations on erosion in curves. Lane (22) set forth stability criteria based on tractive force studies conducted in unlined channels. For canals ranging in curvature from straight to very sinuous, the stability criterion is given as a fractional reduction in the permissible tractive force. It is stated that, for very sinuous canals, the permissible tractive force (equivalent to $\overline{\tau_o}$) is reduced by a factor of 0.6. Thus, the maximum relative tractive force to be expected in such curves is $\tau_o / \overline{\tau_o} = 1/0.6 = 1.7$.

The degree of curvature as defined by "very sinuous" corresponds to the areal configuration "typical of canals in foothills or mountainous topography" [(22), p.1257]. A reasonable estimate of curvatures for such streams appears to be of the order of $0.4 < w/r_c < 06$. While the maximum shears measured in the channel are somewhat greater than this, the agreement is quite good.

It may be concluded that the local tractive forces measured under these simplified channel conditions do provide a useful indication of the distribution and intensity of erosive attack on the boundaries of alluvial channels. In order to establish closer correlation between the laboratory and field conditions, further effort should be directed towards two major areas: (1) observation techniques leading to more concise quantification of field data and (2) the interaction between flowing water and the stream sediments. The latter problem includes the role of entrained sediment as it modifies the dynamical properties of the transporting fluid, as well as the effect of boundary alteration arising from movement of the bed material.

## VI. CONCLUSIONS

The results of this investigation of flow through curved trapezoidal channels permit a number of important conclusions.

### A. Flow Through Single Curves

1. For channels composed of a single 60-degree curve with straight approach and exit tangents, the flow pattern within the curve tends to conform to that of a free vortex. Boundary layer effects, combined with the centripetal acceleration in the curving flow, cause a trend to separation along the concave bank near the curve entrance and a more pronounced separation zone originating at the convex bank towards the exit of the curve. In addition to separation, the frictional effects produce the expected helicoidal motion.

2. The two frictional aspects of the flow, separation and the secondary, helicoidal current, tend to produce a breakdown in the irrotational type of motion, with the ultimate establishment of high velocities along the concave bank. The section of the curve at which the stream momentum is transferred from the inner to the outer bank varies with the bend geometry. This crossover point occurs earlier in the curve for streams of decreasing curvature. Under conditions of greatest curvature, the irrotational type of pattern prevails throughout the curve itself; and at the exit section the crossover is abrupt, due to the large separation zone on the inner bank.

3. The distribution and the magnitudes of the boundary shear stresses produced by the curved flow cannot at present be predicted quantitatively, either by theory or by correlation with measured velocity distributions. In general, the locations of the shear maxima were found to be associated with the course of the filament of highest velocity and with the zones of locally accelerated motion. Thus, high stresses are found along the inner part of the curve and near the outer bank below the curve exit, with a strongly asymmetrical shear distribution persisting for a considerable distance in the downstream tangent reach.

4. The location and the relative intensity of the maximum local shear stress in a curve are controlled primarily by the stream geometry. For streams of increasing curvature, the relative magnitude of the shear maximum increases, and it tends to occur earlier in the curved reach. For the range of curvatures studied in the smooth channels, $0.29 < w/r_c < 0.8$, the shear maximum increased from $\tau_o / \overline{\tau_o} = 1.6$ to 2.4.

5. The total head loss for the curve, as well as the average rates of loss at sections throughout the curved reach, may be computed from the measured shear distributions. This one-dimensional treatment of the flow gives inadequate indication of either the intensities or the peripheral locations of the highest shears; however, it demonstrates

that the excess stream energy dissipated due to a curve increases with increasing curvature.

6. The introduction of boundary roughness does not appear to modify the shear pattern within the curve itself. However, in the downstream reach below the crossover point, the shears are substantially higher, due to the greater development of the helicoidal motion over the rough boundary.

## B. Compound Curve Systems

1. The technique of simulating the effects of upstream curvature by artificially reproducing the related velocity distributions in the approach channel has proved to be useful and economical for establishing shear patterns for compound curves. The quantitative validity of this method remains subject to detailed confirmation.

2. The effect of a reversed curvature is simulated with high velocities near the inside bank at the entrance section. This condition reinforces the free vortex pattern, increasing the superelevation to a slight degree. High shear stresses are produced along the inner bank. Separation towards the exit section is prevented, and thus a more symmetrical flow condition exists in the downstream tangent with shear stresses much reduced, as compared to the case of the single curve.

3. With high velocities produced near the outside bank at the entrance section a double curve configuration is simulated with a short straight section between the curves. This approach condition suppresses the free vortex pattern in the curve; a larger separation zone is formed near the inside bank; and higher shear stresses are encountered along the outer bank throughout the test reach than for the single curve.

4. In general, it may be concluded that longer curves will not materially increase maximum shear intensities; by contrast, reversal of curvature in compound systems leads to a substantial increase in local shear intensity. The absolute maximum relative shear stress was observed to be 3.0 in the simulated reverse curve.

## C. General Observations

1. For stream bends of moderate curvature, the superelevation of the water surface is quite insensitive to variation in the radial distribution of velocities and may be predicted adequately by a one-dimensional treatment of the flow. The total superelevation appears to be a function only of the mean momentum of the stream and the relative curvature of the bend.

2. For a given channel alignment, the relative shear patterns in a curve are in general not greatly modified by variations in depth and

velocity at the curve entrance, but seem to depend primarily on the boundary geometry. For the range of flow conditions which can occur in a trapezoidal channel, the intensities and the areal extent of the highest shears increase with increasing depth and curvature.

3. This study has demonstrated the importance of boundary shear stress patterns with respect to the ultimate understanding of erosion and deposition processes in channel curves. It has been shown that the trends in the measured shear distributions conform quite closely to the scour patterns observed in sinuous alluvial streams, and that, insofar as the limited field data permit a comparison, the magnitudes of the measured stresses suggest agreement with the intensity of the channel scour.

4. While the orientation of the shear stresses was neglected in this study and is not believed to affect the stated results, it may be concluded that it assumes considerable importance with respect to bank slope stability in channels through uniform non-cohesive materials.

5. The distribution of the shear stresses over the boundary is conveniently determined from surface Pitot tube measurements. This technique as previously developed by Preston for air flows has been successfully adapted to the present problem for smooth as well as rough boundary surfaces.

## VII. BIBLIOGRAPHY


1. Abarbanel, S.S., Hakkinen, R.J., and Trilling, L., Use of a Stanton Tube for Skin friction Measurements. NASA Memo 2-17-59W, 1959.

2. Anderson, A.G., Fluid Flow Diversion; A Summary and Bibliography of Literature. Univ. of Minnesota, St. Anthony Falls Hydraulics Laboratory Project Report No. 1, 1947.

3. Bagnold, R.A., The Flow of Cohesionless Grains in Fluids. Phil. Trans. Roy. Soc. A, London, No. 964, Vol. 249, 1956.

4. Bradshaw, P., and Gee, M.T., Note on the Inner Velocity Profiles of Non-equilibrium Turbulent Boundary Layers. Aero. Res. Council, ARC 20, 889, 1959.

5. Bradshaw, P. and Gregory, N., Calibration of Preston Tubes on a Flat Plate using Measurements of Local Skin Friction. Aero. Res. Council, ARC 20, 199, 1958.

6. Dhawan, S., Direct Measurements of Skin Friction. NACA Report 1121, 1953.

7. Eagle, H.C. and Wilson, W.E., Differential Manometers Investigated. Civil Engrg., Vol. 4, pp. 30-32, 1934.

8. Einstein, H.A. and Harder, J.A., Velocity Distribution and the Boundary Layer at Channel Bends. Trans. AGU, Vol. 35, No. 1, 1954.

9. Elata, C. and Ippen, A.T., The Dynamics of Open Channel Flow with Suspensions of Neutrally Buoyant Particles, Massachusetts Institute of Technology Hydrodynamics Laboratory Technical Report No. 45, 1961.

10. Enger, P.F., Tractive Force Fluctuations around an Open Channel Perimeter as Determined from Point Velocity Measurements. Paper presented at ASCE Convention, Phoenix, Arizona, April 10-14, 1961.

11. Fage, A. and Faulkner, V.M., An Experimental Determination of the Intensity of Friction on the Surface of an Aerofoil. Proc. Roy. Soc. A, London, Vol. 129, p. 378, 1930.

12. Fenter, F.W. and Stalmach, C.S., Jr., The Measurement of Turbulent Boundary Layer Shear Stress by Means of Surface Impact-pressure Probes. J. Aero. Space Sci., 25, 12, 793-794, 1958.

13. Friedkin, J.F., A Laboratory Study of the Meandering of Alluvial Rivers. U.S. Waterways Experiment Station, 1945.

14. Gibson, A.H., Hydraulics and its Applications. London Constable and Co. Ltd., 4th Edition, 1945.

15. Givler, C.A., Measurement of Boundary Shear in an Open Channel Curve with a Surface Pitot Tube. SM Thesis, Massachusetts Institute of Technology (unpublished), 1959.

16. Granville, P.S., The Determination of the Local Skin Friction and the Thickness of Turbulent Boundary Layers from the Velocity Similarity Laws. David Taylor Model Basin Report 1340, 1959.

17. Hakkinen, R.J., Measurements of Turbulent Skin Friction on a Flat Plate at Transonic Speeds. NACA T.N. 3486, 1955.

18. Hsu, E.Y., The Measurement of Local Turbulent Skin Friction by Means of Surface Pitot Tubes, David Taylor Model Basin Report 957, 1955.

19. Ippen, A.T., Drinker, P.A., Jobin, W.R., and Noutsopoulos, G.K., The Distribution of Boundary Shear Stresses in Curved Trapezoidal Channels. Massachusetts Institute of Technology Hydrodynamics Laboratory Technical Report No. 43, 1960.

20. Ippen, A.T. and Mitchell, M.M., The Damping of the Solitary Wave from Boundary Shear Measurements. Massachusetts Institute of Technology Hydrodynamics Laboratory Technical Report No. 23, 1957.

21. Ito, H., Pressure Losses in Pipe Bends. Trans. ASME, J. Basic Engrg. Paper No. 59-Hyd 4, 1959.

22. Lane, E.W., Design of Stable Channels. Trans. ASCE, Vol. 120, p. 1234, 1955.

23. Lane, E.W. and Borland, W.M., River-bed Scour During Floods. Trans. ASCE, Hyd. Div., Vol. 119, p. 1069, 1954.

24. Leliavsky, S., An Introduction to Fluvial Hydraulics. Constable and Co. Ltd., London, 1955.

25. Leighly, J.B., Toward a Theory of the Morphologic Significance of Turbulence in the Flow of Water in Streams. Univ. of Calif. Publication in Geography, Vol. 6, pp. 1-22, 1932.

26. Leopold, L.B., Bagnold, R.A., Wolman, M.G., and Brush, L.M., Jr., Flow Resistance in Sinuous Channels. USGS Professional Papers 282-D and 282-E (R.A. Bagnold), 1960.

27. Leopold, L.B. and Maddock, T., The Hydraulic Geometry of Stream Channels and some Physiographic Implications. USGS Professional Paper 252, 1953.

28. Leopold, L.B. and Wolman, M.G., River Meanders. Bull. Geol. Soc. Am., Vol. 71, p. 769, 1960.

29. Liepmann, H.W. and Skinner, G.T., Shearing-stress Measurements by Use of a Heated Element. NACA T.N. 3268, 1954.

30. Ludweig, H., Instrument for Measuring the Wall Shearing Stress of Turbulent Boundary Layers. NACA T.M. 1284, 1950.

31. Mockmore, C.A., Flow Around Bends in Stable Channels. Trans. ASCE, Vol. 109, p. 593, 1944.

32. Nece, R.E., Givler, C.A., and Drinker, P.A., Measurement of Boundary Shear Stress in an Open Channel Curve with a Surface Pitot Tube. Massachusetts Institute of Technology Hydrodynamics Laboratory Technical Note No. 6, 1959.

33. Nikuradse, J., Laws of Flow in Rough Pipes. NACA T.M. 1292 (originally published in German 1933), 1950.

34. Noutsopoulos, G.K., Velocity and Boundary Shear Distributions in an Open Channel Bend. SM Thesis, Massachusetts Institute of Technology (unpublished), 1960.

35. Olsen, O.J. and Florey, Q.L., Sedimentation Studies in Open Channels, Boundary Shear and Velocity Distribution by the Membrane Analogy, Analytic, and Finite-difference Methods. Bureau of Reclamation Structural Lab. Report No. SP-34, 1952.

36. Parsons, D.A., Effects of Flood Flow on Channel Boundaries. Proc. ASCE, Vol. 86, paper Hy 4, 1960.

37. Preston, J.H., The Determination of Turbulent Skin Friction by Means of Pitot Tubes. J. Roy. Aero. Soc., Vol. 54, pp. 109-121, 1954.

38. Schlichting, H., Boundary Layer Theory. Pergamon Press (McGraw-Hill Book Co.) Inc., New York, 1955.

39. Shukry, A., Flow Around Bends in an Open Flume. Trans. ASCE, Vol. 115, p. 751, 1950.

40. Smith, D.W. and Walker, J.H., Skin-friction Measurements in Incompressible Flow. NASA T.R. R-26 (supersedes NACA TN 4231), 1959.

41. Stanton, T.E., Marshall, D.S., and Bryant, C.H., Proc. Roy. Soc. A, Vol. 97, pp. 422-434, 1920.

42. Steinberg, I.H., Russian River Channel Works. Proc. ASCE, J. Waterways and Harbors Div., WW4, No. 2647, 1960.

43. Sundberg, A., The River Klaralven, a Study of Fluvial Processes. Inst. of Hydr., Roy. Inst. of Tech., Stockholm, Bull. 52, 1956.

44. Thompson, J., On the Origin and Winding of Rivers in Alluvial Plains. Proc. Roy. Soc., London, 1876.

45. Vanoni, V.A. and Nomicos, G. N., Resistance Properties of Sediment Laden Streams. Proc. ASCE, J. Hyd. Div., Vol. 84, paper No. Hy5, 1959.

46. Woodward, S.M., Hydraulics of the Miami Flood Control Project. State of Ohio, The Miami Conservancy District, Technical Reports Part VII, 1920.

47. Young, A.D. and Maas, J.N., The Behavior of a Pitot Tube in a Transverse Total Pressure Gradient. Aero. Res. Council Repts. and Memo. No. 1770, 1937.

# VIII. APPENDIX

## Superelevation in Curved Flow

Consider the flow through a circular curve in a rectangular channel as shown in the accompanying sketch. Neglecting entrance transition effects, let it be assumed that all motion is concentric

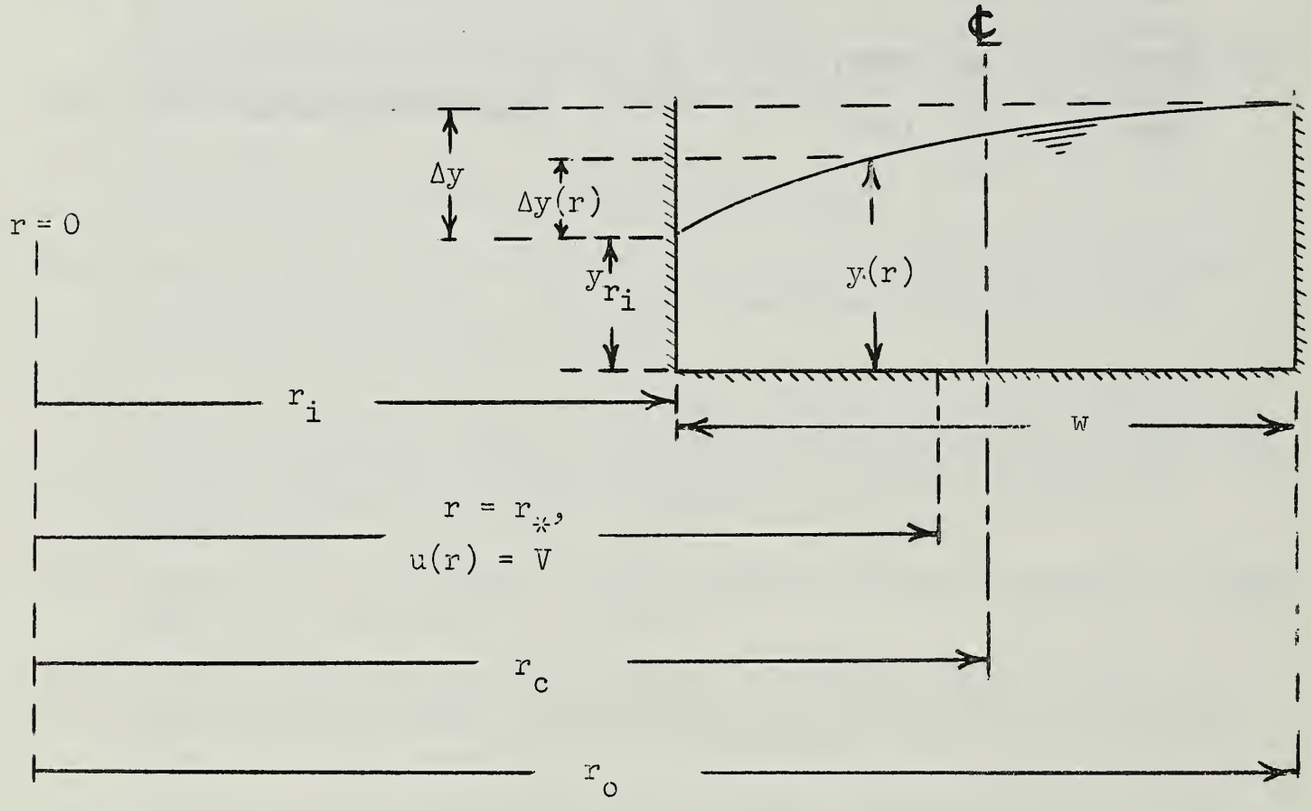


and that there is no frictional dissipation of energy on the stream boundaries. Thus, the mean specific energy is constant at all sections, and may be computed from the approach conditions:

$$\bar{H} = \frac{1}{r_o - r_i} \int_{r_i}^{r_o} H\,dr = H_o = y_o + \frac{V^2}{2g}. \qquad \text{(A-1)}$$

Since the motion of each fluid particle is circular, equilibrium of radial forces is given by:

$$\frac{dp}{dr} = \frac{\rho u(r)^2}{r}. \qquad \text{(A-2)}$$

and, for the free surface, the superelevation becomes:

$$\Delta y\Big|_{(r_o - r_i)} = \int_{r_i}^{r_o} \frac{u(r)^2}{gr}\, dr \,. \qquad \text{(A-3)}$$

However, the computed flow through a curve in a stream of specified discharge must be consistent with the requirements of the conservation of mass and energy. Thus the assigned function u(r) and the depth within the curve y(r) must satisfy:

$$\bar{H} = H_o = \frac{1}{r_o - r_i} \int_{r_i}^{r_o} (y(r) + \frac{u(r)^2}{2g})\, dr \,, \qquad \text{(A-4)}$$

and

$$Q = w\, y_o\, V = \int_{r_i}^{r_o} y(r)\, u(r)\, dr \qquad \text{(A-5)}$$

As a first model for curved flow, the superelevation is computed for the condition of specific energy constant in the radial direction. Then:

$$H(r) = y(r) + \frac{u(r)^2}{2g} = H_o \,, \qquad \text{(A-6)}$$

and

$$\frac{dy}{dr} = \frac{-u}{g} \frac{du}{dr} \,. \qquad \text{(A-7)}$$

From equations (A-2) and (A-7), the velocity distribution function may be computed as that for a free vortex:

$$u = \frac{K_1}{r} \,, \qquad \text{(A-8)}$$

and the total superelevation is given by:

$$\Delta y = \frac{K_1^2}{2g}(\frac{1}{r_i^2} - \frac{1}{r_o^2}) \qquad \text{(A-9)}$$

As shown in the definition sketch the effective mean radius, $r_*$, is defined such that:

$$u\Big|_{(r=r_*)} = V ,$$

Hence,

$$K_1 = V\, r_* \qquad \text{(A-10)}$$

and

$$u = \frac{V r_*}{r} .$$

Then the mean depth within the curve may be obtained as:

$$y_m = \frac{1}{r_o - r_i}\int_{r_i}^{r_o} y(r)dr = \frac{1}{r_o - r_i}\int_{r_i}^{r_o} (H_o - \frac{u(r)^2}{2g})dr , \qquad \text{(A-11)}$$

where $y(r)$ is as defined implicitly in equation (A-6). The resulting expression:

$$y_m = H_o - \frac{V^2}{2g}\frac{r_*^2}{r_c r_i} ,$$

may be arranged as:

$$\frac{y_m}{y_o} = 1 + \frac{F^2}{2}\left(1 - \frac{(r_*/r_c)^2}{1 - (\frac{w}{2r_c})^2}\right) . \qquad \text{(A-12)}$$

Equation (A-12) indicates that the mean depth in the curve may not be assumed a priori equal to the depth in the approach flow.

Equation (A-5) becomes:

$$Q = \int_{r_i}^{r_o} \frac{V r_*}{r}(H_o - \frac{V^2 r_*^2}{2g\, r^2})dr = H_o\, V r_*\, \ln(\frac{r_o}{r_i}) + \frac{V^3 r_*^3}{4g}(\frac{r_i^2 - r_o^2}{r_o^2\, r_i^2}) , \qquad \text{(A-13)}$$

which leads to the cubic equation:

$$\left(\frac{r_*}{r_o}\right)^3 - \frac{r_*}{r_c}\left[\frac{[2+\mathbb{F}^2]\left[1-\left(\frac{w}{2r_c}\right)^2\right]^2}{2\,\mathbb{F}^2\left(\frac{w}{2r_c}\right)}\ln\left(\frac{1+\frac{w}{2r_c}}{1-\frac{w}{2r_c}}\right)\right] + \frac{2\left[1-\left(\frac{w}{2r_c}\right)^2\right]^2}{\mathbb{F}^2} = 0 \quad \text{(A-14)}$$

Then, equations (A-9), (A-10), and (A-14) may be combined to give:

$$\left(\frac{\Delta y}{y_o}\right)^{3/2} - \left(\frac{\Delta y}{y_o}\right)^{1/2}\left[(2+\mathbb{F}^2)\ln\left(\frac{1+\left[\frac{w}{2r_c}\right]}{1-\left[\frac{w}{2r_c}\right]}\right) + \frac{4\sqrt{2}\,\mathbb{F}\left(\frac{w}{2r_c}\right)^{3/2}}{\left[1-\left(\frac{w}{2r_c}\right)^2\right]}\right] = 0 \quad \text{(A-15)}$$

Equation (A-15) is plotted in Figure A-1 showing the relative superelevation, $\Delta y/y_o$, as a function of Froude number for three values of relative curvature, $w/r_c$. As shown in the text of this report (see pp. 48 ff.) the initial assumption of constant mean depth in the curve leads to the expression:

$$\Delta y = \frac{V^2}{2g}\frac{2w}{r_c}\left[\frac{1}{1-\left(\frac{w}{2r_c}\right)^2}\right] , \quad \text{(11b)}$$

or,

$$\frac{\Delta y}{y_o} = 2\,\mathbb{F}^2\left(\frac{w}{2r_c}\right)\left[\frac{1}{1-\left(\frac{w}{2r_c}\right)^2}\right] , \quad \text{(A-16)}$$

which is also plotted in Figure A-1. It is seen from the figure that at higher Froude numbers equation (A-16) gives values of $\Delta y/y_o$ which are too low, although at moderate curvatures the differences are not great and the assumption $y_m = y_o$ is reasonable.

As the second flow condition, it is assumed that the velocities increase linearly in the radial direction. This flow distribution, which is seen near the end of a long river bend (cf Runs 5,6,7,10,11), corresponds to a forced vortex. Under the assumption,

$$u = K_2\, r , \quad \text{(A-17)}$$

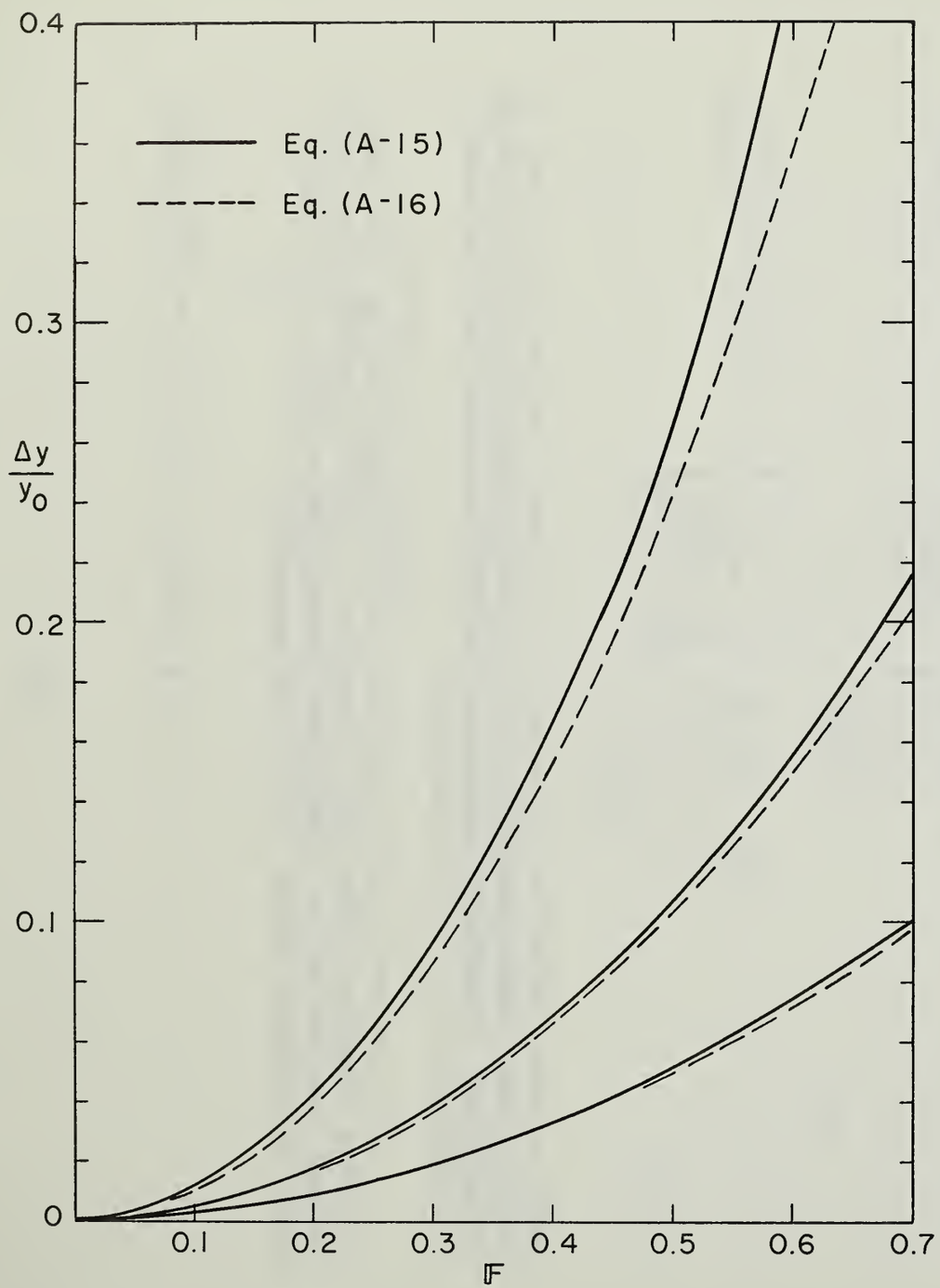


Figure A-1. Superelevation Computed for a Free Vortex.

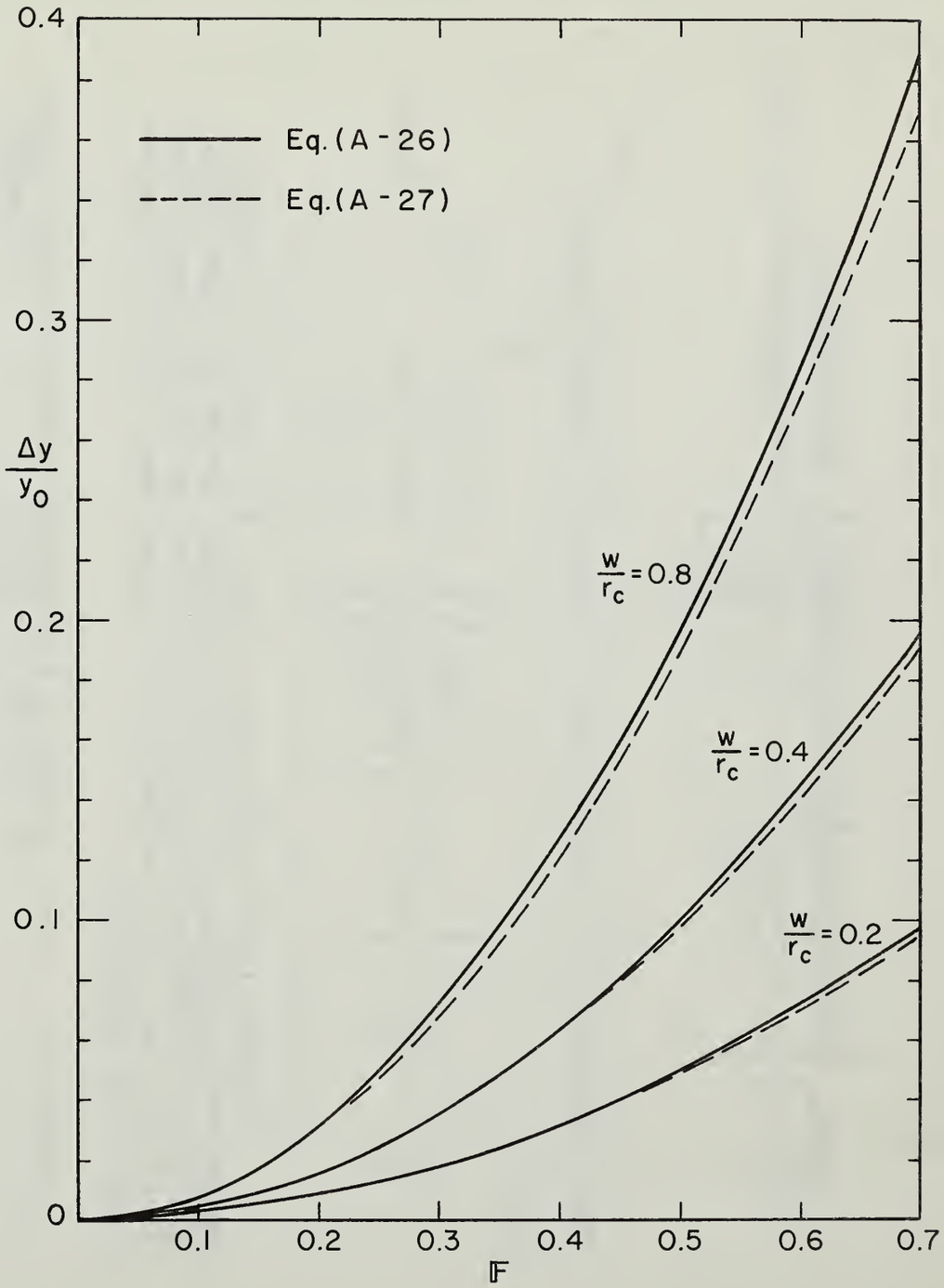


Figure A-2. Superelevation Computed for a Forced Vortex.

the total superelevation is given by:

$$\Delta y = \frac{K_2^2}{2g}(r_o^2 - r_i^2) \ . \qquad \text{(A-18)}$$

Again introducing the effective mean radius, $r_*$, the expression reduces to:

$$\frac{\Delta y}{y_o} = \mathbb{F}^2 \frac{w}{r_c}\left(\frac{r_c}{r_*}\right)^2 \qquad \text{(A-19)}$$

By the assumption of constant mean specific energy, the mean depth in the curve is given by:

$$y_m = H_o - \frac{V^2}{2g}\frac{1}{r_*^2}\frac{r_o^3 - r_i^3}{3(r_o - r_i)} \qquad \text{(A-20)}$$

which may be expressed by:

$$\frac{y_m}{y_o} = 1 + \frac{\mathbb{F}^2}{2}\left[1 - \left(\frac{r_c}{r_*}\right)^2\left(\frac{3 + \left(\frac{w}{2r_c}\right)^2}{3}\right)\right]. \qquad \text{(A-21)}$$

Now in order to evaluate the continuity relation, (A-5), it is necessary to further define $y(r)$, since in this case the function, $H(r)$, is an unknown. Expressing $y(r)$ in terms of the depth at the inner bank:

$$y(r) = y_{r_i} + \delta\, y(r) = y_{r_i} + \int_{r_i}^{r} \frac{V^2}{r_*^2 g}\, r\, dr, \qquad \text{(A-22)}$$

and

$$y_m = \frac{1}{r_o - r_i}\int_{r_i}^{r_o} y(r)dr = y_{r_i} + \frac{1}{r_o - r_i}\int_{r_i}^{r_o}\left[\int_{r_i}^{r}\frac{V^2}{r_*^2 g}\, r\, dr\right] dr \qquad \text{(A-23)}$$

This equation can be integrated and rearranged to give:

$$\frac{y_{r_i}}{y_o} = \frac{y_m}{y_o} - \mathbb{F}^2\left(\frac{r_c}{r_*}\right)^2\left[\frac{\frac{w}{2r_c}\left(3 - \frac{w}{2r_c}\right)}{3}\right] . \qquad \text{(A-24)}$$

Introducing equation (A-22) into the continuity expression, equation (A-5) becomes:

$$Q = \int_{r_i}^{r_o} \left[ y_{r_i} + \int_{r_i}^{r} \frac{V^2}{r_*^2 g} r\, dr \right] \frac{V}{r_*} r\, dr \,. \qquad \text{(A-25)}$$

Equations (A-19), (A-21), (A-24), and (A-25) may then be combined to give:

$$\left(\frac{\Delta y}{y_o}\right)^{3/2} \left[ \frac{3 - \left(\frac{w}{2r_c}\right)^2}{3} \right] - \left(\frac{\Delta y}{y_o}\right)\left(\frac{w}{r_c}\right)(2 + \mathbb{F}^2) + 4\sqrt{2}\ \mathbb{F}\left(\frac{w}{2r_c}\right)^{3/2} = 0 \quad \text{(A-26)}$$

Equation (A-26) is plotted in Figure A-2, together with the expression based on the assumption of constant mean depth:

$$\Delta y = \frac{V^2}{2g} \frac{2w}{r_c} \left[ \frac{1}{1 + \frac{w^2}{12 r_c^2}} \right] \qquad \text{(11-c)}$$

which may be rewritten as:

$$\frac{\Delta y}{y_o} = 2\mathbb{F}^2 \frac{w}{2r_c} \left[ \frac{3}{3 + \left(\frac{w}{2r_c}\right)^2} \right] . \qquad \text{(A-27)}$$

It may be seen from the figure that, except for conditions of severe curvature, the two expressions give virtually identical values of $\Delta y/y_o$, and that the assumption of constant mean depth is completely justified.

From the foregoing developments which lead to equations (A-15) and (A-26) it will be seen that, in general, if the velocity distribution for flow in an open circular curve can be expressed as some integrable function:

$$u = u(r) \,,$$

then an exact solution for the total superelevation may be found, which is based on the single fundamental assumption of constant total energy. Although the complete form of the transverse surface profile has not been given here, it can be shown that the explicit function for the depth at any radius, equation (A-22), can be obtained through solution of expressions of the form of equations (A-21), (A-23), and (A-24).

It is again recalled that, consistent with the above assumption, no restrictions need be placed on the geometry of the water surface. For

example, equations (A-12) and (A-21) indicate that an a priori assumption of $y_m/y_o = 1$ is not justified. However, for a broad range of curvatures and Froude numbers, essentially covering normal stream conditions, Figures A-1 and A-2 indicate that the error introduced by this simplifying assumption is in fact negligible.